

Effect of Alloying Additions and Heat Treatment on Localized Corrosion
Susceptibilities of AA7xxx Alloys Grain Refined with Al-5Ti-1B Master
Alloy

Effect of Alloying Additions and Heat Treatment on Localized Corrosion Susceptibilities
of AA7xxx Alloys Grain Refined with Al-5Ti-1B Master Alloy

By JORDAN KRAMP, B.ENG

A Thesis

Submitted to the Department of Materials Science & Engineering

And School of Graduate Studies

In Partial Fulfilment of the Requirements

For the Degree

Master of Applied Science

McMaster University

© Copyright by Jordan Kramp, April 2018

McMaster University

Hamilton, Ontario

MASTER OF APPLIED SCIENCE (2018)

(Materials Science & Engineering)

TITLE:

Effect of Alloying Additions and Heat Treatment on
Localized Corrosion Susceptibilities of AA7xxx
Alloys Grain Refined with Al-5Ti-1B Master Alloy

AUTHOR:

Jordan Kramp, B. Eng (McMaster University)

SUPERVISOR:

Dr. J.R. Kish and Dr. S. Shankar

NUMBER OF PAGES:

xix, 145

Abstract

The aim of this research was to identify the effect of alloying additions and heat treatment on the localized corrosion mechanisms of AA7xxx alloys that have been grain refined with an Al-5Ti-1B master alloy. The major alloying elements, Zn (3.5 – 6.5 wt. %), Mg (1.5 – 2.5 wt.%), Cu (0 – 3 wt. %), and Ti (0.04 – 0.25 wt.%), were varied and ten AA7xxx aluminum alloys were cast, heat treated to the T4, T6, T79, T76, and T73 tempers, and studied extensively.

Casting high integrity near net shaped AA7xxx components by introducing Ti and B into the melt to facilitate a non-dendritic microstructure produced a unique microstructure due to the phenomena of athermal nucleation, unconstrained growth, and solute field impingement. The three phenomena listed above create three microstructural regimes; dendritic area rich in Ti, interdendritic region lean in Ti, and grain boundary area rich in eutectic phases.

The breakdown potential, E_b , in a detreated 0.5 M NaCl_(aq) was determined for each alloy and heat treatment after 1 h at the open circuit potential. The effect of alloying element composition and heat treatment on E_b was examined and an empirical expression was created. It was determined that a semi-logarithmic relationship exists between E_b and the Zn/Cu weight ratio. Zn and Cu have opposing effects on E_b , where, Zn-depletion from the solid solution into the strengthening precipitates increased the E_b while Cu-depletion decreased the same. Cu-lean alloys have a continually increasing E_b from T4 to T6 and

T7x temper conditions, while, Cu-rich alloys have no significant change in E_b with temper condition. The critical Zn/Cu weight ratio was determined to be approximately 5.

Corrosion initiation mechanisms of a Cu-lean and Cu-rich alloy were studied using the dual beam FIB-SEM platform after 5 min of potentiostatic polarization in detreated 0.5 M NaCl_(aq) at potentials of interest. The initiation mechanism of the Cu-rich alloy (alloy 3) was determined to be dealloying of the S-phase (Al₂CuMg) along the grain boundary leading to intergranular corrosion. The surface of the Cu-lean alloy (alloy 6) after potentiostatic polarization above E_b showed three mechanisms of corrosion; corrosion domes, corrosion rings, and interdendritic corrosion. Corrosion rings were identified as the initiation mechanism, corrosion domes were determined to be metastable sites and not a precursor to further corrosion, interdendritic corrosion was determined to be the propagation mechanism. Interdendritic corrosion is the selective dissolution of the interdendritic region leaving the dendritic regime intact after immersion in a corrosive solution which is unique to these alloys grain refined with the Ti-B master alloy. Corrosion domes were shown to cause an active-passive region in the potentiodynamic polarization curve.

Modified EXCO experiments were used to study the propagation mechanism in each of the alloys at each temper. All alloys and tempers were susceptible to interdendritic corrosion, however Cu-lean alloys showed less surface damage after 96 h of immersion in the modified EXCO solution. Alloys with a Zn/Mg weight ratio < 2 were susceptible to intergranular corrosion in the T6 temper, however, in the T4 and T7x temper the primary mode of corrosion propagation is interdendritic corrosion. Due to the bimodal distribution

of the grain size, intergranular corrosion was only observed in the small grain areas. The extent of attack was more severe in the small grain regions with intergranular corrosion present than areas without leading to the conclusion that intergranular corrosion is more detrimental than interdendritic corrosion.

Acknowledgements

First, I would like to thank my supervisors Dr. Joey Kish and Dr. Sumanth Shankar for their tireless efforts in the completion of this body of work. They have allowed me to work independently to grow as a researcher and professional.

I would like to acknowledge my colleagues in the department of Material Science and Engineering at McMaster University, Centre for Automotive Materials and Corrosion (CAMC), and the Light Metal Research Centre (LMRC). There are individuals who throughout my work have been especially helpful and require special mention. Dr. Elizabeth McNally for her constant support at the McMaster Automotive Research Centre (MARC). Travis Casagrande for his expertise and operation of the dual beam FIB-SEM. Dr. Xiaochun Zeng for his guidance during the heat treatment portion of this thesis. Doug Culley and Xiogang Li for their support in material characterization.

My industry partners Fiat Chrysler Automotive of Canada and USA and Nemak of Canada deserve recognition for providing me with this opportunity. My thanks to the Automotive Partnership of Canada and NSERC for providing financial support for this project.

Finally, I would like to acknowledge my family and friends for their constant support and necessary distractions. I would like to thank Melissa for putting up with me over the last few years. Most of all, I would like to acknowledge my parents to whom this thesis is dedicated. Their never-ending support throughout all aspects of my life have allowed me to take full advantage of all opportunities that have come my way.

Abbreviations and Symbols

List of Abbreviations

AA	Aluminum Association
APT	Atom Probe Tomography
ASAXS	Anomalous Small Angle X-ray Scattering
BSE	Backscatter Electron Image
BFSTEM	Bright Field Scanning Transmission Electron Image
DOE	Design of Experiments
ECD	Effective Circular Diameter
EDS	X-ray Energy Dispersive Spectroscopy
EXCO	Exfoliation Corrosion
FIB	Focused Ion Beam
GDOES	Glow Discharge Optical Emission Spectroscopy
GP (I & II)	Guinier-Preston Zone (I & II)
IDC	Interdendritic Corrosion
IGA	Intergranular Attack
IGC	Intergranular Corrosion
IMP	Intermetallic Phase
L	Longitudinal Direction
N	Normal Direction
PFZ	Precipitate Free Zone
S/L	Solid – Liquid
SCC	Stress Corrosion Cracking
SCE	Standard Calomel Electrode
SEI	Secondary Electron Image
SEM	Scanning Electron Microscopy

SHT	Solution Heat Treatment
SSSS	Super Saturated Solid Solution
STEM	Scanning Transmission Electron Microscopy
T	Transverse Direction
TEM	Transmission Electron Microscopy
TPGC	Tilt Pour Gravity Cast
UTS	Ultimate Tensile Strength
V	Validation Alloy
VRC	Vacancy Rich Cluster
YS	Yield Strength

List of Symbols

%	Percent
°C	Degrees Celsius
±	Plus/Minus
aq	Aqueous
cm	Centimetre
ΔT_c	Constitutional Undercooling
ΔT_r	Curvature Undercooling
ΔT_T	Thermal Undercooling
E_b	Breakdown potential
η	Eta
η'	Eta prime
g	gram
h	Hour
H	Hardness
kV	Kilovolt
log	Logarithm
μm	micrometre
m	Metre
M	Molar concentration
mA	Milliampere
min	Minute
mL	Millilitre
mm	Millimetre
mol	Mole
mV	Millivolt
nA	Nanoampere

pA	Picoampere
s	Second
T _e	Eutectic temperature
wt. %	Weight percent

Table of Contents

Chapter 1: Introduction.....	1
Chapter 2: Literature Review.....	6
2.1.0 AA7xxx Series Aluminum Alloys.....	6
2.2.0 Solidified Microstructure.....	8
2.2.1 Athermal Nucleation.....	10
2.2.2 Unconstrained Growth.....	10
2.2.3 Solute Field Impingement.....	11
2.2.4 Solidifying Cast vs Wrought Alloys.....	12
2.2.5 Abnormal Grain Growth Characteristics.....	13
2.3.0 Heat Treatments.....	14
2.4.0 Precipitation Sequence.....	16
2.5.0 Secondary Phases.....	19
2.6.0 Precipitate Free Zone (PFZ).....	22
2.7.0 Corrosion Mechanisms in Aluminum Alloys.....	22
2.7.1 Intergranular Corrosion.....	23
2.7.2 Intergranular Stress Corrosion Cracking.....	25
2.7.3 Corrosion Rings and Clustering.....	26
2.7.4 Exfoliation Corrosion.....	28
2.8.0 Breakdown Potential, E_b	29
Chapter 3: Experiments.....	31
3.1.0 Materials.....	31
3.2.0 Transient Hardness.....	33
3.3.0 Corrosion Experiments.....	35
3.3.1 Modified EXCO Experiment.....	36
3.3.2 Electrochemical Experiments.....	38
3.4.0 Material Characterization.....	39
3.4.1 Light Optical Microscopy.....	39
3.4.2 Electron Microscopy.....	40
Chapter 4: Results and Discussion.....	43
4.1.0 Microstructural Characterization.....	43

4.2.0 Potentiodynamic Polarization	50
4.2.1 Breakdown Potential, E_b	50
4.2.2 Potentiodynamic Polarization of Alloy 6.....	59
4.3.0 Modified EXCO Experiments.....	68
4.4.0 Summary of Corrosion Mechanisms in AA7xxx Alloys	85
Chapter 5: Conclusions	89
Chapter 6: Future Work	94
Chapter 7: Appendix.....	97
7.1.0 Alloy 1	97
7.2.0 Alloy 2	101
7.3.0 Alloy 3	105
7.4.0 Alloy 4	109
7.5.0 Alloy 5	113
7.6.0 Alloy 6	117
7.7.0 Alloy 7	121
7.8.0 Alloy 8	125
7.9.0 Alloy 9	129
7.10.0 Validation Alloy.....	133
References	137

List of Tables

Table 2.1: Main alloying elements in the wrought aluminum alloy designation system [6].	6
Table 2.2: Common strain and thermal treatment designations [9].	7
Table 2.3: Subset galvanic series of compounds common in 7xxx series Al alloys [7,34].	19
Table 3.1: Target and actual compositions of each alloy as determined by GDOES. A denotes the composition of the TPGC samples and B denotes the composition of the permanent mould plates.	32
Table 4.1: Summary of possible phases present in the as-cast condition of each alloy as determined by the non-equilibrium simulation using Pandat software.	45
Table 4.2: Mean values of breakdown potential (E_b) observed in each alloy (and temper). Mean values are based on three repetitions of experiments conducted using a de-aerated 0.5M NaCl _(aq) solution at room temperature.	51
Table 4.3: Values of the constants A and B in Equation (2) along with the R^2 value of the linear regression model and % difference between experimental and predicted E_b in the validation alloy.	55
Table 4.4: Summary of active potentials in alloy 6.	60
Table 4.5: Summary of corrosion mechanisms in each alloy as a function of composition and temper.	87
Table 7.1: Alloy 1 compositions as determined by GDOES.	97
Table 7.2: Rockwell hardness and associated ageing time for Alloy 1.	97
Table 7.3: Alloy 1 grain size summary.	98
Table 7.4: Alloy 2 compositions as determined by GDOES.	101
Table 7.5: Rockwell hardness and associated ageing time for alloy 2.	101
Table 7.6: Alloy 2 grain size summary.	102
Table 7.7: Alloy 3 compositions as determined by GDOES.	105
Table 7.8: Rockwell hardness and associated ageing time for alloy 3.	105
Table 7.9: Alloy 3 grain size summary.	106
Table 7.10: Alloy 4 compositions as determined by GDOES.	109
Table 7.11: Rockwell hardness and associated ageing time for alloy 4.	109
Table 7.12: Alloy 4 grain size summary.	110
Table 7.13: Alloy 5 compositions as determined by GDOES.	113
Table 7.14: Rockwell hardness and associated ageing time for alloy 5.	113
Table 7.15: Alloy 5 grain size summary.	114
Table 7.16: Alloy 6 compositions as determined by GDOES.	117
Table 7.17: Rockwell hardness and associated ageing time for alloy 6.	117
Table 7.18: Alloy 6 grain size summary.	118
Table 7.19: Alloy 7 compositions as determined by GDOES.	121
Table 7.20: Rockwell hardness and associated ageing time for alloy 7.	121
Table 7.21: Alloy 7 grain size summary.	122

Table 7.22: Alloy 8 compositions as determined by GDOES.	125
Table 7.23: Rockwell hardness and associated ageing time for alloy 8.	125
Table 7.24: Alloy 8 grain size summary.	126
Table 7.25: Alloy 9 compositions as determined by GDOES.	129
Table 7.26: Rockwell hardness and associated ageing time for alloy 9.	129
Table 7.27: Alloy 9 grain size summary.	130
Table 7.28: Validation alloy compositions as determined by GDOES.....	133
Table 7.29: Rockwell hardness and associated ageing time for the validation alloy.....	133
Table 7.30: Validation alloy grain size summary.	134

List of Figures

Figure 2.1: General properties associated with T6 and T7x heat treatments [10].	7
Figure 2.2: Micrographs illustrating the differing morphology AA7050 alloy with (a) dendritic microstructure with no Ti additions (b) non-dendritic microstructure obtained through 0.07 wt% Ti addition to the melt [11].	8
Figure 2.3: Overaged AA7xxx alloy (Al-5.9Zn-1.6Mg-2.7Cu-0.19Ti) etched with Weck's reagent revealing dendritic imprints.	9
Figure 2.4: Thermal profiles in front of dendritic arm for thermal undercooling (T_T), constitutional undercooling (T_c), and curvature undercooling (T_r) [16].	11
Figure 2.5: Simulated solid fraction development of (a) A356.2 casting alloy and (b) AA7050 wrought alloy during solidification [11].	13
Figure 2.6: Schematic diagrams illustrating (a) the stability of precipitates in an Al-2Mg-Zn system (b) the free energy change with the formation of metastable precipitates [2].	17
Figure 2.7: Schematic of corrosion mechanism present in the S-phase [44].	21
Figure 2.8: Stages to stable pitting in AA2024-T3 [39].	23
Figure 2.9: Phenomenological intergranular corrosion model developed by Kairy et al. using nine various compositions of the AA6xxx series alloys [47].	25
Figure 2.10: Effect of alloying element content and heat treatment on the crack growth rate of Al-Zn-Mg-Cu alloys during SCC in 0.6 M NaCl _(aq) solutions compiled by Holroyd et al. [52].	26
Figure 2.11: Image of intermetallic clustering surrounded by a ring of corrosion product in AA2024-T3 [39].	27
Figure 3.1: Typical cats samples in this study (a) TPGC sample outlining “U-shaped” sections used for ageing coupons (b) Permanent mould casting of corrosion plate used for alloy 8 T79 tests outlining sections used for corrosion and microstructure analyses.	32
Figure 3.2: Graphical schematic of the heat treatment of the alloy castings used to acquire transient ageing curves.	34
Figure 3.3: Layout of plate samples immersed in the modified EXCO solution. Three plate samples of alloy 1, 4, and 7 in the T76 temper are shown.	37
Figure 3.4: Sequence of TEM foil sample preparation in FIB-SEM (a) Sample location (b) Tungsten deposition and trenching (c) Micromanipulator attached to sample by tungsten deposition (d) sample attached to Mo grid and polished with Ga ⁺ beam.	41
Figure 4.1: Solid fraction trace simulated under non-equilibrium conditions with Pandat software for (a) full solid fraction range (b) expanded solid fraction range approaching 1.0 (complete solidification).	44

Figure 4.2: Light optical micrograph of alloy 8 after natural ageing (T4 temper) showing abnormal grain growth while retaining the morphology and size of the equiaxed dendrites from solidification.	47
Figure 4.3: Typical qualitative EDS spot analyses taken within and adjacent to the equiaxed dendritic imprint to demonstrate the relative difference in Ti content (intensity) in these regions. Spectra taken on surface of alloy 6 at the T6 temper after potentiostatic polarization at $-884 \text{ mV}_{\text{SCE}}$ for 5 min.	49
Figure 4.4: The plots of main effects of the independent parameters (wt.%) on the dependant variable, E_b	52
Figure 4.5: Plot of E_b with respect to temper of the samples.....	53
Figure 4.6: Graphical representation of the linear regression model correlating E_b to the weight ratio of Zn to Cu in the alloys (a) T4 (b) T6 (c) T79 (d) T76 (e) T73.	56
Figure 4.7. Graphical plot of E_b and the weight ratio of Zn to Cu that is representative of the ten alloys in this study.....	57
Figure 4.8: Potentiodynamic anodic polarization curves of alloy 6 in deaerated 0.5 M $\text{NaCl}_{(\text{aq})}$ solution.	59
Figure 4.9: Secondary electron image of the pristine (as-etched) surface of alloy 6 at the T6 temper clearly showing the dendritic imprints and grain boundaries.....	61
Figure 4.10: Results of the potentiostatic polarization experiment of alloy 6 at the T6 temper corresponding to matrix breakdown ($-884 \text{ mV}_{\text{SCE}}$ in deaerated 0.5 M $\text{NaCl}_{(\text{aq})}$) (a) potentiodynamic (b) current density transient during 5 min potentiostatic (c-d) secondary electron image of the surface (e) secondary electron image of a FIB-prepared cross-section of a corrosion dome with intermetallic particle at base (f) secondary electron image of a FIB-prepared corrosion-section of a co-operative corrosion ring.	62
Figure 4.11: EDS elemental maps of the corrosion dome observed in FIB-prepared cross-section of alloy 6 at the T6 temper shown in Figure 10e.....	64
Figure 4.12: Results of the potentiostatic polarization experiment of alloy 6 at the T6 temper corresponding to the 1 st active state region ($-1040 \text{ mV}_{\text{SCE}}$) in deaerated 0.5 M $\text{NaCl}_{(\text{aq})}$: (a) potentiodynamic curve (b) current density transient (c) secondary electron image of surface (d) secondary electron image of FIB-prepared cross-section through a corrosion dome (e) EDS spot analyses corrosion dome and underlying intermetallic particle corresponding to the spots identified in (d).....	67
Figure 4.13: Light optical images of the corroded surface of alloys at the T6 temper in cross-section and after 96 h immersion in the modified EXCO solution (a) Al-3.4Zn-1.5Mg-0.04Ti (b) Al-6.5Zn-2.4Mg-1.3Cu-0.04Ti (c) Al-5.4Zn-2.2Mg-3Cu-0.05Ti (d) Al-5Zn-2.1Mg-0.12Ti (e) Al-3.6Zn-2Mg-1.5Cu-0.12Ti (f) Al-7Zn-1.7Mg-3Cu-0.15Ti (g) Al-5.1Zn-1.6Mg-1.4Cu-0.25Ti (h) Al-5.9Zn-1.6Mg-12.7Cu-0.2Ti (i) Al-3.6Zn-2.5Mg-2.9Cu-0.2Ti.	71
Figure 4.14: Light optical microscopy images of the typical microstructure found in (a) alloy 2 with a bimodal distribution of grain size due to abnormal grain growth and (b) alloy 3 with a uniform grain size.....	72
Figure 4.15: Light optical microscopy images of the corroded surface in cross-section after 96 h immersion in modified EXCO solution: (a) alloy 2 at the T6 temper (small	

grain area), (b) alloy 2 at the T6 temper (large grain area), (c) alloy 2 at the T79 temper (small grain area), (d) alloy 3 at the T6 temper and (e) alloy 3 at the T79 temper.	73
Figure 4.16: Photograph taken of the alloy 2 at the T6 temper plate sample (a) before immersion and (b) after 96 h of immersion in the modified EXCO solution. (c) Overlay of corroded areas (red) and large grain area (black outline).	74
Figure 4.17: Secondary electron image of the alloy 3 at the T6 temper plate surface in the pristine (as-etched) condition.	75
Figure 4.18: Results of the potentiostatic polarization experiment (-683 mV _{SCE} for 5 min. in deaerated 0.5 M NaCl _(aq)) of alloy 3 at the T6 temper: (a) potentiodynamic curve (b) current density transient during potentiostatic polarization (c and e) secondary electron images of the polarized surface, (d and f) secondary electron images of FIB-prepared cross-section through partially dealloyed S-phase.	77
Figure 4.19: EDS elemental map of the polarized alloy 3 at the T6 temper plate surface showing enrichment of Cu phases along the grain boundaries.	78
Figure 4.20: Secondary electron image of S-phase particle in cross-section and associated set of EDS spot analyses corresponding to the locations identified in the image for alloy 3 at the T6 temper.	79
Figure 4.21: Bright field (BF) scanning TEM (STEM) images of alloy 3 at the T6 temper in the pristine condition (a) low magnification (b) grain boundary with Cu-rich precipitate formation (c) EDS spot analyses of the grain boundary precipitate identified in (b).	81
Figure 4.22: Secondary electron image of the alloy 3 at the T73 temper plate surface in the pristine (as-etched) condition.	82
Figure 4.23: Results of the potentiostatic polarization experiment (-696 mV _{SCE} for 5 min. in deaerated 0.5 M NaCl _(aq)) of alloy 3 at the T73 temper: (a) potentiodynamic curve (b) current density transient during potentiostatic polarization (c) secondary electron image of polarized surface (d) secondary electron image of FIB-prepared cross-section through S-phase particle cluster, and (e) EDS spectra for selected locations identified in (d).	84
Figure 7.1: Ageing curve for alloy 1 at 185°C (HREW).	97
Figure 7.2: Alloy 1 cross-sections after 96 h immersion in EXCO solution at 200x (a) T4 (b) T6 (c) T79 (d) T76 (e) T73. Scale is 50 µm.	98
Figure 7.3: Alloy 1 micrographs at 100x of (a) T4 (b) T6 (c) T79 (d) T76 (e) T73.	98
Figure 7.4: Alloy 1 images before and after immersion in modified EXCO solution (a-b) T4 (c-d) T6 (e-f) T79 (g-h) T76 (i-j) T73.	99
Figure 7.5: Alloy 1 potentiodynamic polarizations in deaerated 0.5M NaCl _(aq) solution.	100
Figure 7.6: Alloy 1 maximum depth of penetration observed in cross-section after 96 h of immersion in modified EXCO solution.	100
Figure 7.7: Ageing curve for alloy 2 at 185°C (HRBW).	101
Figure 7.8: Alloy 2 cross-sections after 96 h immersion in EXCO solution at 200x (a) T4 (b) T6 (c) T79 (d) T76 (e) T73. Scale is 50 µm.	102
Figure 7.9: Alloy 2 micrographs at 100x of (a) T4 (b) T6 (c) T79 (d) T76 (e) T73.	102

Figure 7.10: Alloy 2 images before and after immersion in modified EXCO solution (a-b) T4 (c-d) T6 (e-f) T79 (g-h) T76 (i-j) T73.	103
Figure 7.11: Alloy 2 potentiodynamic polarizations in deaerated 0.5M NaCl _(aq) solution.	104
Figure 7.12: Alloy 2 maximum depth of penetration observed in cross-section after 96 h of immersion in modified EXCO solution.	104
Figure 7.13: Ageing curve for alloy 3 at 185°C (HRBW).	105
Figure 7.14: Alloy 3 cross-sections after 96 h immersion in EXCO solution at 200x (a) T4 (b) T6 (c) T79 (d) T76 (e) T73. Scale is 50 µm.*	106
Figure 7.15: Alloy 3 micrographs at 100x of (a) T4 (b) T6 (c) T79 (d) T76 (e) T73.	106
Figure 7.16: Alloy 3 images before and after immersion in modified EXCO solution (a-b) T4 (c-d) T6 (e-f) T79 (g-h) T76 (i-j) T73.	107
Figure 7.17: Alloy 3 potentiodynamic polarizations in deaerated 0.5M NaCl _(aq) solution.	108
Figure 7.18: Alloy 3 maximum depth of penetration observed in cross-section after 96 h of immersion in modified EXCO solution.	108
Figure 7.19: Ageing curve for alloy 4 at 185°C (HRBW).	109
Figure 7.21: Alloy 4 cross-sections after 96 h immersion in EXCO solution at 200x (a) T4 (b) T6 (c) T79 (d) T76 (e) T73. Scale is 50 µm.	110
Figure 7.20: Alloy 4 micrographs at 100x of (a) T4 (b) T6 (c) T79 (d) T76 (e) T73.	110
Figure 7.22: Alloy 4 images before and after immersion in modified EXCO solution (a-b) T4 (c-d) T6 (e-f) T79 (g-h) T76 (i-j) T73.	111
Figure 7.23: Alloy 4 potentiodynamic polarizations in deaerated 0.5M NaCl _(aq) solution.	112
Figure 7.24: Alloy 4 maximum depth of penetration observed in cross-section after 96 h of immersion in modified EXCO solution.	112
Figure 7.25: Ageing curve for alloy 5 at 185°C (HRBW).	113
Figure 7.26: Alloy 5 cross-sections after 96 h immersion in EXCO solution at 200x (a) T4 (b) T6 (c) T79 (d) T76 (e) T73. Scale is 50µm.	114
Figure 7.27: Alloy 5 micrographs at 100x of (a) T4 (b) T6 (c) T79 (d) T76 (e) T73.	114
Figure 7.29: Alloy 5 images before and after immersion in modified EXCO solution (a-b) T4 (c-d) T6 (e-f) T79 (g-h) T76 (i-j) T73.	115
Figure 7.30: Alloy 5 potentiodynamic polarizations in deaerated 0.5M NaCl _(aq) solution.	116
Figure 7.31: Alloy 5 maximum depth of penetration observed in cross-section after 96 h of immersion in modified EXCO solution.	116
Figure 7.32: Ageing curve for alloy 6 at 185°C (HRBW).	117
Figure 7.33: Alloy 6 cross-sections after 96 h immersion in EXCO solution at 200x (a) T4 (b) T6 (c) T79 (d) T76 (e) T73. Scale is 50 µm.	118
Figure 7.34: Alloy 6 micrographs at 100x of (a) T4 (b) T6 (c) T79 (d) T76 (e) T73.	118
Figure 7.35: Alloy 6 images before and after immersion in modified EXCO solution (a-b) T4 (c-d) T6 (e-f) T79 (g-h) T76 (i-j) T73.	119
Figure 7.36: Alloy 6 potentiodynamic polarizations in deaerated 0.5M NaCl _(aq) solution.	120

Figure 7.37: Alloy 6 maximum depth of penetration observed in cross-section after 96 h of immersion in modified EXCO solution.....	120
Figure 7.38: Ageing curve for alloy 7 at 185°C (HRBW).	121
Figure 7.40: Alloy 7 cross-sections after 96 h immersion in EXCO solution at 200x (a) T4 (b) T6 (c) T79 (d) T76 (e) T73. Scale is 50 µm.	122
Figure 7.39: Alloy 7 micrographs at 100x of (a) T4 (b) T6 (c) T79 (d) T76 (e) T73.	122
Figure 7.41: Alloy 7 images before and after immersion in modified EXCO solution (a-b) T4 (c-d) T6 (e-f) T79 (g-h) T76 (i-j) T73.	123
Figure 7.42: Alloy 7 potentiodynamic polarizations in deaerated 0.5M NaCl _(aq) solution.	124
Figure 7.43: Alloy 7 maximum depth of penetration observed in cross-section after 96 h of immersion in modified EXCO solution.	124
Figure 7.44: Ageing curve for alloy 8 at 185°C (HRBW).	125
Figure 7.46: Alloy 8 cross-sections after 96 h immersion in EXCO solution at 200x (a) T4 (b) T6 (c) T79 (d) T76 (e) T73. Scale is 50 µm.*	126
Figure 7.45: Alloy 8 micrographs at 100x of (a) T4 (b) T6 (c) T79 (d) T76 (e) T73.	126
Figure 7.47: Alloy 8 images before and after immersion in modified EXCO solution (a-b) T4 (c-d) T6 (e-f) T79 (g-h) T76 (i-j) T73.	127
Figure 7.48: Alloy 8 potentiodynamic polarizations in deaerated 0.5M NaCl _(aq) solution.	128
Figure 7.49: Alloy 8 maximum depth of penetration observed in cross-section after 96 h of immersion in modified EXCO solution.	128
Figure 7.50: Ageing curve for alloy 9 at 185°C (HRBW).	129
Figure 7.52: Alloy 9 cross-sections after 96 h immersion in EXCO solution at 200x (a) T4 (b) T6 (c) T79 (d) T76 (e) T73. Scale is 50 µm.	130
Figure 7.51: Alloy 9 micrographs at 100x of (a) T4 (b) T6 (c) T79 (d) T76 (e) T73.	130
Figure 7.53: Alloy 9 images before and after immersion in modified EXCO solution (a-b) T4 (c-d) T6 (e-f) T79 (g-h) T76 (i-j) T73.	131
Figure 7.54: Alloy 9 potentiodynamic polarizations in deaerated 0.5M NaCl _(aq) solution.	132
Figure 7.55: Alloy 9 maximum depth of penetration observed in cross-section after 96 h of immersion in modified EXCO solution.	132
Figure 7.56: Ageing curve for the validation alloy at 185°C (HRBW).	133
Figure 7.58: Validation alloy cross-sections after 96 h immersion in EXCO solution at 200x (a) T4 (b) T6 (c) T79 (d) T76 (e) T73. Scale is 50 µm.	134
Figure 7.57: Validation alloy micrographs at 100x of (a) T4 (b) T6 (c) T79 (d) T76 (e) T73.	134
Figure 7.59: Validation alloy images before and after immersion in modified EXCO solution (a-b) T4 (c-d) T6 (e-f) T79 (g-h) T76 (i-j) T73.	135
Figure 7.60: Validation alloy potentiodynamic polarizations in deaerated 0.5M NaCl _(aq) solution.	136
Figure 7.61: Validation alloy maximum depth of penetration observed in cross-section after 96 h of immersion in modified EXCO solution.	136

Chapter 1: Introduction

Aluminum alloys are garnering large interest for automotive lightweighting due to their high specific strength properties. There has been a recent push for automakers to reduce their CO₂ production, and vehicle lightweighting is one of the methods to reduce the fuel consumption and carbon footprint. The use of aluminum alloys in vehicles has increased over the years and could be found in various components including engine blocks, structural components, and body closures. A conservative estimate has forecasted the aluminum usage in automobiles to increase by 7.7% by weight from 2016 to 2020 and 18.3% by 2025 in the European market [1]. In 2016, 66 wt.% of the aluminum content in an automobile was near net shaped cast product [1]. Among the aluminum alloy families, the AA7xxx alloys exhibit high strength to weight ratio with high levels of ductility. Therefore, recent investigations in automotive lightweighting and innovative net shaped casting processes to adapt AA7xxx alloys to manufacture near net shaped structural automotive components. Presently, the AA7xxx series alloys are typically used in the form of wrought products, predominantly in the aerospace industry. The difficulty in adapting these alloys to near net shaped casting methods successfully stems from its high susceptibility to hot tearing [2]. Further, the composition of these alloys also presents a high susceptibility to microstructurally induced corrosion [3].

Typically, components made with aluminum alloys gain strength from age hardening, strain hardening, or a combination of the two. However, the near net shaped cast components do not lend themselves to strain hardening processes and hence, cast

Chapter 1: Introduction

products of the AA7xxx series alloys are strengthened through the precipitation reactions during the ageing process. Typically, components of these alloys undergo heat treatments that comprise of solution treatment, quenching, natural ageing at ambient conditions and artificial ageing at an elevated temperature. The solution treatment at an elevated temperature is carried out to homogenize the solute distribution in the cast microstructure, dissolve meta-stable phases that evolve during casting, and favourably alter the morphology of the secondary grain boundary phases. The quench after the solution treatment preserves the supersaturated solid solution (SSSS) of the solute in the primary Al matrix phase and retains the vacancy rich clusters in the matrix to enable atom mobility during the ageing process. These alloys are prone to forming strengthening precipitates in the Al matrix from the SSSS at room temperature immediately after quenching. The ageing treatment at room temperature and/or elevated temperature results a series of precipitation reactions that lead to the formation of coherent, semi-coherent, and subsequently, incoherent precipitates that contribute to the strength of the component by acting as barriers to dislocation movement. During the ageing process, there is a peak value of strength attained by the alloy component, which coincides with the optimum combination of coherent and semi-coherent strengthening precipitates in the Al matrix. However, extending the ageing time beyond this peak value results in the growth of the precipitates via Ostwald ripening (coarsening) and loss of coherency with the Al matrix; this would allow the dislocations to move more freely throughout the material and result in a loss of strength [2,4].

Chapter 1: Introduction

In heat treated AA7xxx alloys, there exists a trade-off between strength and corrosion resistance, which limits the use of aluminum in industrial applications. Cu is added as a solute element to boost the yield strength of the AA7xxx Al alloys; however, the addition of any relatively noble element such as Cu, has a detrimental effect on the corrosion resistance of the cast component [5]. Pitting, intergranular corrosion, and exfoliation corrosion are all examples of localized corrosion phenomena that are enhanced by the addition of Cu to these alloys.

The T6 heat treatment results in the highest strength of the component, however, this also renders the component most susceptible to localized corrosion. Due to the continuous galvanic path that exists along the grain boundaries in the microstructure, the component has low resistance to intergranular and exfoliation corrosion. Ageing the material past the time for T6 treatment, such as, to the T73 condition, improves the resistance to localized corrosion, but also reduces the overall strength of the material [3].

This thesis aims to investigate the localized corrosion of ten Ti-containing AA7xxx series alloys at 5 unique heat treatment conditions (T4, T6, T79, T76, T73) of near net shaped cast components. The four elements that were varied in the alloy compositions of this study include Zn, Mg, Cu and Ti. Zn and Mg are typically added to the AA7xxx alloys to strengthen the components by the effects of solid solution and precipitation in the primary Al matrix [4,6]. However, Zn and Mg are both anodic with respect to Al and could create anodic precipitates that increase corrosion susceptibility [7]. Cu is added to further strengthen the alloy matrix, however, addition of Cu decreases the corrosion resistance by precipitating detrimental secondary phases such as the S-phase (Al_2CuMg) [3]. Ti is added

Chapter 1: Introduction

as a grain refiner to enable net shaped casting of sound components by producing non-dendritic primary phase morphology at the end of the solidification event [8].

The aim of the study is to better understand the role of solute element additions to these alloys coupled with the interactions of critical elements at various heat treatment tempers, on the initiation and propagation of corrosion. Further, the tendencies for exfoliation corrosion in these alloys would be studied. The following are the specific objectives of this project:

- Create an empirical expression for the effect of alloy composition on break down potential, E_b in the T4, T6, and T7x temper conditions, by conducting potentiodynamic polarizations.
- Identify the corrosion mechanisms and relate the initiation sites and propagation to the alloy compositions and heat treatment.
- Examine the corrosion susceptibilities of the Al-6Zn-1.6Mg-2.3Cu-0.25Ti alloy (validation), which was optimized for maximum strength and ductility of the cast component.

The strategy used in this study was to carry out potentiodynamic polarization experiments to quantify E_b as a function of alloy addition and heat treatment, while use a modified version of the standard EXCO experiments to analyse the extent of corrosion on a cast sample surface and correlate the effect of alloy composition and heat treatment to the same

The results of this study have shown that the primary propagation mechanism for the corrosion is significantly different in the cast of near neat shaped components manufactured with a non-dendritic primary Al phase morphology through the addition of

Chapter 1: Introduction

Ti and B for the purpose of grain refinement during solidification. The main difference stems from the selective dissolution of the inter-dendritic regions of the microstructure.

Chapter 2: Literature Review

2.1.0 AA7xxx Series Aluminum Alloys

Aluminum alloys can be defined as one of many designations defined by the Aluminum Association (AA). The designation system for aluminum alloys is extensive and based on primary element composition or heat treatment. This study considers the Al alloys under the designation of wrought alloys [6]. Table 2.1 shows the alloy designation system for Al based wrought alloys depending on the primary alloying element in the composition.

Table 2.1: Main alloying elements in the wrought aluminum alloy designation system [6].

Alloy	Main Alloying Element
1xxx	No major alloying element
2xxx	Copper
3xxx	Manganese
4xxx	Silicon
5xxx	Magnesium
6xxx	Magnesium and Silicon
7xxx	Zinc
8xxx	Other elements

Between age hardening and strain hardening, there exists a variety of processing designations that exist for aluminum alloys. When naming an alloy, identifiers after the first 4 digits signify the post-solidification processing that has been completed on the alloy component. Table 2.2 outlines the common designations used during strain hardening and age hardening treatments. This study only considers only the following age hardening treatments for the cast alloys: such as T4, T6, and T7x. The T7x treatment is an overageing

Chapter 2: Literature Review

treatments and includes the T79, T76, and T73 treatments. Figure 2.1 describes how strength and localized corrosion resistance depends on each T7x heat treatment.

Table 2.2: Common strain and thermal treatment designations [9].

Designation	Definition
<i>Strain Hardened</i>	
H1	Strain hardened
H2	Strain hardened and partially annealed
H3	Strain hardened and stabilized
H4	Strain hardened and painted or lacquered
<i>Thermal Treatment</i>	
T1	Cooled from elevated temperature shaping process and naturally aged to stable condition
T2	Cooled from elevated temperature shaping process, cold worked, and naturally aged to stable condition
T3	Solution heat treated, cold worked, and naturally aged to stable condition
T4	Solution heat treated and naturally aged to stable condition
T5	Cooled from elevated temperature shaping process and artificially aged
T6	Solution heat treated and artificially aged
T7	Solution heat treated and artificially overaged/stabilized
T8	Solution heat treated, cold worked, and artificially aged
T9	Solution heat treated, artificially aged, and cold worked
T10	Cooled from elevated temperature shaping process, cold worked, and artificially aged

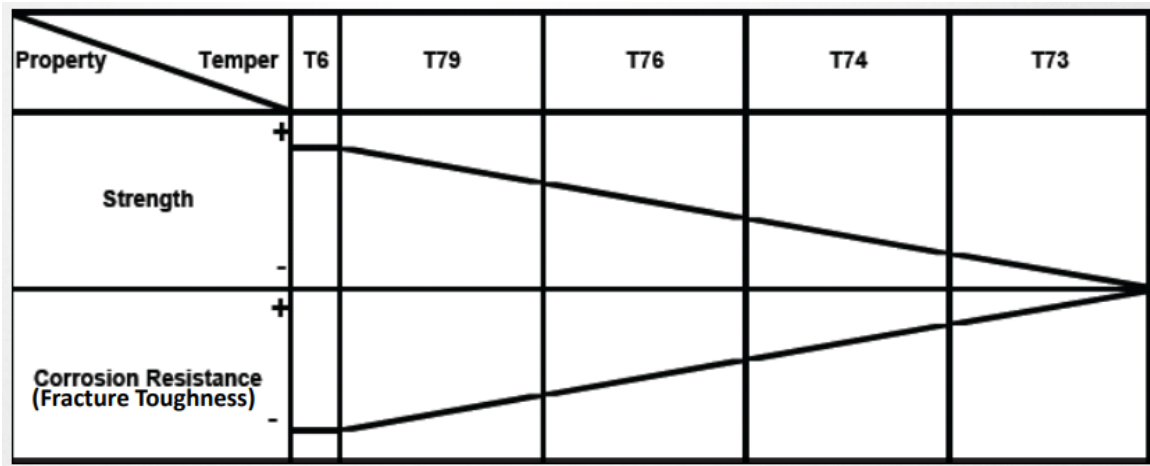


Figure 2.1: General properties associated with T6 and T7x heat treatments [10].

2.2.0 Solidified Microstructure

The near net shaped manufacturing of the high integrity cast components in this study was feasible by altering the morphology of the primary Al phase during solidification from a complex dendritic network to a non-dendritic structure. Figure 2.2 presents a comparison of the dendritic and non-dendritic morphologies of the primary Al phase in the AA7050 alloy with varying Ti content in the as-cast condition.

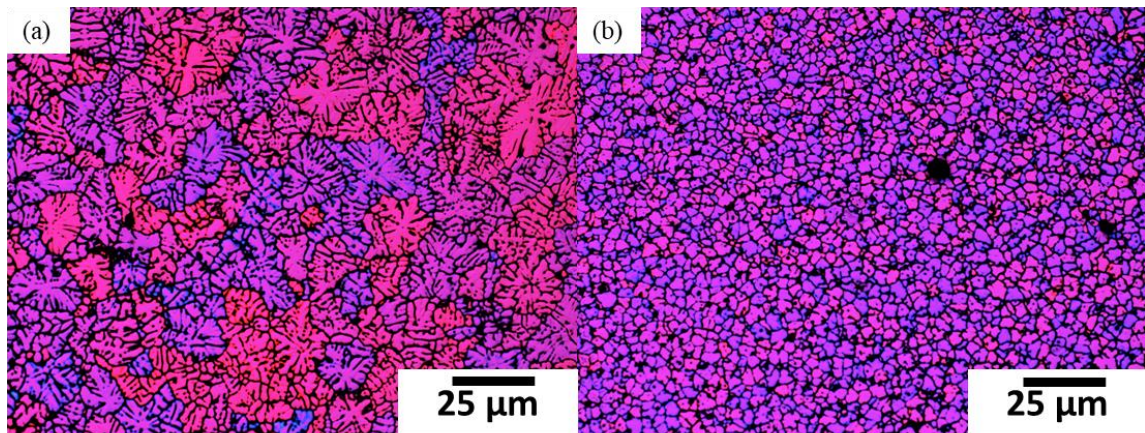


Figure 2.2: Micrographs illustrating the differing morphology AA7050 alloy with (a) dendritic microstructure with no Ti additions (b) non-dendritic microstructure obtained through 0.07 wt% Ti addition to the melt [11].

One of the main deterrents to manufacturing a sound AA7xxx alloy near net shaped casting component is the increased susceptibility to hot tearing during the final stages of solidification, which renders the component defective. The hot tearing phenomenon is significantly alleviated by altering the solidified dendritic morphology of the primary Al grains to a non-dendritic one [2]. Although, the scope of this study is merely to discuss the corrosion performance of these alloys with an initial non-dendritic primary Al phase

Chapter 2: Literature Review

morphology, it is imperative to better understand the broad mechanisms that lead to such a morphology during solidification. In the case of the alloys used in this study, the non-dendritic morphology is facilitated by the addition of grain refiners such as Ti and B to the alloy. However, the intermediate stages during the formation of the seemingly non-dendritic structure of Al is critical to the corrosion performance of the cast component. Figure 2.3 shows a typical image of the primary Al grain in the microstructure of the cast component in this study, wherein, an imprint of equiaxed dendritic structure is present in all the Al grains. The solidification mechanisms that lead to such a unique structure in the shaped cast components of these wrought alloys compositions include copious amounts of athermal nucleation, unconstrained growth of equiaxed dendrites of Al, and the final growth of the Al grains driven by interface curvature effect after solute field impingement. These three phenomena occur in a chronological order and are further explained below.

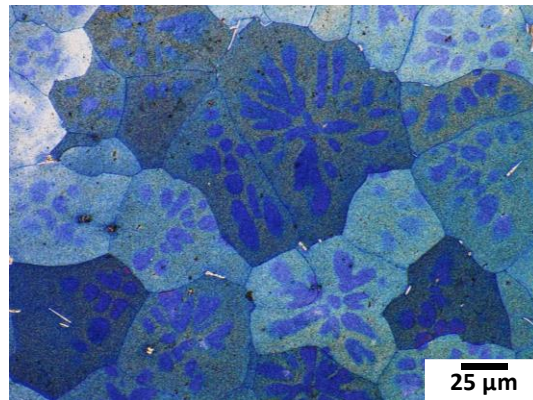


Figure 2.3: Overaged AA7xxx alloy (Al-5.9Zn-1.6Mg-2.7Cu-0.19Ti) etched with Weck's reagent revealing dendritic imprints.

2.2.1 Athermal Nucleation

Ti and B are added to AA7xxx alloys through Al-5wt.%Ti-1wt.%B master alloys to create a fine grain microstructure by heterogeneous nucleation on TiB₂ phase particles. A thin layer (a few atoms thick) of TiAl₃ phase exists on preferential planar ledges of the TiB₂ phase. When the liquidous temperature of the alloy is reached the thin layer acts a heterogeneous nucleation site for primary Al phase. A copious amount of these *athermal nucleation* events are uniformly distributed in the alloy when Ti and B are introduced to the melt followed by a free-growth process of primary Al phase. [12,13]. The extensive nucleation and growth of primary Al is essential for a final non-dendritic microstructure.

2.2.2 Unconstrained Growth

The growth of equiaxed dendrites in the primary Al-phase is due to the mechanism of *unconstrained growth*. The nucleation event releases the enthalpy of fusion within the melt (away from mold walls) resulting in this site being the hottest in the immediate vicinity: the heat is then extracted through the melt and mold walls to the ambient surrounding. Therefore, there exists a negative temperature gradient ahead of the solid-liquid interface (S/L) known as a *thermal undercooling*. Moreover, a *constitutional undercooling* exists ahead of the S/L interface due to the solute redistribution of alloying elements such as Zn, Mg, and Cu in this alloy series. Constitutional undercooling is significantly enhanced by the negative thermal gradient ahead of the S/L interface, which leads to a breakdown of the interface resulting in the growth of the primary Al-phase as an equiaxed dendrite. A third undercooling exists when the S/L interface deviates from

planarity, *curvature undercooling*. Curvature undercooling is caused by the Gibbs-Thompson effect and works to return an unstable interface to planarity; however, the Gibbs-Thompson effect is much smaller than the combination of thermal and constitutional undercooling [14–16]. Figure 2.4 presents a schematic of the equiaxed dendrite morphology of a single primary Al grain solidifying in a melt environment with the three undercooling phenomena. Constitutional undercooling (ΔT_c) and thermal undercooling (ΔT_T) combining to lead to the instability of the growing S/L interface and curvature undercooling (ΔT_r) working towards a planar interface [16].

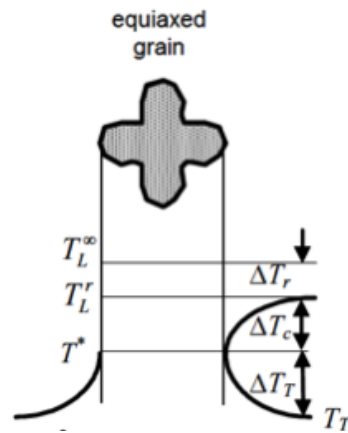


Figure 2.4: Thermal profiles in front of dendritic arm for thermal undercooling (T_T), constitutional undercooling (T_c), and curvature undercooling (T_r) [16].

2.2.3 Solute Field Impingement

When the solute field ahead of two or more dendritic arms impinge the solute gradient ahead of the S/L interface gradually begins to disappear. Moreover, the temperature gradient equalizes between the two dendritic features. This ultimately reduces the driving force for constitutional and thermal undercooling to disappear leaving only

curvature undercooling effect to dominate growth of the primary Al-phase. The curvature effect promotes planar growth: according to the Gibbs-Thompson effect the positive curvatures (dendritic arms) flatten and the negative curvatures (cusps between dendritic arms) grow faster to obtain a virtual non-dendritic microstructure observed in Figure 2.2 (b). The two regimes of growth can be observed in Figure 2.3 where the initial growth dominated by constitutional and thermal undercooling are preferentially etched using Weck's reagent and the surrounding is the regime dominated by curvature undercooling. Copious amounts of athermal nucleation sites increases the likelihood of the impingement phenomenon to occur [10,11].

It is critical to mention here that the segregation of the heavier elements such as Ti within the dendritic imprint can define the boundary between the growth regime controlled by thermal and constitutional undercooling and the growth regime controlled by curvature undercooling. Such segregation in the interdendritic region can then play a critical role in affecting the corrosion performance of AA7xxx cast alloys grain refined by this method.

2.2.4 Solidifying Cast vs Wrought Alloys

The solute impingement phenomenon explained above does not necessarily occur in all primary Al alloys. The amount of eutectic phase present at the end of solidification is critical to the presence of dendritic imprints in the microstructure. Cast alloys solidify with significantly more eutectic phase in the microstructure than wrought alloys. Figure 2.5 shows a Pandat solidification simulation of a cast Al alloy (A356.2) vs a wrought Al alloy (AA7050) [11]. The figure shows that at the end of solidification in the cast alloy

there is approximately 50% liquid remaining to solidify as the eutectic phase, whereas, the wrought alloy has less than 10% liquid remaining. The phenomenon of solute impingement requires a large fraction of solidification to occur promoting the dendritic tips to come into proximity to one another. In a cast alloy the solidification stops near 50% solid fraction: there exists a large amount of eutectic phase between each dendrite maintaining the solute gradient ahead of the dendritic tip and ultimately constitutional undercooling. In a wrought alloy, there would not be sufficient eutectic phase between the dendritic tips resulting in the loss of a solute gradient and constitutional undercooling [11].

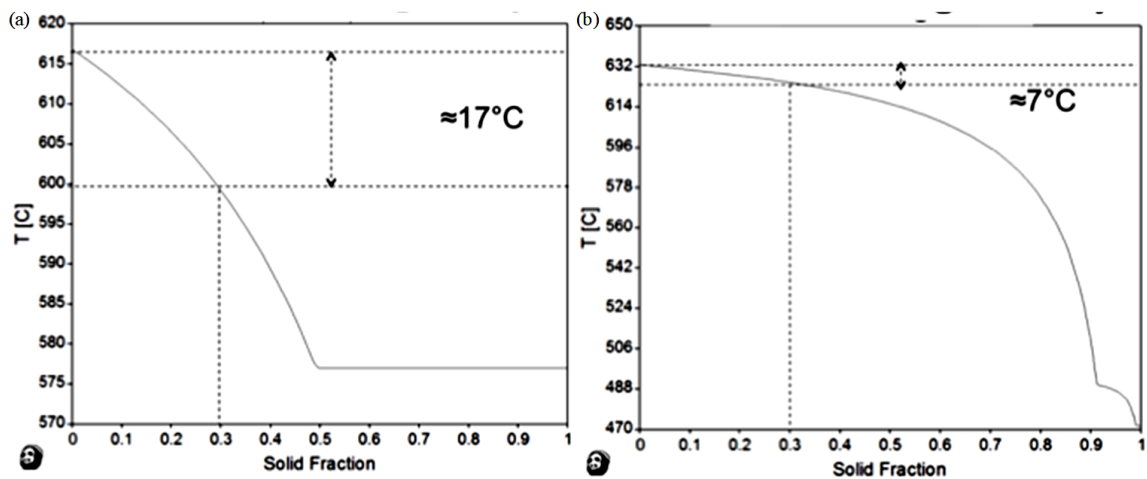


Figure 2.5: Simulated solid fraction development of (a) A356.2 casting alloy and (b) AA7050 wrought alloy during solidification [11].

2.2.5 Abnormal Grain Growth Characteristics

During the solution heat treatment of these alloy components, thermally activated abnormal grain growth (grain coarsening) occurs in the microstructure to result in distinctly different size regimes of primary Al grains. During grain growth, large grains grow at the expense of small grains leading to a uniform grain size. However, some materials exhibit

abnormal grain growth where some grains grow more rapidly than others. At the end of abnormal grain growth, the grain size could also be relatively uniform, but most likely the distribution is bimodal with two distinct size regimes of large and small grains. Abnormal grain growth stems from the presence of second phase particles and high angle grain boundaries, which limit the uniform growth of grains (normal grain growth) [18,19]. It is notable that the contribution of the grain size to the final yield strength of the heat treated cast AA7xxx alloys is negligible at about 3% and hence, the grain size distribution, be it normal Gaussian or abnormal bimodal has insignificant effect on the final yield strength of the component [2]. However, abnormal grain growth significantly affects the fatigue life of components [20].

2.3.0 Heat Treatments

Casting near net shaped components requires that the material is age hardened to promote the formation of strengthening precipitates in the Al matrix [21]. Typically, there are three required steps for age hardening, namely, solution treatment, quenching and ageing.

In solution heat treatment (SHT), the temperature is held at a safe value below the first melting point of the alloy, but high enough to homogenize the solute elements. An ideal SHT of a primary single-phase alloy such as the AA7xxx alloys, would completely homogenize all solute segregation, dissolve all meta-stable secondary phases back into the Al matrix and favourably alter the morphology of the intergranular phases by rounding off sharp edges and corners. However, certain heavier elements such as Cr, Zr, V and Ti have

Chapter 2: Literature Review

sluggish mobility during the SHT and hence, may not completely dissolve and homogenize in the Al matrix [3]. A solution treatment at 515°C for 1 h was shown to be too high and resulted in incipient melting of meta-stable phases, but was not high enough to dissolve Fe-containing particles in AA7150 (Al-6.2Zn-2.1Mg-2.4Cu) [22]. Main alloying elements such as Zn, Mg, and Cu diffuse easily in the primary Al matrix and are typically homogenized except for a few intermetallic particles. SHT has a significant role on localized corrosion as it directly affects the secondary phases that are present in the material. In AA7150 the volume fraction of particles was shown to reduce from 4.3 % in the as-cast state to 0.8 % after SHT, which resulted in a reduction in the number of pits from 335 to 46 in a 300 x 228 μm 2D field of view [22].

The rate of the quench after SHT influences the number of vacancy-rich clusters (VRC) that are retained in the primary Al matrix. The VRC is critical to create mobility of the atoms that come together to form the initial Guinier-Preston (GP) zones in the matrix. Higher quench rates result in higher concentration of VRC leading to more volume fraction of GP zone during ageing at room temperature with a smaller size of these zones, as well [2,23].

There are two types of ageing: natural (room temperature) and artificial (elevated temperature). Increasing the ageing temperature increases the kinetics of ageing. Most processes include at least one artificial ageing step, and typically, these are multi-step processes. Ageing has a significant effect on the size and distribution of the strengthening precipitates, $\text{Mg}(\text{Zn},\text{Al},\text{Cu})_2$ in the case of AA7xxx alloys Marlaud et al. completed an extensive study utilizing TEM, APT and ASAXS to study the size and composition of

precipitates during ageing of AA7150 and AA7449 at 160°C. It is notable that the solubility of Cu in the strengthening precipitates increases, while that of Zn decreases with increased ageing periods at elevated temperatures. Moreover, the solubility of both Cu and Zn, in these precipitates increase with higher initial Cu and Zn contents in the alloy composition, respectively [24].

2.4.0 Precipitation Sequence

The precipitation sequence of AA7xxx alloys after SHT is complicated. It is generally regarded to be the following:

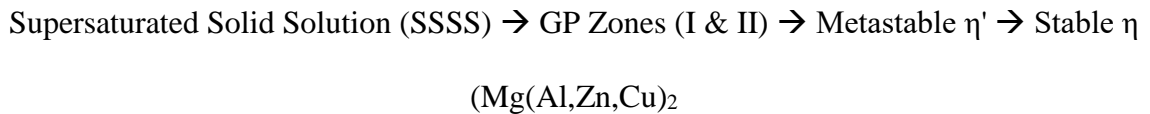


Figure 2.6 (a) and (b) presents the equilibrium phase diagram simulation with all the solid-state transformations during the precipitation of the strengthening phases in the primary Al matrix and a schematic showing the temporal sequence of the precipitates along with their relative free energy values, respectively. The SHT of wrought AA7xxx alloys eliminates Mg, Cu, and Zn segregation since these are predominantly primary single-phase alloys.

Aluminum alloys have multiple steps in the precipitation sequence due to the high barrier to nucleation of the incoherent stable precipitates. The addition of Cu to the ternary Al-Zn-Mg system does not change the overall sequence of precipitation, but rather, alters the kinetics of the process in addition to altering the size and distribution of the precipitates in the Al matrix [25]. Upon quenching after SHT, the retained VRC distributed in the primary Al matrix facilitates the evolution of the coherent solute cluster zones known as

GP zones [26,27]. GP zones formation is followed by the formation of a semi-coherent transition phase (η'). These transition phases are less stable, but more coherent than the terminal stable phase (η) (Figure 2.6 (a)). The transformation sequence stops when the stable precipitates form. These precipitates have the lowest free energies [21,28,29].

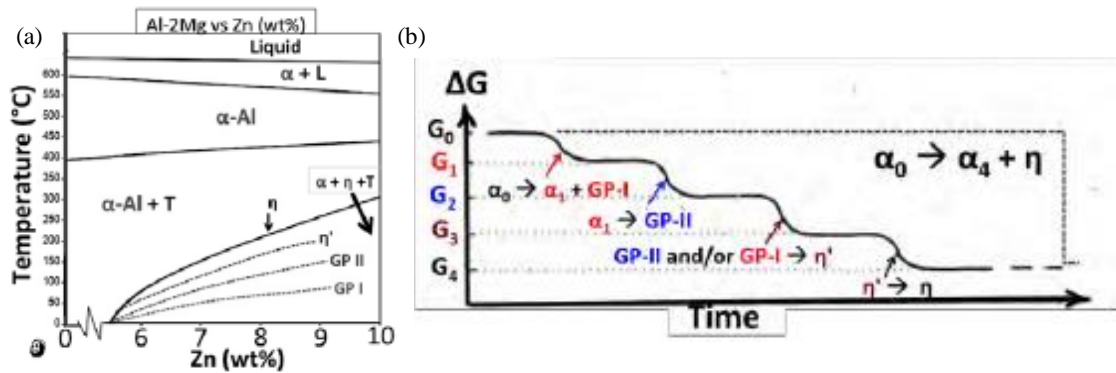


Figure 2.6: Schematic diagrams illustrating (a) the stability of precipitates in an Al-2Mg-Zn system (b) the free energy change with the formation of metastable precipitates [2].

It is widely reported that two GP zones can co-exist as GP-I and GP-II zones. As shown in Figure 2.6, GP-I zones are likely to form first from the supersaturated solid solution (SSSS) followed by the formation of GP-II zones. The GP-II zones evolve in one of two ways at an ageing temperature of around 70°C; the existing GP-I zones transform to GP-II zones or GP-II zones could directly nucleate and grow from the SSSS [9,10,30,32]. The addition of Cu to the alloy (in the SSSS in particular) influences the precipitation reaction such that the kinetics of the sequential transformation process is enhanced and certain amount of Cu atoms dissolves in each of the precipitates, which results in a significantly reduced mean precipitate size and increased distribution of precipitates throughout the Al matrix. The Cu atoms uniquely tie down the Mg atoms from diffusion

Chapter 2: Literature Review

in the Al matrix, which results in a more distributed evolution of the GP zones that continue on to form smaller and more distributed η' precipitates [24,25].

The ratio of Zn/Mg plays a major role on the ageing characteristics of AA7xxx alloys. Since the strengthening precipitate is based on $\text{Mg}(\text{Al,Zn,Cu})_2$ derivatives, for every 1 atom of Mg there needs to be 2 atoms of Zn available with some Al and Cu atoms substituting the Zn atom locations in the lattice. With weight ratios of Zn/Mg below 2, it was observed that the peak strength and number density of precipitates increased [33].

In summary, the primary Al matrix contains GP zones in the as-quenched state after SHT and the GP zones will continue to form in the matrix in ambient condition during natural ageing (T4). When the alloy component is aged at an elevated temperature after natural ageing, the hardness and yield strength increase because of increased formation of the GP-II zones and η' precipitates. Peak values of hardness and yield strength are reached when an optimum volume fraction of these two phases exist in the alloy matrix and the time taken (T6) for attaining the peak strength depends on the initial alloy composition and the state of the SSSS after SHT. Past the T6 treatment the formation of the incoherent and terminal η precipitates increases from T6 to T73 treatment and results in a decrease in hardness and strength values because of the increased size and number density of the terminal η precipitates forming from the η' precipitates during the overageing treatment past the T6.

2.5.0 Secondary Phases

Secondary phases have a significant effect on the localized corrosion of aluminum alloys. They could be anodic, cathodic, or both with respect to the matrix and precipitate free zone (PFZ). They could act as initiation sites for corrosion and enable the propagation of the same via a variety of mechanism that are explained later in this thesis. Birbilis and Buchheit [7,34] compiled a list of common intermetallic phases and their corrosion potential extracted from literature and experimental measured using the microcapillary electrochemical cell technique. Table 2.3 shows a subset of intermetallic compounds reported from their work. Birbilis et al. [35] reported that in AA2024-T3, there were variants of microconstituents with their own Volta potentials implying that the list given in Table 2.3 is not complete and, thus should merely serve as a reference.

Table 2.3: Subset galvanic series of compounds common in 7xxx series Al alloys [7,34].

Stoichiometry	Phase	Corrosion Potential (mV_{SCE}) (0.1M NaCl)
MgZn ₂	η	-1029
Al ₂ CuMg	S	-883
Al (99.9999)		-823
7X75 Matrix		-799
Al ₂ Cu	θ	-665
Al ₃ Ti	β	-603
Al ₇ Cu ₂ Fe		-551
Al ₃ Fe	β	-539
Cu (99.9)		-232

Cu-containing phases are typically cathodic with respect to the matrix and cause galvanic interactions leading to initiation of corrosion. Al₇Cu₂Fe and Al₂CuMg are the most common Cu-containing intermetallic phases that exist in a T4 temper and can cause stable pitting [36]. The S-phase (Al₂MgCu) particles are present in most Cu-containing

Chapter 2: Literature Review

AA7xxx alloys. It is very difficult to dissolve these particles in solid solution because the solvus temperature is close to the SHT temperature (475°C) and the melting temperature of these particles is 488°C [37]. Figure 2.7 presents a schematic of the corrosion mechanism involving the S-phase particles interacting with the corrosive environment. The schematic in Figure 2.7 is valid for the AA2xxx series alloys (Al-Cu-Mg) [38–40], however, the results of this thesis demonstrate that the mechanism is valid for the cast AA7xxx alloys under consideration. At the onset of corrosion these particles are anodic relative to the matrix, but, as selective dissolution of the Al and Mg in the phase occurs leaving behind Cu-rich clusters, these particles eventually become cathodic relative to the matrix. Phenomenon leads to peripheral trenching of the alloy matrix directly adjunct to the Cu-rich clusters. During dealloying, Cu fragments are released and redeposited onto the matrix surface surrounding the S-phase particle. The redeposited Cu serves as an active cathodic site, which is required to sustain the adjacent enhanced anodic dissolution of the matrix. Increasing flow in the corrosive solution increases the range of transport for the Cu away from the S-phase particles, creating a wider network of cathodic sites. [17,18,42–44].

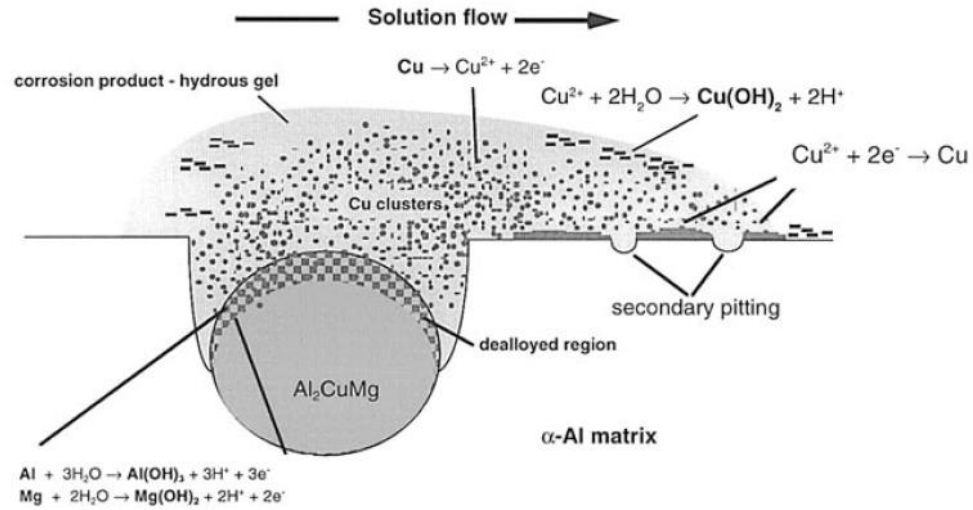


Figure 2.7: Schematic of corrosion mechanism present in the S-phase [44].

Another common intermetallic phase (IMP) in aluminum alloys is the $\text{Al}_{13}\text{Fe}_4$ phase, which is sometimes referred to as Al_3Fe . In AA7xxx alloys, these particles have a plate-like morphology. SHT do not dissolve these particles back into solid solution [37]. Although the Fe-containing particles have a more noble potential than the Cu-containing phases in the microstructure, the Cu-lean alloys are not as susceptible to pitting corrosion as the Cu-rich alloys [36], which implies that the Cu-containing phases play a key role in pitting and therefore initiation mechanisms: also, this implies that a mere comparison of phase potentials may not be entirely sufficient to explain the corrosion tendencies of these alloys. Similar to the S-phase particle dealloying mechanism, Fe-containing particles can also dealloy. The dissolved Fe can redeposit onto the Al matrix, meeting the conditions necessary for autocatalytic pitting [45]. Seri and Tagashira [46] have shown that in an Fe-Al alloy, Al_3Fe phase particles can create an active-passive region prior to breakdown potential (E_b) in a cathodically-treated sample. During cathodic treatment, Al is selectively

dissolved on the surface leaving behind clusters of atoms rich in Fe as residue. During potentiodynamic polarization these Fe-rich residues oxidise to form $\text{Fe}(\text{OH})_2$ creating a small active-passive region in the potentiodynamic curve [46].

2.6.0 Precipitate Free Zone (PFZ)

Grain boundary precipitates and some intermetallic particles form a precipitate free (solute-depleted) zone (PZF) along the grain boundary or around a particle. As precipitates and particles coarsen they deplete solute from the surrounding areas leaving behind areas completely depleted of solute atoms. The PFZ size is directly proportional to the vacancy concentration in the matrix [37]. The formation of PFZ is significant in the mechanisms of corrosion as they have a direct galvanic interaction with the solute-rich adjacent grain boundary precipitate or intermetallic particles.

2.7.0 Corrosion Mechanisms in Aluminum Alloys

High strength AA7xxx alloys are susceptible to a variety of corrosion mechanisms: intermetallic particle trenching, intergranular corrosion, intergranular stress corrosion cracking, corrosion rings, domes, and exfoliation corrosion are the primary modes that have been reported. Intermetallic particle trenching is often a precursor to the other corrosion modes. The galvanic interaction between intermetallic particles and the surrounding matrix lead to further propagation of corrosion [36] Literature background on the stages in the localized corrosion of AA2024-T3 alloy is shown in Figure 2.8, which is a temporal schematic description of the processes leading to a stable pitting. Intermetallic particle

(IMP) trenching is the first mode observed. Once intermetallic particle trenching creates stable pits, further modes can be activated serving to propagate corrosion further [39].

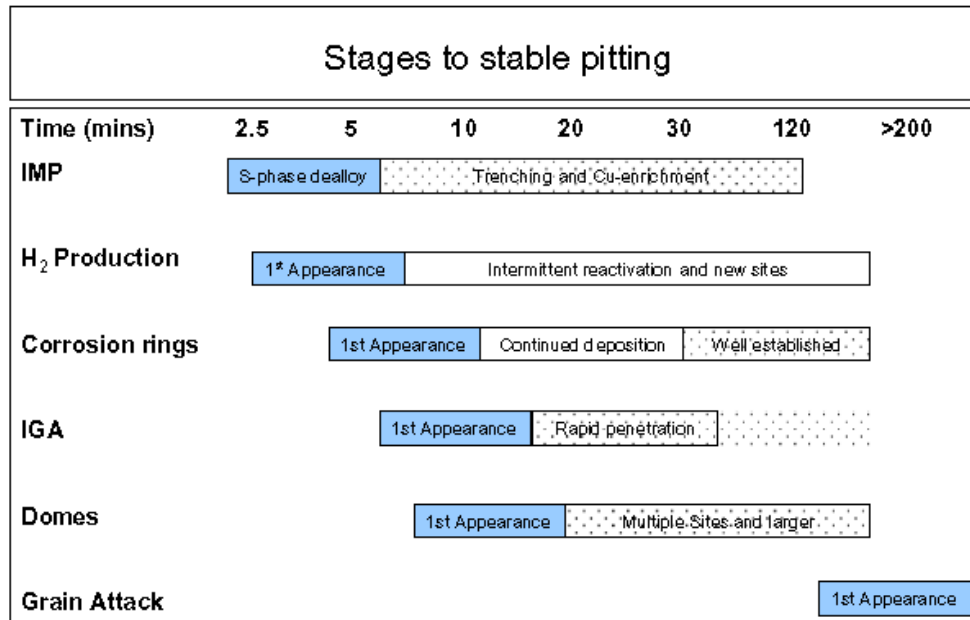


Figure 2.8: Stages to stable pitting in AA2024-T3 [39].

2.7.1 Intergranular Corrosion

Intergranular corrosion is a common occurrence in high strength aluminum alloys. Microgalvanic cells are present along grain boundaries due to the high electrochemical differences between grain boundary precipitate particles, intermetallic particles, PFZs, and Al matrix, all of which promote localized attack at the grain boundaries. Intergranular corrosion is highly dependent on alloy composition and heat treatment. An alloy in T4 condition is typically free of intergranular corrosion as most alloying elements are in solid solution reducing the secondary phases that exist along the grain boundary.

Kairy et al. [47] developed a phenomenological intergranular corrosion model for the AA6xxx series alloys wherein the detrimental interactions between grain boundary features and the matrix are highlighted; the schematic of the mechanism is shown in Figure 2.9. Of the nine alloys considered in their study, they were able to identify the primary galvanic interaction between intermetallic particles and specific grain boundary features based on alloy composition. The PFZ acts either as a cathode or anode site, depending on compositions of the grain boundary precipitate particles. It was reported that a Cu film existed in Cu-rich alloys along the grain boundaries that could act as the cathodic portion of a “nano”galvanic cell with the PFZ. A high diffusion rate of Cu in Al leads to the formation of a Cu film along the grain boundary. It was concluded that increasing Cu content and Si/Mg ratio increases the severity of intergranular corrosion at identical heat treatments. For Cu-rich alloys, the intergranular corrosion susceptibility depends on the temper, with the highest susceptibility exhibited by the peak aged T6 temper, followed by a decrease in susceptibility with overageing (T7X tempers). It has been extensively reported that the grain boundary precipitates coarsen during overageing, resulting in larger inter-particle spacing. The larger spacing creates a discontinuous galvanic pathway to mitigate the intergranular corrosion[24,47,48].

Further to initiation of intergranular corrosion at intermetallic particles, it has been reported that intergranular corrosion can also occur on grain boundaries that do not contain precipitate particles. Zhou et al. [49] completed work on AA2xxx series alloys showing that intergranular corrosion does not occur along the centre-line of a grain boundary, but

rather the path of attack is skewed towards grains with higher stored energy indicating that grains with high relatively level of defects are more susceptible to corrosion [3,49].

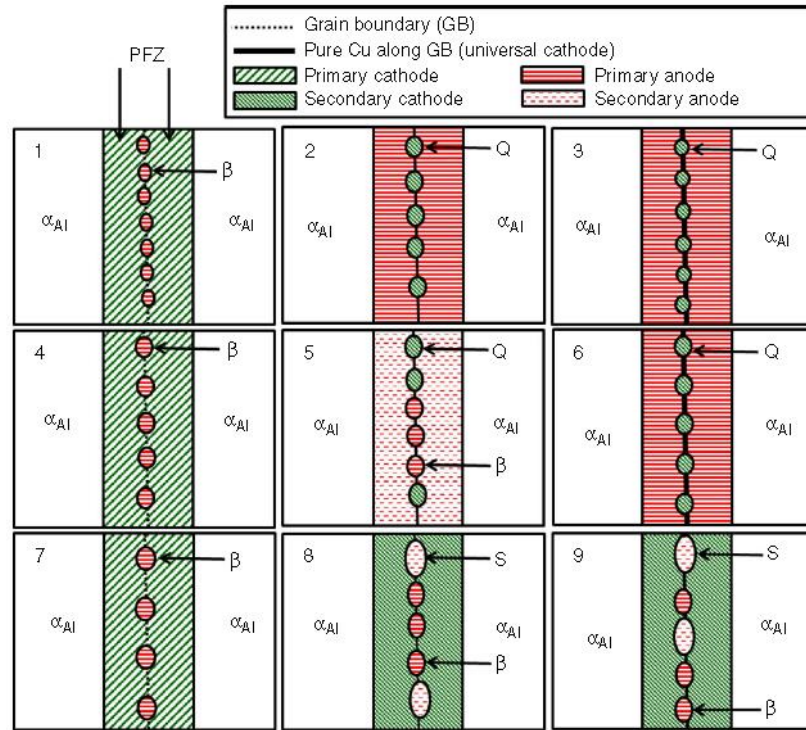


Figure 2.9: Phenomenological intergranular corrosion model developed by Kairy et al. using nine various compositions of the AA6xxx series alloys [47].

2.7.2 Intergranular Stress Corrosion Cracking

Intergranular stress corrosion cracking (SCC) is the brittle fracture along the grain boundaries under a constant stress well below the yield stress of the material in a corrosive environment [50]. Intergranular corrosion is a prerequisite for SCC to occur, therefore, the same mitigation techniques discussed in the previous section will apply for SCC [51]. For AA7xxx alloys only alloys that contain an appreciable amount of alloying element like Zn, Mg, and Cu are susceptible to SCC. Figure 2.10 is a summary of the effect of heat treatment

and alloying element concentration on the crack growth rate of various AA7xxx alloys compiled by Holroyd et al. [52]. According to the summary ageing the alloy beyond the T6 temper to T76 has significant benefits nearly independent of composition. Alloy Cu content between 0.8 and 1.8 wt% has a significant decrease in SCC susceptibility. Moreover, alloys with a Zn/Mg weight ratio of approximately 2 and an excess Mg content between 0.5 and 1.5 wt% would provide the optimal stress corrosion properties [52].

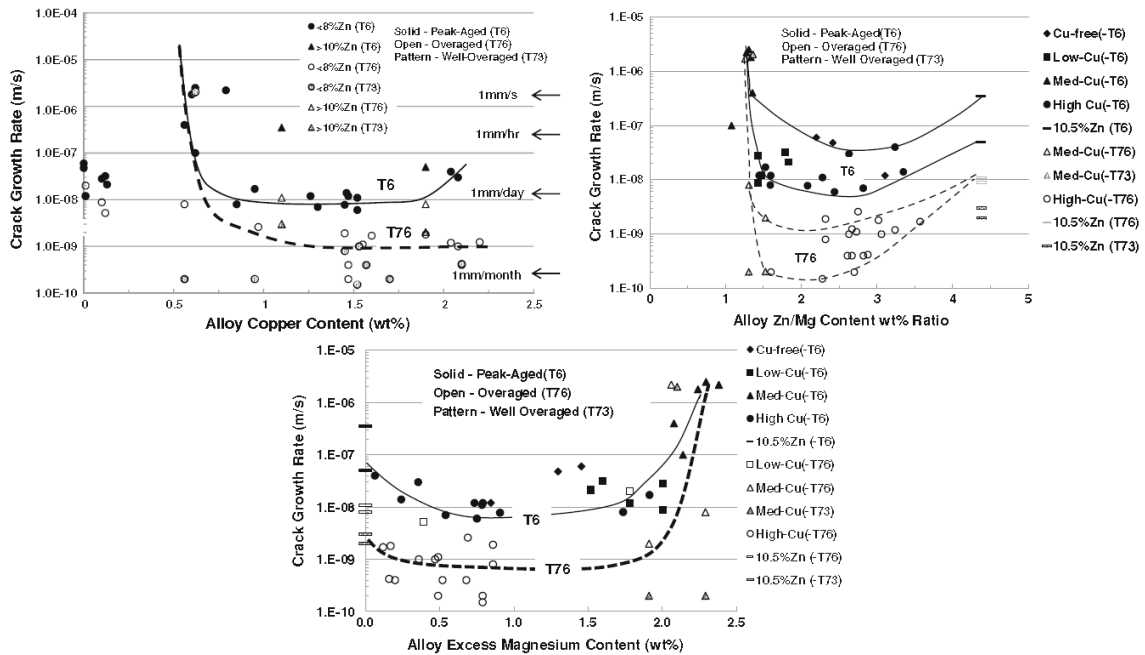


Figure 2.10: Effect of alloying element content and heat treatment on the crack growth rate of Al-Zn-Mg-Cu alloys during SCC in 0.6 M NaCl_(aq) solutions compiled by Holroyd et al. [52].

2.7.3 Corrosion Rings and Clustering

The localized corrosion properties of AA2024-T3 was studied extensively to understand the formation of stable pitting [38–40]. It was discovered, that isolated intermetallic particles do not lead to stable pitting. Even though dealloying of the S-phase

particles and trenching is evident, stable pits do not necessarily form. They concluded that stable pitting requires clusters of intermetallic phase particles to be present. Clustering of intermetallic particles (cathodic with respect to the matrix) creates a large area within a corrosion ring that acts as a global cathodic site due to Cu enrichment from the S-phase particle dealloying. Figure 2.11 presents a microstructure model that explains the phenomena of corrosion ring formation from particle clustering [39]. Each cathode intermetallic phase particle has a trench along its interface with the matrix due to corrosion. Among a cluster of such intermetallic particles in the intergranular region, the surface of the microstructure serves as the cathode while the matrix at the bottom of the trenches serves as the anode. As pitting (trenching) continues and trenches become deeper, the anode moves deeper into the material while continuously maintaining an active galvanic couple with the cathodic surface. This galvanic couple leads to continuous intergranular corrosion and stable pitting and is referred to as *co-operative corrosion*.

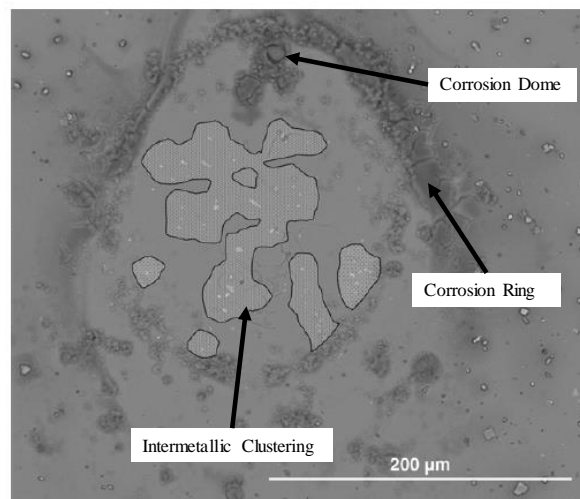


Figure 2.11: Image of intermetallic clustering surrounded by a ring of corrosion product in AA2024-T3 [39].

2.7.4 Exfoliation Corrosion

Exfoliation corrosion is a type of corrosion limited to high strength wrought alloys with an elongated grain structure. Most often observed in wrought AA2xxx, AA5xxx, and AA7xxx alloys, exfoliation corrosion is a type of intergranular corrosion that causes leafing of elongated grains. As intergranular corrosion progresses, corrosion products deposit within the gaps between grains that are left behind by corrosion, which then expand upon drying causing the exfoliation of elongated grains [53]. Hydrogen uptake near the grain boundaries has also been reported to assist in exfoliation corrosion. It has been suggested that the fracture of grain boundaries is due to the hydrogen embrittlement and the volumetric expansion serves only to produce the leafing structure [53–56]. The volume expansion occurs near the surface of the plate material can also cause external component coatings to blister and fail [57]. Moreover, exfoliation corrosion can reduce the intact cross-sectional area and, hence reduce the directional mechanical properties [58]. Elongated grains are necessary for exfoliation corrosion to occur. Equiaxed grains are believed to promote the formation of pits, whereas elongated grains, with higher aspect ratios, promote the formation of blisters that are the precursors to exfoliation corrosion [53,59]. Since exfoliation corrosion is a subset of intergranular, as ageing continues past the T6 temper, the resistance to exfoliation corrosion increases due to a discontinuous galvanic path along the grain boundaries [48].

2.8.0 Breakdown Potential, E_b

During potentiodynamic polarization, a sharp increase in anodic current density at relatively low applied potentials is considered as a breakdown potential event. In AA7xxx alloys, many studies have shown the existence of one or two values of E_b . Zhao et al. [60] reported that the first breakdown in a T6 temper sample and attributed it to the dissolution of a solute-rich active surface layer created during polishing [60]. It was mentioned that the double breakdown feature is absent in Cu-lean alloys and in alloys with an overaged (T73) heat treatment temper. Wang et al. [61] discovered that solute rich layers still exist after polishing a Cu-lean alloy, but with low Cu in the bulk alloy, no galvanic interaction between the surface and bulk exist for a double breakdown potential to be observed. In the overaged condition, it is reported that Cu content depletes in the Al matrix as Cu migrates towards the grain boundaries. This reduces the galvanic interactions between the bulk alloy and surface layer in the T73 temper condition [61].

The effect of alloying elements on the pitting potential/breakdown potential has been subject to a variety of studies. Muller et al. [62], showed that the pitting potential in a Al-Cu system increased with increasing Cu content. They attributed the increase to the formation of Cu-depleted zones along the grain boundaries [62]. Wang et al. [61] discussed the relationship between Cu content and temper on the localized breakdown potential in AA7xxx alloys. In Cu-lean alloys, Zn and Mg are the only significant alloying element in the bulk solution. This creates a much more active bulk solution compared to one containing Cu. The breakdown potential of Cu-containing alloys is more noble compared to Cu-lean alloys. A similar argument is made for overageing tempers. During heat

Chapter 2: Literature Review

treatment to the peak age (T6) condition, Zn continually move from the SSSS to the evolving strengthening precipitate particles, thus, increasing the breakdown potential of the alloy. Past the peak age (T6) temper and during overageing (T7x) tempers , the breakdown potential decreases, because the Cu content increases in the strengthening precipitate particles during overageing [61]. Although, both Cu and Zn leave the solid solution during overageing treatment, the depletion of Cu from the matrix has a greater impact on the breakdown potential [36,61]. This is further validated by the continuous increase of the breakdown potential in Cu-lean alloys, between the naturally-aged (T4) temper and highly overaged (T73) tempers caused by the continual depletion of Zn from the Al matrix, making the bulk more noble [36,63].

Chapter 3: Experiments

3.1.0 Materials

Based on the philosophy of a Taguchi L9 orthogonal design matrix [64], nine AA7xxx series alloys were chosen by varying compositions of Zn (3.5-6.5 wt%), Mg (1.5-2.5 wt%), Cu (0-2.4 wt%), and Ti (0.06-0.24 wt%), as critical independent parameters. The composition of the validation alloy (V) in this study was borrowed from another study carried out in tandem with these alloys [65], wherein, statistical analyses of experiment data lead to the validation alloy composition to be the ideal for highest values of Ultimate Tensile Strength (UTS), Yield Strength (YS) and elongation, combined in the cast component. Two casting methods were used; one set of alloys were cast into a rod form via the tilt pour gravity casting (TPGC) method so as to determine the transient hardness values during the ageing process from the SSSS state in the T4 temper and the second set of alloys were cast into plate form using a permanent mould for corrosion testing and microstructural analyses. The outlined portion of Figure 3.1 (a) illustrates the area sectioned for the transient ageing studies. The permanent mould plate (10 cm × 20 cm × 0.635 cm) along with the section lines are shown in Figure 3.1 (b). The DOE target and actual composition of each alloy as determined by GDOES are presented in Table 3.1. A full listing of all the major and trace elements in the alloys shown in Table 3.1, is presented in the Appendix. Notably, the standard deviations in the measured values of elements in the alloys were nominal.

Chapter 3: Experiments

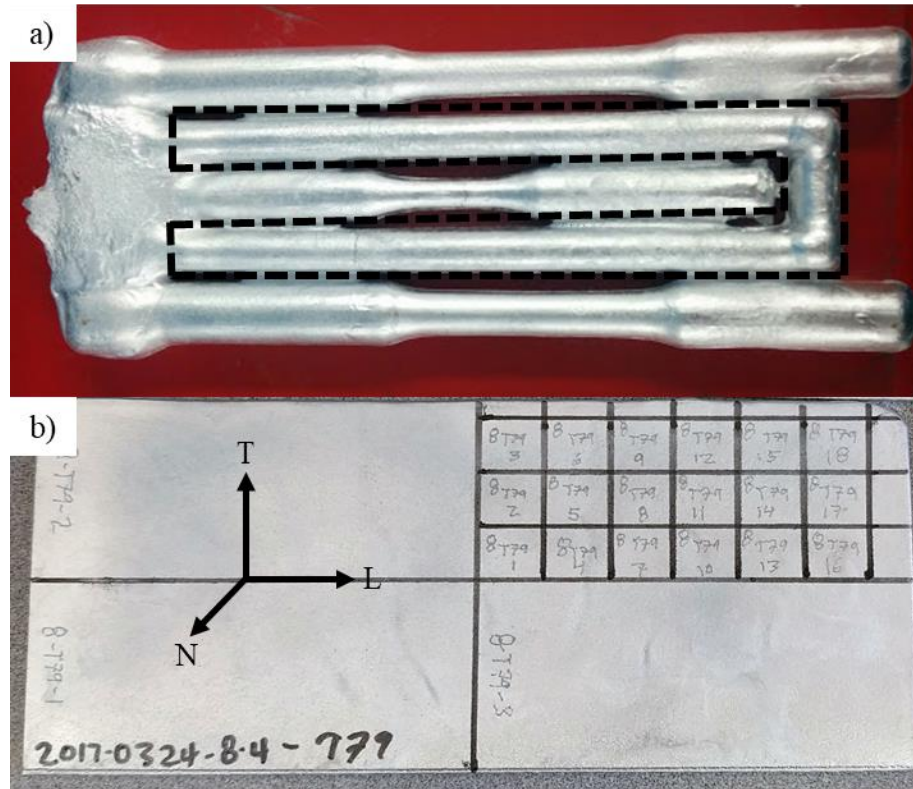


Figure 3.1: Typical cats samples in this study (a) TPGC sample outlining “U-shaped” sections used for ageing coupons (b) Permanent mould casting of corrosion plate used for alloy 8 T79 tests outlining sections used for corrosion and microstructure analyses.

Table 3.1: Target and actual compositions of each alloy as determined by GDOES. A denotes the composition of the TPGC samples and B denotes the composition of the permanent mould plates.

Alloy	Zn (wt%)			Mg (wt%)			Cu (wt%)			Ti (wt%)		
	Target DOE	GDOES A	GDOES B									
1	3.5	3.2	3.4	1.5	1.4	1.5	0	0.0	0.1	.06	.06	.04
2	3.5	3.2	3.8	2	1.8	2.0	1.2	1.1	1.5	.15	.17	.12
3	3.5	3.4	3.6	2.5	2.4	2.5	2.4	2.7	2.9	.24	.22	.21
4	5	4.8	5.1	1.5	1.5	1.6	1.2	1.3	1.4	.24	.17	.25
5	5	4.8	5.5	2	2.0	2.2	2.4	2.7	3.0	.06	.09	.05
6	5	4.7	5.0	2.5	2.1	2.1	0	0.0	0.1	.15	.12	.13
7	6.5	6.0	7.0	1.5	1.4	1.7	2.4	2.1	3.0	.15	.57	.14
8	6.5	6.0	6.9	2	1.8	1.9	0	0.0	0.2	.24	.26	.07
9	6.5	6.5	6.5	2.5	2.3	2.4	1.2	1.2	1.3	.06	.06	.04
V	6	6.0	5.9	1.5	1.6		2.4	2.5	2.7	.24	.32	.19

3.2.0 Transient Hardness

The “U-shaped” cast specimen from the TPGC mould were each sectioned into 21 elliptical ageing coupons ($h \times a \times b = 1.5 \text{ cm} \times 1.6 \text{ cm} \times 1.3 \text{ cm}$). Each of the two elliptical surfaces were polished flat to a 500 grit surface finish prior to thermal treatment. Figure 3.2 presents a graphical schematic of the entire heat treatment of the samples for the transient hardness study during ageing. Each specimen underwent a two-step solution heat treatment (ramp from 25°C to 450°C at 60°C /h, hold for 24 h, ramp from 450°C to 475°C at 5°C /h, hold for 24 h), followed by quenching in water held at around 15°C. The quenched samples underwent natural ageing at ambient conditions for 24 h, followed by a two-step artificial ageing (120°C for 24 h, step to 185°C, hold up to 96 h). Peak solution heat treatment temperature was chosen to be 475°C as incipient melting of secondary phases has been shown to occur in samples prepared with solution treatments temperatures above 483°C [2]. The aged samples were quenched in water, maintained at around 15°C. During the second stage of artificial ageing, the coupons were removed from the furnace at periodic intervals and subsequently water quenched to generate ageing curves.

Chapter 3: Experiments

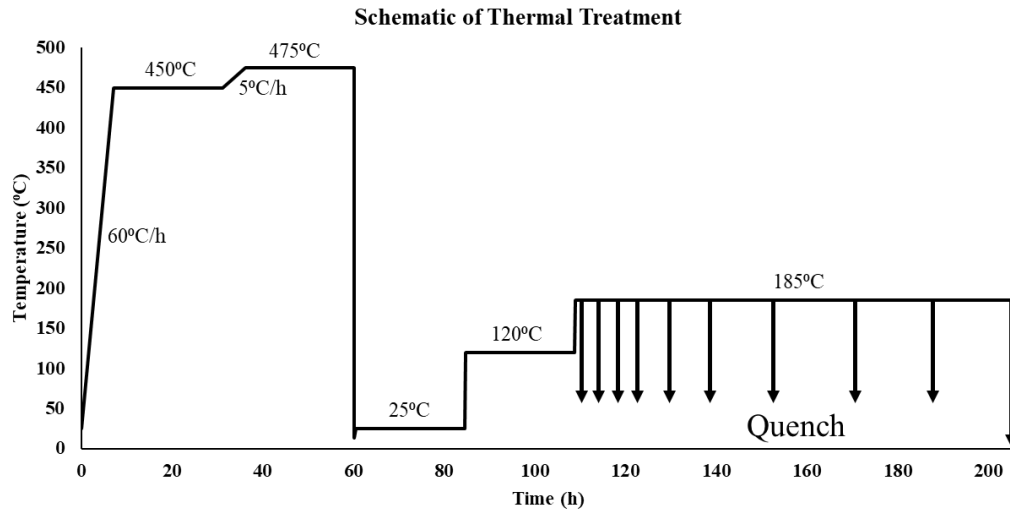


Figure 3.2: Graphical schematic of the heat treatment of the alloy castings used to acquire transient ageing curves.

Transient hardness during ageing was measured using Rockwell hardness test in accordance with the ASTM E18-17e1 standard [66]. Notably, the hardness measurements were initiated immediately after quenching the samples so as to avoid any interference from the natural ageing phenomenon. Rockwell hardness scale B (1/16 inch (1.6 mm) carbide ball indenter and 100 kg weight) was used for alloys 2 to 9 and the validation alloy. Due to the low strength of alloy 1, scale E was used; 1/8 inch (3.2 mm) carbide ball indenter and 100 kg weight. Prior to making hardness measurements on the elliptical coupons, daily measurements were made on verification blocks, one per indenter, to ensure day-to-day repeatability. Six measurements were conducted on each flat surface of the elliptic cylinder for a total of 12 per coupon. Transient hardness graphs were compiled for each alloy. The temporal definitions of the T4, T6, T79, T76, and T73 tempers were determined from the nature of the transient hardness data.

T4 temper was the same for all alloys; solution treatment followed by 96 hours of natural age. The T6 and T7x tempers depended on the individual alloy compositions. T6 temper was defined as the peak hardness data of the ageing curves. T73 is the point at which the rate of overageing (hardness decrease) is negligible (i.e. an asymptote on the ageing curve). A ratio to describe the nearly complete extent of overageing was developed as shown in Equation (1)

$$\text{Percent Overage} = \frac{H_{T6} - H_t}{H_{T6} - H_{T73}} \quad (1)$$

Where H_{T6} , H_t , and H_{T73} are the Rockwell hardness values at T6, at any time (t) between T6 and T73, and T73, respectively. T6 was defined as the base-line with a 0% overage condition. T73 was defined as the 100% overaged condition, while the T79 and T76 were defined as conditions that were overaged to 33% and 66% of the total drop in hardness from T6 to T73 tempers, respectively. The entire transient hardness data obtained from each alloy during ageing treatment is presented in the Appendix.

3.3.0 Corrosion Experiments

The corrosion experiments were carried out as modified EXCO and electrochemical experiments to study the propagation of corrosion and breakdown potential, respectively. The latter experiments also investigate the mechanism of corrosion initiation in the alloy samples.

3.3.1 Modified EXCO Experiment

Material for corrosion testing was cast from a permanent mould producing 3 unique planes: The longitudinal direction (L), transverse direction (T), and normal direction (N) were defined as the horizontal direction, vertical direction, and cross section, respectively seen in Figure 3.1 (b). The size of each plate casting was 20 cm × 10 cm × 0.635 cm (L x T x N). The LT plane was polished and exposed in all corrosion experiments. The cast plate was sectioned into four 10 cm × 5 cm (L x T) sections, three of which were used for the modified EXCO tests. The LT plane of three plates were manually ground flat using 800 grit SiC paper with water as the lubricant, followed by a chemical etch using 1.0 M NaOH_(aq) at 60°C for 90 s followed by immersion in 70 wt.% HNO_{3(aq)} at room temperature for 30 s to remove the active surface layer created during polishing [60]. Following etching, the polished surface was covered using masking tape and the five remaining sides were masked with RTV-5818 silicone (adhesive sealant). After 24 h of drying, the masking tape was removed, and acetone was used to remove residual adhesive. Finally, samples were immersed in 40°C isopropanol for 5 min, for ultrasonic cleaning.

Following the ASTM G34 standard practice [67] and a modification proposed by Lee and Liftka [68], a 750 mL solution of 600 mg/L Al³⁺_(aq), 4.0 M NaCl_(aq), and 0.6 M KNO_{3(aq)} was made. AlCl₃ was used to add Al³⁺ ions to the solution. Each sample was immersed in a separate solution for 96 h. Figure 3.3 shows an example layout of how the plate samples were immersed in the modified EXCO solution. Each plate was resting on the masked reverse side of the sample. Three samples of each alloy and temper were immersed to ensure repeatability. After 96 h of immersion in the modified EXCO solution,

Chapter 3: Experiments

samples were immersed in 70 wt.% $\text{HNO}_{3(\text{aq})}$ for 1 min to clean the surface of oxides. Photographs of the plate surfaces were taken prior to immersion in the modified EXCO solution and after each of 5 h, 24 h, 48 h, 72 h, and 96 h of immersion times in the modified EXCO solution, and again after the acid clean.

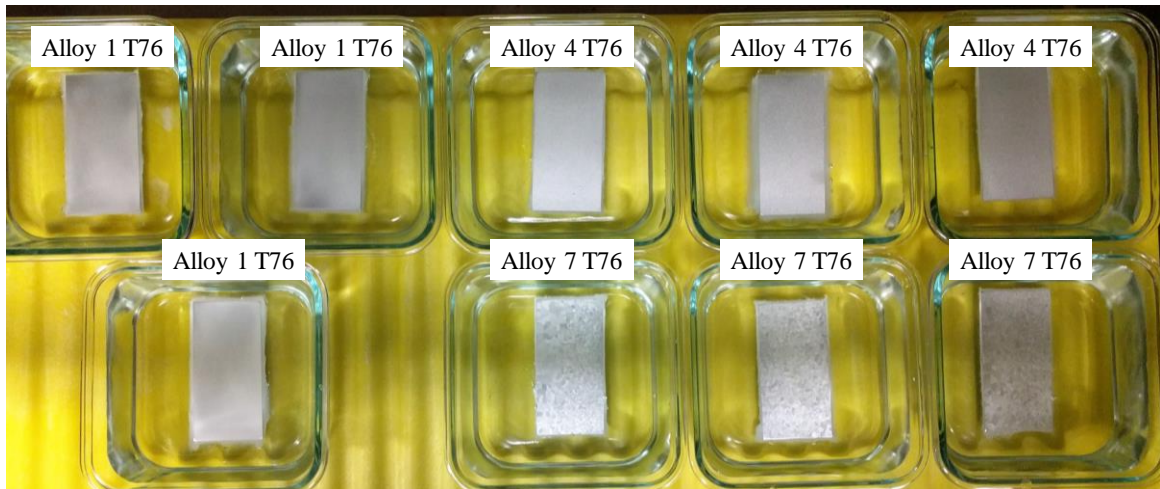


Figure 3.3: Layout of plate samples immersed in the modified EXCO solution. Three plate samples of alloy 1, 4, and 7 in the T76 temper are shown.

After the acid clean, plate samples were cross-sectioned near the top (5 mm from the top), middle, and bottom (5 mm from the bottom) along the longitudinal axis. This produced approximately 45 cm of cross-sectional length for each alloy and temper. These samples were cold mounted in epoxy and ground to 4000 grit surface finish using SiC abrasive paper and water as a lubricant, followed by polishing to a 1 μm surface finish using a diamond suspension and then a water free colloidal silica suspension (OPS). Using a Nikon Eclipse LV100 light optical microscope, each cross section was examined (and imaged) to locate the region of the deepest extent of corrosion attack: the depth of which being recorded.

3.3.2 Electrochemical Experiments

The remaining 5 cm × 10 cm plate section was cut into 1.5 cm square samples. Wires were connected to three samples then cold mounted in a 1.5 inch (38.1 mm) diameter epoxy resin mould exposing the LT plane. The working surfaces were manually ground to 4000 grit surface finish using SiC abrasive paper and water as a lubricant. Immediately following the grinding step, working surfaces were etched in 1.0 M NaOH_(aq) for 90 s at 60°C and then in 70 wt.% HNO_{3(aq)} for 30 s at room temperature to remove the deformed layer [60].

The prepared samples acted as working electrodes in a standard three-electrode corrosion cell configuration. A saturated calomel reference electrode (SCE) and two graphite counter electrodes acted as the other two electrodes. A VSP-300 Biologic potentiostat was used for all electrochemical measurements. Using a high purity nitrogen gas purge, a 900 mL 0.5 M NaCl_(aq) solution (prepared using reagent grade NaCl crystals and deionized water) was deaerated for at least 45 min prior to the immersion of the working electrode. Following deaeration, working electrodes were immersed in the solution and the open circuit potential (OCP) was recorded for 45 min. The working electrodes were then anodically polarized from the OCP to 200 mV above E_b at a scan rate of 0.2 mV/s. Three working electrodes of each alloy and temper were polarized to ensure repeatability.

To study initiation mechanisms, certain alloys and tempers of interest were chosen and potentiostatic polarization measurements were conducted. Working electrodes were

prepared in the same manner as for the potentiodynamic polarizations described above, except that the working surfaces were polished to 0.25 μm surface finish using a diamond suspension and then etched using the $\text{NaOH}_{(\text{aq})}$ and $\text{HNO}_{3(\text{aq})}$ procedure, as described above. A finer polish was used to reduce the defects on the surface for imaging. An extra set of potentiodynamic polarization measurement were carried out on the these working surfaces with the finer polish to ensure that the breakdown potential did not change. Working electrodes were polarized at 50 mV above the breakdown potential for 5 min to initiate corrosion. The working surfaces were rinsed in deionized water, followed by a rinse with ethanol, and finally dried using a stream of warm air. For each working electrode that was potentiostatically polarized, a second working electrode was left in the pristine condition, to serve as a baseline data. The working surfaces were examined using the SEM mode in the FIB-SEM dual platform.

3.4.0 Material Characterization

The metallographic characterization of the alloy microstructure was carried out using light optical, SEM and TEM.

3.4.1 Light Optical Microscopy

LT plane samples were mounted in cold epoxy resin moulds. A $\frac{1}{4}$ inch (6.4 mm) drill bit was used to expose the reverse side of the sample to facilitate preparation of a working electrode for subsequent etching. The working surfaces were ground and polished using the same procedure outlined above in the modified EXCO experiments. The as-

polished working surfaces were etched using Barker's reagent (in 5 ml $\text{HBF}_{4(\text{aq})}$ + 200 ml H_2O at 30 V dc) for 2 min. This was carried out by connecting the exposed reverse side of the as-polished surfaces to a power supply using a copper rod. After etching, the working surfaces were viewed under polarized light using a Nikon Eclipse LV100 light optical microscope at magnifications of 50x and 100x. The grain size was measured using an image analyses software and reported as Effective Circular Diameter (ECD). A subset of working surfaces were etched with Weck's reagent (100 ml H_2O , 4 g $\text{KMnO}_{4(\text{aq})}$, 1 g $\text{NaOH}_{(\text{aq})}$) for 6-16 s prior to being examined using the light optical microscopy (Nikon Eclipse LV100).

3.4.2 Electron Microscopy

A JOEL JSM-6610LV scanning electron microscope was used to characterize the working surfaces of both pristine samples and corroded samples after potentiostatic polarization. Images were obtained using a working distance of 10 mm at an energy of 10 kV. Various magnifications were used depending on size of the desired features. EDS line scans and spot analyses were quantified using the Aztec analysis software.

To investigate sub-surface corrosion initiation sites, a dual beam Zeiss NVision 40 dual beam platform equipped with X-ray energy-dispersive spectroscopy (EDS) was used to analyze the working surfaces of both pristine samples and corroded samples after potentiostatic polarization. INCA EDS X-ray micro-analysis was used to complete the analyses. A Ga^+ beam, ranging from 27 nA for fast removal of material to 300 pA for finer polishing of the cross section surface, was used to prepare cross-sections. Once polished

Chapter 3: Experiments

with the 300 pA beam, the cross-sectional surface was examined using secondary electron imaging (SEI), backscattered electron (BSE) imaging and EDS for elemental composition information.

The FIB-SEM was also used to prepare thin foils for TEM examination by milling out an area of interest (Figure 3.4), using a micro-manipulator to lift-out the foil, and tungsten deposition to attach it to a molybdenum grid. Tungsten was also used to protect the surface of the sample prior to milling.

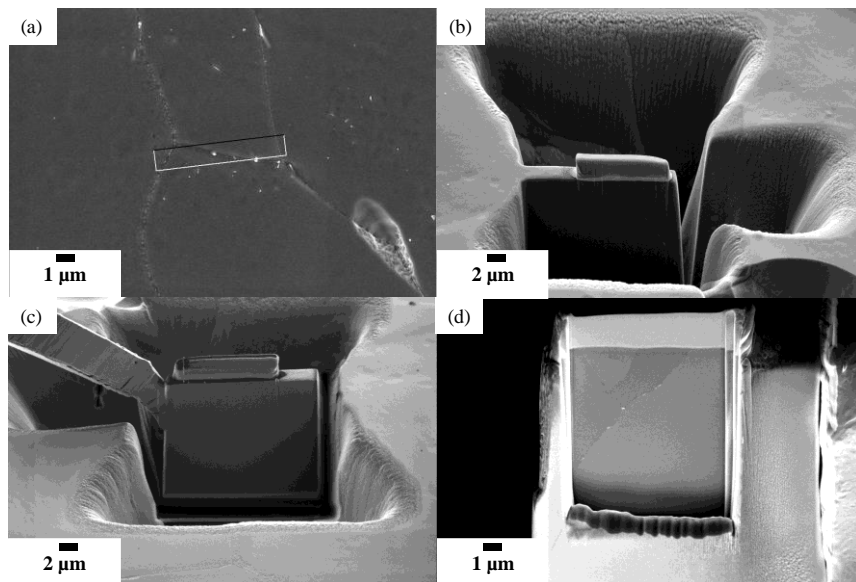


Figure 3.4: Sequence of TEM foil sample preparation in FIB-SEM (a) Sample location (b) Tungsten deposition and trenching (c) Micromanipulator attached to sample by tungsten deposition (d) sample attached to Mo grid and polished with Ga⁺ beam.

The foil was then further thinned to become electron transparent. Investigations were carried out using a JEOL 2010F TEM/STEM at an operating voltage of 200 kV. EDS line scans and point analysis was completed in STEM mode to perform compositional

Chapter 3: Experiments

investigations across microstructural features of interest (grain boundaries, PFZ, intermetallic particles, and precipitates).

Chapter 4: Results and Discussion

4.1.0 Microstructural Characterization

Solidification simulations were completed for each alloy using Pandat software under non-equilibrium (Scheil-Gulliver) conditions. Figure 4.1 shows the variation of the fraction of solid with temperature during solidification for each alloy. To obtain sound castings of near net shaped components, there needs to be a sufficient fraction of liquid prior to reaching the eutectic temperature (T_e) to fill in inherent volumetric shrinkages during solidification [69]. Low Cu alloys (1, 6, and 8) have the lowest liquid fraction values at T_e as defined by the length of the horizontal line in Figure 4.1. As a result, these alloys are very susceptible to hot cracking, but do not contain the large amounts of eutectic phases that increase localized corrosion susceptibility [3]. High Cu alloys (3, 5, 7, and validation) have higher liquid fraction values at T_e , but they contain a high fraction of eutectic phase that increase localized corrosion susceptibility.

Chapter 4: Results and Discussion

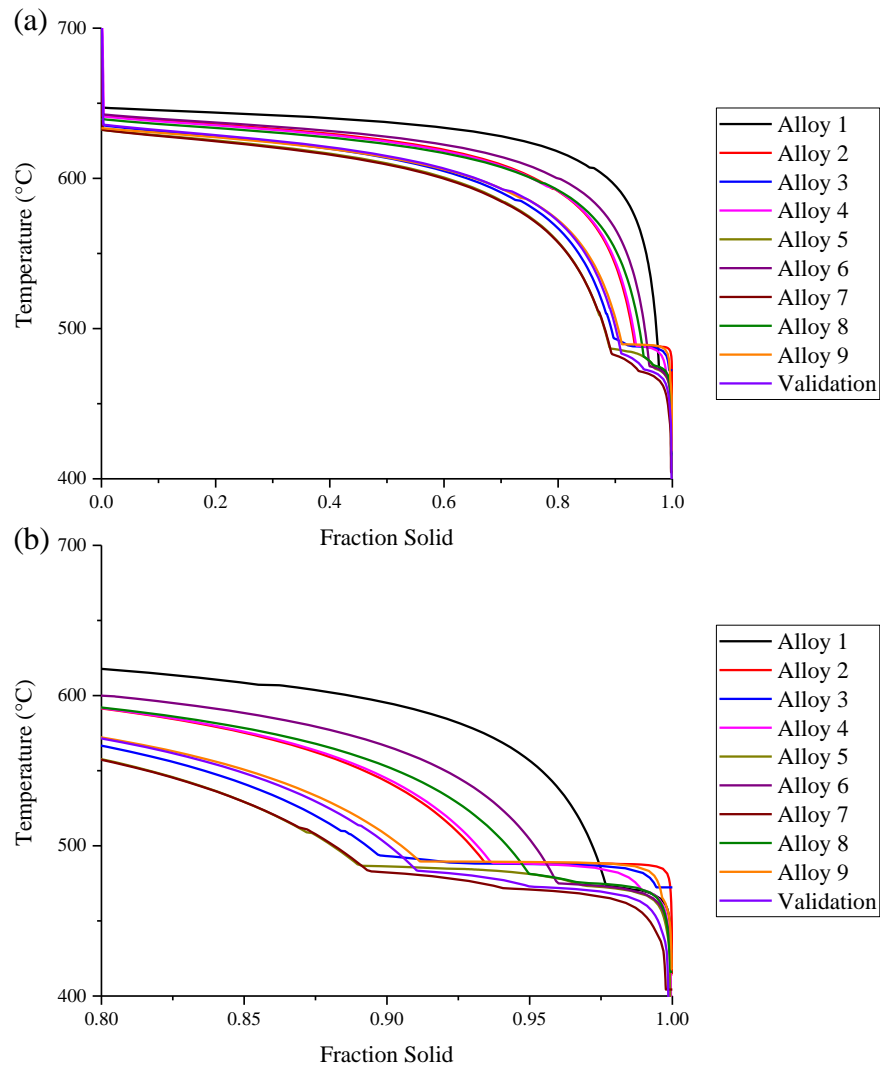


Figure 4.1: Solid fraction trace simulated under non-equilibrium conditions with Pandat software for (a) full solid fraction range (b) expanded solid fraction range approaching 1.0 (complete solidification).

A summary of predicted phases in each alloy in the as-cast condition is provided in Table 4.1. The Scheil-Gulliver model in Pandat tends to under-predict the total fraction of phases present in the as-cast condition because solidification conditions in the casting

Chapter 4: Results and Discussion

process deviates farther from the Scheil-Gulliver model towards increasing non-equilibrium conditions [2]. Moreover, all phases that are predicted to be present in the as-cast condition would be present in the T4 microstructure, except θ (Al_2Cu). It was assumed that each phase listed in Table 4.1 is present in each alloy after both natural ageing (T4 temper) and subsequent artificial ageing (T6 and T7x tempers), however, as it is a simulation, not all phases are represented in Table 4.1. For instance, it is expected that all alloys contain the Al_3Ti phase as each alloy contains dendritic imprints.

Table 4.1: Summary of possible phases present in the as-cast condition of each alloy as determined by the non-equilibrium simulation using Pandat software.

Alloy	Possible Phases
1	$\alpha\text{-Al}$, $\text{Al}_{13}\text{Fe}_4$, $\text{Mg}(\text{Zn,Cu,Al})_2$
2	$\alpha\text{-Al}$, $\text{Al}_{13}\text{Fe}_4$, $\text{Mg}(\text{Zn, Cu, Al})_2$, Al_3Ti , $\text{Al}_7\text{Cu}_2\text{Fe}$, $\text{S}(\text{Al}_2\text{MgCu})$
3	$\alpha\text{-Al}$, $\text{Al}_{13}\text{Fe}_4$, $\text{Mg}(\text{Zn, Cu, Al})_2$, Al_3Ti , $\text{Al}_7\text{Cu}_2\text{Fe}$, $\text{S}(\text{Al}_2\text{MgCu})$, $\theta(\text{Al}_2\text{Cu})$
4	$\alpha\text{-Al}$, $\text{Al}_{13}\text{Fe}_4$, $\text{Mg}(\text{Zn, Cu, Al})_2$, Al_3Ti , $\text{Al}_7\text{Cu}_2\text{Fe}$, $\theta(\text{Al}_2\text{Cu})$
5	$\alpha\text{-Al}$, $\text{Al}_{13}\text{Fe}_4$, $\text{Mg}(\text{Zn, Cu, Al})_2$, $\text{Al}_7\text{Cu}_2\text{Fe}$, $\text{S}(\text{Al}_2\text{MgCu})$, $\theta(\text{Al}_2\text{Cu})$
6	$\alpha\text{-Al}$, $\text{Al}_{13}\text{Fe}_4$, $\text{Mg}(\text{Zn, Cu, Al})_2$, Al_3Ti
7	$\alpha\text{-Al}$, $\text{Al}_{13}\text{Fe}_4$, $\text{Mg}(\text{Zn, Cu, Al})_2$, Al_3Ti , $\text{Al}_7\text{Cu}_2\text{Fe}$, $\theta(\text{Al}_2\text{Cu})$
8	$\alpha\text{-Al}$, $\text{Al}_{13}\text{Fe}_4$, $\text{Mg}(\text{Zn, Cu, Al})_2$, Al_3Ti
9	$\alpha\text{-Al}$, $\text{Al}_{13}\text{Fe}_4$, $\text{Mg}(\text{Zn, Cu, Al})_2$
Validation	$\alpha\text{-Al}$, $\text{Al}_{13}\text{Fe}_4$, $\text{Mg}(\text{Zn, Cu, Al})_2$, Al_3Ti , $\text{Al}_7\text{Cu}_2\text{Fe}$, $\theta(\text{Al}_2\text{Cu})$

A micrograph for each cast alloy at each temper is presented in the Appendix. The microstructure of all cast alloys show a non-dendritic morphology of the primary Al phase, as required for sound near net shaped casting. The amount of intermetallic phases observed in the microstructure can be linked to the fraction of liquid at T_e . Alloy 7, subjectively has the largest fraction of intermetallic phases in the microstructure and it has the highest liquid fraction (88%) at T_e . Alloy 1, 6, and 8 show the opposite as the visual inspection of the

micrographs shown in the Appendix reveal a higher percentage of shrinkage porosity in these alloys due to the low fraction of liquid at T_e .

Grain sizes are reported in the Appendix as Effective Circular Diameter (ECD). The grain size is highly dependant on the initial alloy composition, specifically the Ti content. Low Ti alloys such as 1, 5, 8, and 9, have large grains with a mean diameter (ECD) around 1 mm with a small fraction of small grains with a diameter of approximately 50 μm . Medium Ti alloys such as 2, 6, and 7, have higher fraction of small diameter grains with a mean of around 50 μm , with large grains covering a smaller fraction of the microstructure. High Ti alloys such as 3, 4, and validation, have a single uniform mean grain size of 50 μm in the alloy. Alloy 9 has a uniform grain size distribution with an average ECD of approximately 600 μm . Abnormal grain growth is evident in the low Ti-containing alloys, where the barrier to grain growth during SHT is minimal. Artificial ageing at 185°C does not present the sufficient required thermal energy for abnormal grain growth and, hence the grain structure retained after SHT remains unchanged during any ageing (natural or artificial) treatment. Although grain boundaries have shown to only contribute 3% to the overall yield strength of these Al alloys, a fine grain structure is important for other properties such as fracture toughness, surface finish, and fatigue crack growth rate [2–3,70].

Some of the microstructures in the Appendix show the imprints left behind by the growth of equiaxed dendrites during the initial stages of the alloy solidification; these imprints become visible under specific etching conditions that preferentially etch the interdendritic regions. As an example, Figure 4.2 shows alloy 8 in the T4 temper condition with

Chapter 4: Results and Discussion

abnormal grain growth and imprints of the equiaxed dendrites that formed in the initial stages of solidification. Notably, the morphology of the equiaxed dendrite imprints do not change during thermal treatment; SHT, natural ageing, or artificial ageing. The demarcation between the equiaxed dendrites and inter-dendritic region is merely compositional differences caused by a significant difference in solute re-distribution during dendritic growth at the early stages and growth of the inter-dendritic region after solute field impingement during the later stages of solidification. Consequently, a high angle grain boundary between these two regions does not form and, hence no abnormal growth of the equiaxed dendrites occurs. The dendritic imprints, visible from a contrast created by Barker's reagent during etching, occur as a consequence of the difference in growth mechanisms that occur during solidification of the dendrites and the subsequent inter-dendritic regions that evolve due to the Gibbs-Thompson curvature effect.

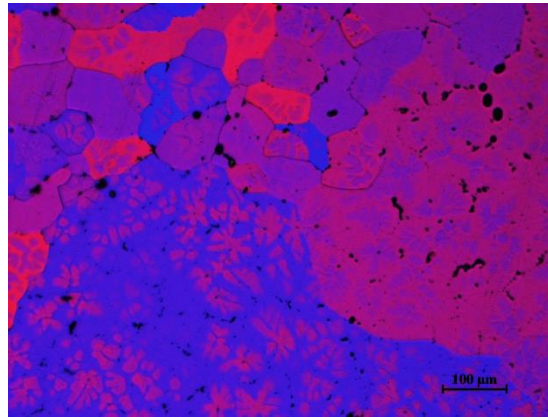


Figure 4.2: Light optical micrograph of alloy 8 after natural ageing (T4 temper) showing abnormal grain growth while retaining the morphology and size of the equiaxed dendrites from solidification.

Chapter 4: Results and Discussion

In these alloys, the Ti content in the bulk of the equiaxed dendrites is higher relative to the inter-dendritic region; as shown by the EDS results in Figure 4.3. Figure 4.3 shows the results of the qualitative EDS spot analyses acquired both within and adjacent to the equiaxed dendritic imprint (outlined area) in alloy 6 at the T6 temper and sampled after potentiostatic polarization at -884 mV for 5 min. Inside the dendritic imprint (EDS spots 1 and 4) a Ti peak is clearly visible, while, in regions outside the dendritic imprint (spots 2 and 3), no Ti peak is observed in the energy spectrum. SHT is not sufficient to homogenize the Ti segregation in the matrix resulting in the dendritic imprints, which may be due to the sluggish mobility of Ti in the Al matrix.

Chapter 4: Results and Discussion

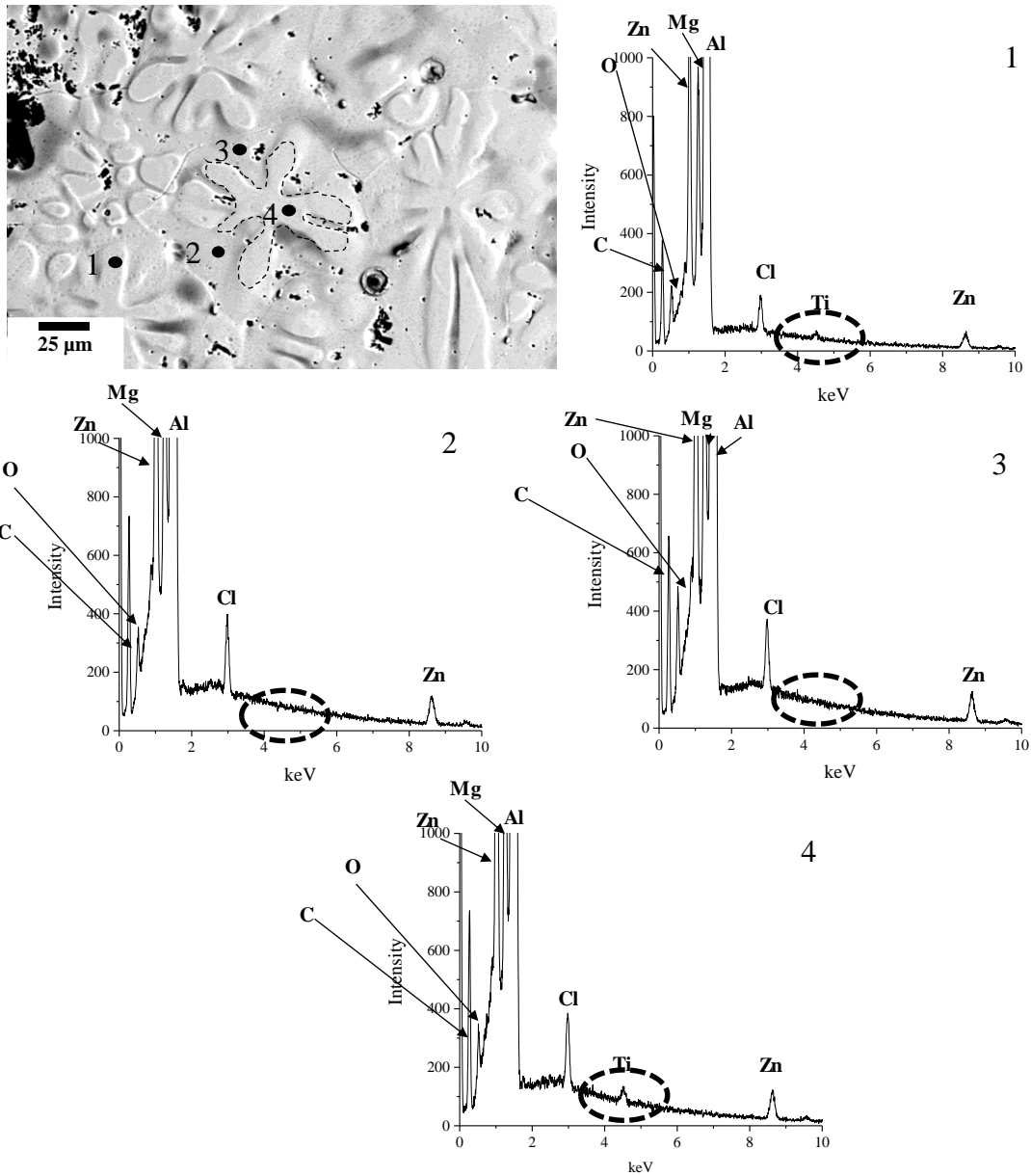


Figure 4.3: Typical qualitative EDS spot analyses taken within and adjacent to the equiaxed dendritic imprint to demonstrate the relative difference in Ti content (intensity) in these regions. Spectra taken on surface of alloy 6 at the T6 temper after potentiostatic polarization at $-884\text{ mV}_{\text{SCE}}$ for 5 min.

4.2.0 Potentiodynamic Polarization

The results of the potentiodynamic polarization experiments is presented in two parts: (i) evaluation of E_b along with the statistical analyses of the effect of the critical parameters on the variance of E_b and (ii) in-depth analysis of the peculiarities found in these experiment results for alloy 6 at the T6 temper.

4.2.1 Breakdown Potential, E_b

Potentiodynamic curves for all alloys with each temper can be found in the Appendix. Values of E_b obtained from each curve are presented in Table 4.2. Breakdown potential, E_b is a thermodynamic property and, therefore has no direct relationship with corrosion rates of the alloy [50]. However, the breakdown potential can provide mechanistic insight during corrosion initiation. All alloys (and tempers) exhibit one clear breakdown potential followed by a sharp increase in the anodic current density except for alloy 6 at the T6 temper. An in-depth discussion of the peculiarity observed with this alloy is presented in the next sub-section of this thesis.

Chapter 4: Results and Discussion

Table 4.2: Mean values of breakdown potential (E_b) observed in each alloy (and temper). Mean values are based on three repetitions of experiments conducted using a de-aerated 0.5M NaCl_(aq) solution at room temperature.

Alloy	T4 E_b (mV_{SCE})	T6 E_b (mV_{SCE})	T79 E_b (mV_{SCE})	T76 E_b (mV_{SCE})	T73 E_b (mV_{SCE})
Alloy 1	-942 ± 2	-862 ± 20	-861 ± 13	-860 ± 40	-838 ± 28
Alloy 2	-754 ± 17	-744 ± 9	-741 ± 13	-753 ± 5	-746 ± 12
Alloy 3	-735 ± 5	-733 ± 8	-746 ± 2	-754 ± 15	-751 ± 12
Alloy 4	-791 ± 16	-766 ± 15	-778 ± 19	-782 ± 26	-782 ± 10
Alloy 5	-736 ± 9	-747 ± 10	-741 ± 5	-749 ± 7	-750 ± 9
Alloy 6	-970 ± 7	-961 ± 8	-951 ± 14	-917 ± 5	-917 ± 8
Alloy 7	-742 ± 3	-754 ± 4	-769 ± 8	-789 ± 8	-782 ± 10
Alloy 8	-955 ± 10	-899 ± 6	-909 ± 30	-888 ± 4	-842 ± 12
Alloy 9	-827 ± 9	-740 ± 3	-749 ± 10	-757 ± 3	-755 ± 7
Alloy V	-732 ± 10	-706 ± 3	-754 ± 15	-770 ± 10	-764 ± 5

There have been a variety of studies that involved linking the breakdown/pitting potential to the bulk alloy composition and/or heat treatment in AA7xxx alloys [22,36,61,63,71–73], however, at comprehensive study of this scale (number of alloys and heat treatments) has not been completed. Figure 4.4 presents the plot of the main effects of the independent variables such as concentration of Zn, Mg, Cu and Ti in addition to the weight ratio of the Zn to Cu concentration in weight percent. These plots show that the individual effect of concentrations of Zn, Mg and Ti are random on the mean value of E_b , while the concentration of Cu and the Zn/Cu ratio have pronounced influence on the E_b .

Chapter 4: Results and Discussion

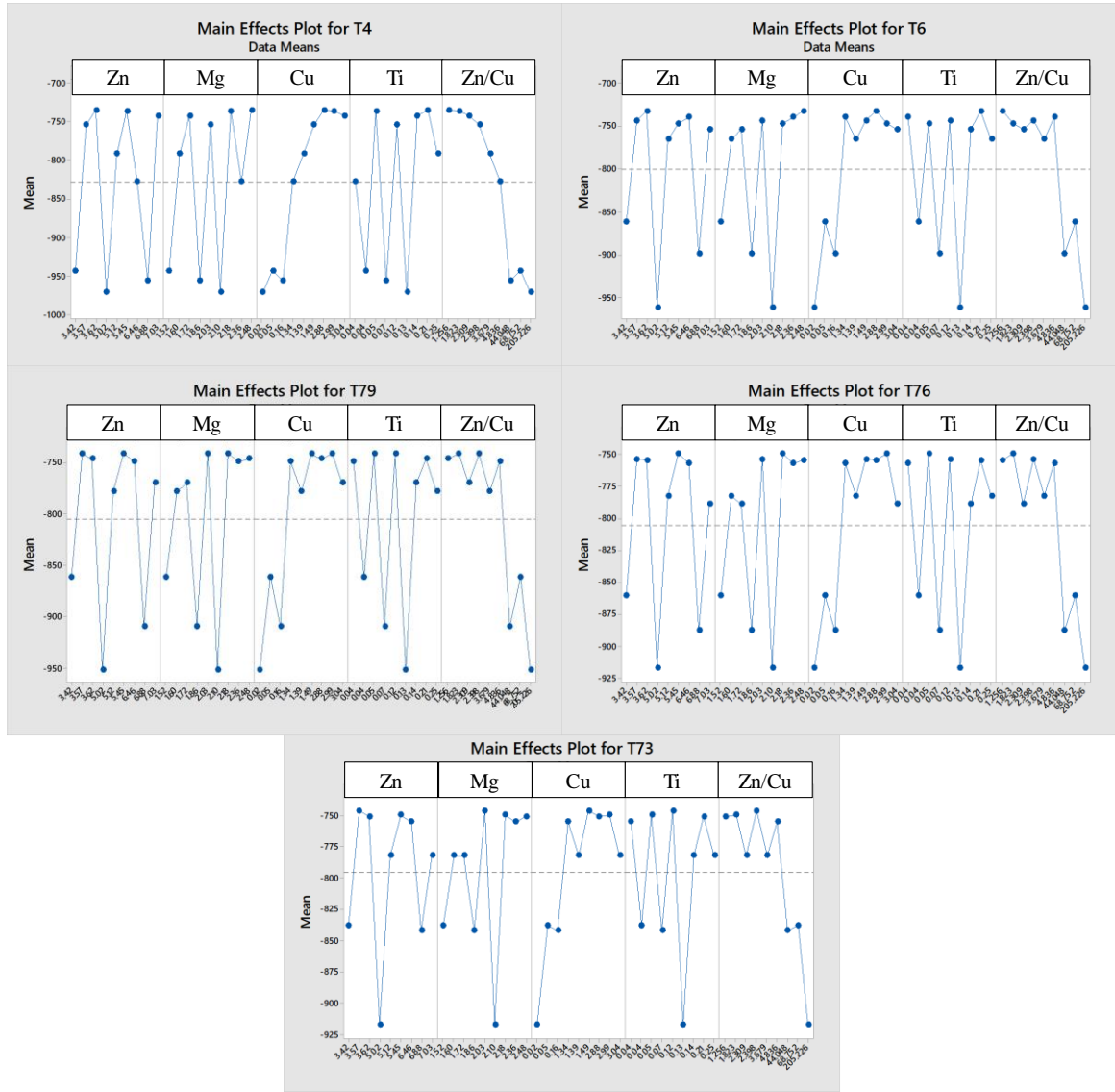


Figure 4.4: The plots of main effects of the independent parameters (wt.%) on the dependant variable, E_b .

Figure 4.5 presents the values of breakdown potential, E_b for the various tempers of the alloys in the study; it is quite evident that adding Cu to the alloys increases E_b and further, all Cu-containing alloys (medium or high levels) removes the variability in E_b as a function of either alloy composition or temper. Notably, in Figure 4.5, the Cu-free alloys show an increase in E_b between the T4 and T73 tempers; this trend is lost when Cu is added

Chapter 4: Results and Discussion

to these alloys. However, one Cu-containing alloy, alloy 9, shows a peculiar behaviour of a significant increase in E_b between the T4 and T6 tempers (orange line in Figure 4.5). This is an anomaly, along with the increasing E_b in Cu-free alloys with artificial ageing, cannot be explained by just considering the Cu content of the alloys.

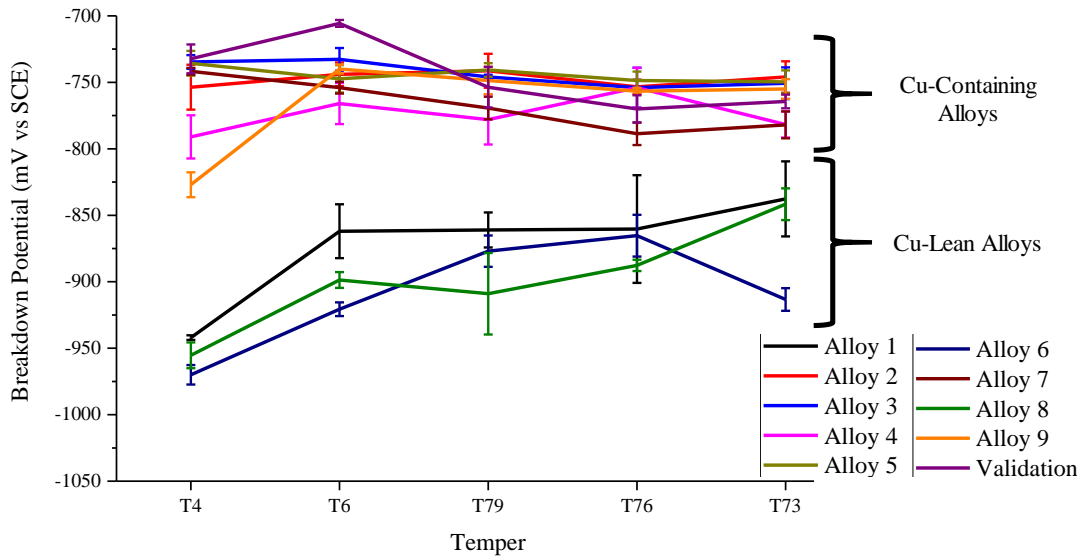


Figure 4.5: Plot of E_b with respect to temper of the samples.

Another parameter that plays a critical role in affecting the E_b is the weight ratio of Zn to Cu in the alloys. Meng et al. [73] discovered that the breakdown potential and Cu content showed a semi-logarithmic relationship [73]. However, Wang et al. [61] showed that there is competing phenomena between Zn depletion and Cu depletion from the solid solution of the Al matrix: Zn depletion leads to an increase in E_b , while Cu depletion leads to a decrease of the same. If the Cu content solely influences the value of E_b , then the alloys with no Cu content should not show any trend in variation of E_b with changes in temper for

Chapter 4: Results and Discussion

a specific alloy composition. However, Figure 4.5 clearly shows that there is an increasing trend of the value of E_b as the temper changes from T4 to T73, which leads to the assumption that there is more than merely the Cu content that affects E_b with changes in temper. Wang et al. [61] attributed the trend in Cu-free alloys to the continued Zn depletion in the matrix with ageing. In the reported literature, the breakdown potentials of Cu-containing alloys increases from the T4 to the T6 temper, then decreases with artificial ageing to the T73; also, Cu-free alloys show a continual increase in E_b from the T4 to the T73 temper [36]. Wang et al. [61] argued that Zn depletion dominates in the early stages of artificial ageing to raise the breakdown potential, while Cu depletion from the solid solution Al matrix and subsequent incorporation into the strengthening precipitates controls the breakdown potential at the later stages of artificial ageing. The results shown in Figure 4.5 do not show any appreciable trend in the variation of E_b in Cu-containing alloys except the initial increase for alloy 9 between the T4 and T6 tempers.

Taking the works of Meng et al. [73] and Wang et al. [61] into consideration, a model is proposed to correlate the trend in changes of E_b to the weight of Zn to Cu in the alloys. The model is a semi-logarithmic relationship as shown by the general expression in Equation (2), wherein the concentrations of Zn and Cu are in weight fractions, and A and B are constants of the linear regression model. Equation (2) is valid for a range of 1 to 205 for the weight ratio of Zn to Cu, 1.5 to 2.5 wt.% Mg, and 0.04 to 0.25 wt.% Ti.

$$E_b = A \cdot \log\left(\frac{Zn}{Cu}\right) + B \quad (2)$$

Chapter 4: Results and Discussion

Table 4.3: Values of the constants A and B in Equation (2) along with the R^2 value of the linear regression model and % difference between experimental and predicted E_b in the validation alloy.

Temper	A (mV_{SCE})	B (mV_{SCE})	R²	Percent Difference Between Experimental and Predicted Validation Alloy
T4	-122	-717.5	0.95	3.4
T6	-101	-709.5	0.93	5
T79	-96	-718.2	0.92	0.5
T76	-77	-735.3	0.92	1.2
T73	-69	-733.5	0.90	1

A graphical representation of the data presented in Table 4.3 is shown in Figure 4.6. The model was generated using alloys 1-9, then validated by comparing the experimental E_b obtained for the validation alloy with the one predicted by the linear regression model for compositions matching that of the validation alloy. All five models show a percent error less than 5% from the predicted value of E_b to the mean experimental value obtained during the experiments. A percent error less than or equal to 5% is evidence of a statistical model with good fit.

Chapter 4: Results and Discussion

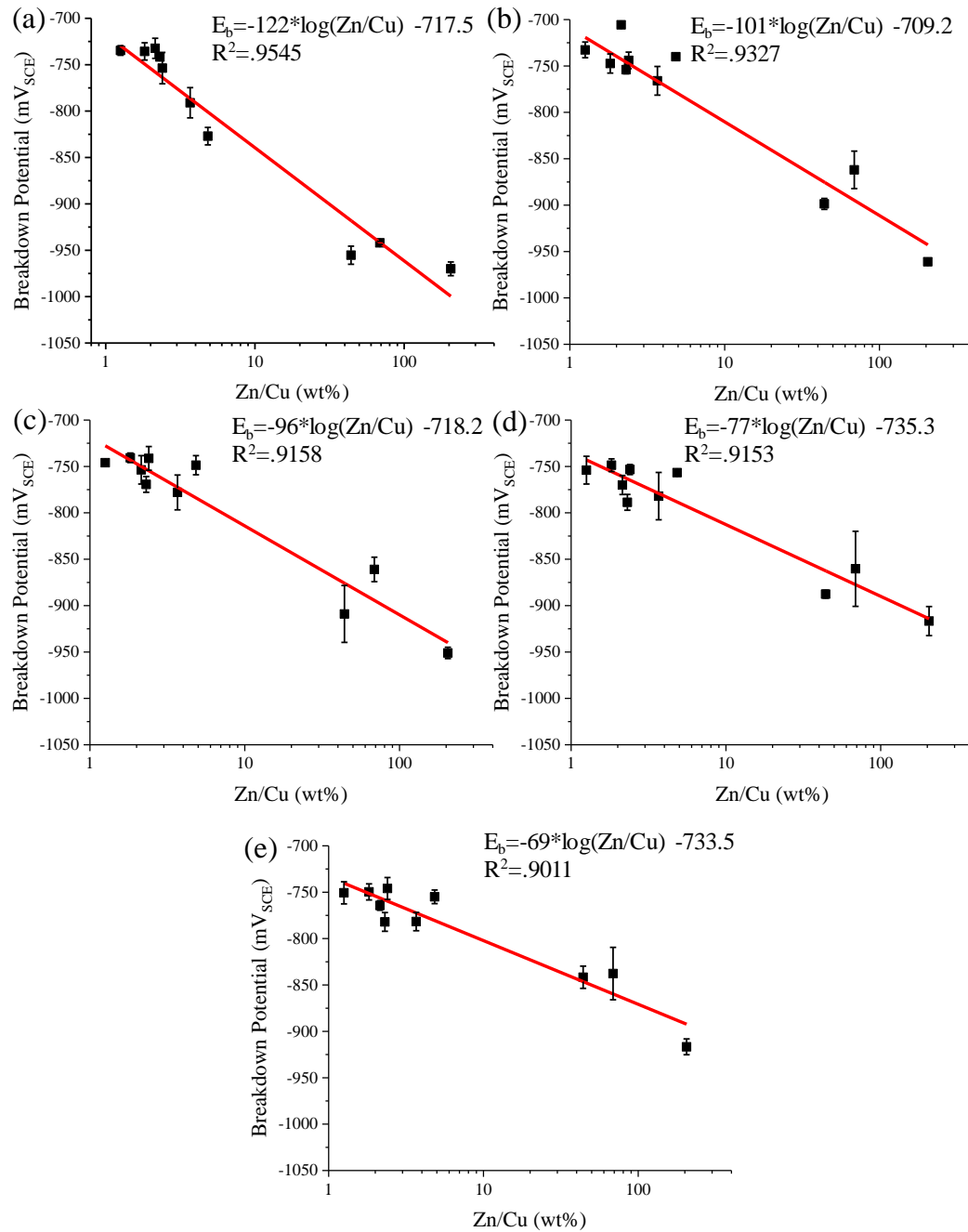


Figure 4.6: Graphical representation of the linear regression model correlating E_b to the weight ratio of Zn to Cu in the alloys (a) T4 (b) T6 (c) T79 (d) T76 (e) T73.

Chapter 4: Results and Discussion

Various values of the weight ratio of Zn to Cu, which were representative of the ten alloys in this study, that were used in Equation (2) is presented in Figure 4.7. The use of Zn to Cu ratio over merely the Cu content in the alloy presents better clarity on the trends of the changes in the values of E_b as the ageing (natural and artificial) ageing time increases from T4 to T73 conditions.

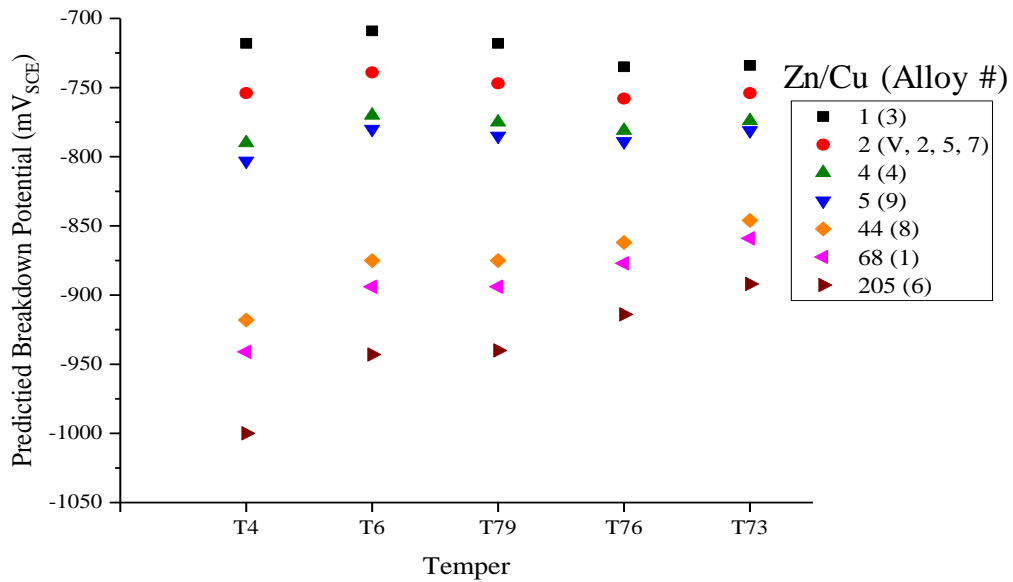


Figure 4.7. Graphical plot of E_b and the weight ratio of Zn to Cu that is representative of the ten alloys in this study.

Figure 4.7 show that in Cu-free alloys, with Zn to Cu ratio values of greater than 44, exhibit a continually increasing trend in the values of E_b , while Cu-containing alloys with values of Zn to Cu less than 4 show a marginal initial increase in mean value of E_b from the T4 to the T6 temper, followed by a marginal decrease of the same from the T6 temper to the T73 temper. Notably, the trend in E_b with temper for Zn to Cu weight ratios

Chapter 4: Results and Discussion

less than 4 is marginal: it stands to reason that the E_b trends observed in literature in Cu-containing alloys [36] and the lack of trends observed in the experimental results of this thesis could be within experimental error. Alloys containing an initial Zn to Cu weight ratio of 5 (alloy 9) shows that there exists an initial increase in the mean value of E_b from the T4 temper to the T6 temper, followed by no significant change from the T6 temper to the T73 temper. The trends of E_b shown in Figure 4.7 has also been reported by in literature [36]. It is notable that considering only Cu content in the alloy as the influencing parameter for changes in E_b is not as valid as considering the weight ratio of Zn to Cu in the AA7xxx alloys (Figure 4.7).

Mg is shown not to contribute to the breakdown potential (Figure 4.4). The strengthening precipitates of AA7xxx alloys are commonly believed to be $Mg(Al,Zn,Cu)_2$ precipitates, wherein the Mg content is rigidly defined by the stoichiometry (33 at%) and the Zn content is variable depending on how many of the Zn atoms in the lattice are substituted by Al and/or Cu atoms [24]. It is possible that given that the Mg content of all the AA7xxx alloys in this study is well below the maximum solubility limit in the Al matrix, it is safe to assume that all the Mg atoms gradually migrate from the solid solution matrix to the strengthening precipitates because of the excess amounts of Zn, Cu and Al in the matrix regardless of alloy composition. If true, then the Mg content in these alloys do not play a critical role in influencing the trends in the changes of E_b .

4.2.2 Potentiodynamic Polarization of Alloy 6

Alloy 6 (Al-5Zn-2Mg-0.13Ti) in the T6 and T7x tempers exhibit multiple active regions in the anodic potentiodynamic polarization curve, as shown in Figure 4.8. The T4 temper exhibits a single breakdown, which is expected and is comparable to all other alloys. In contrast, the T6 and T79 temper show an initial active region at -1000 mV_{SCE}, followed by a repassivation region until a typical breakdown event occurs at approximately -955 mV_{SCE}. The T76 and T73 tempers show an initial breakdown event at -917 mV_{SCE}, followed by a small passive region and then a second breakdown event occurs at -860 mV_{SCE}.

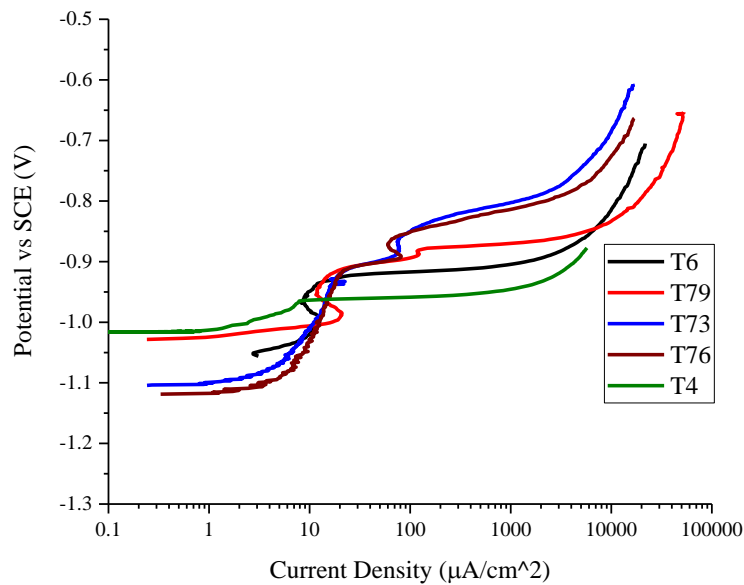


Figure 4.8: Potentiodynamic anodic polarization curves of alloy 6 in deaerated 0.5 M NaCl_(aq) solution.

Chapter 4: Results and Discussion

In the reported literature [71], alloys that have multiple active regions (double breakdown events) have a Zn-rich layer on the sample surface that preferentially dissolves creating the first breakdown event. The second breakdown event is then the breakdown of the underlying matrix [71]. All alloys in this study have been chemically etched to remove the deformation-induced Zn-rich surface layer produced during sample preparation. Cu-free alloys have an active layer due to the polishing during sample preparation before etching, but do not show a double breakdown [61]. An increase in anodic current density has been noted in the Al-Fe system, where cathodic polarization prior to potentiodynamic polarization causes Al in Al₃Fe phases to selectively dissolve. The remaining Fe is then passivated during continued anodic polarization causing an active-passive region [46]. The existence of two active regions in alloy 6 required further analysis.

Table 4.4: Summary of active potentials in alloy 6.

Temper	1st Active State (mV_{SCE})	2nd Active State (mV_{SCE})
T4	-970 ± 4	N/A
T6	-1000 ± 4	-961 ± 4
T79	-1000 ± 9	-951 ± 9
T76	-917 ± 4	-864 ± 4
T73	-917 ± 5	-861 ± 5

The T6 temper of alloy 6 was investigated further using dual platform FIB-SEM. For comparative purposes, the pristine sample of alloy 6 at the T6 temper was also examined. Figure 4.9 shows a secondary electron image of the pristine surface. The equiaxed dendritic imprints and grain boundaries are clearly apparent. This sample has no modes of corrosion visible on the surface.

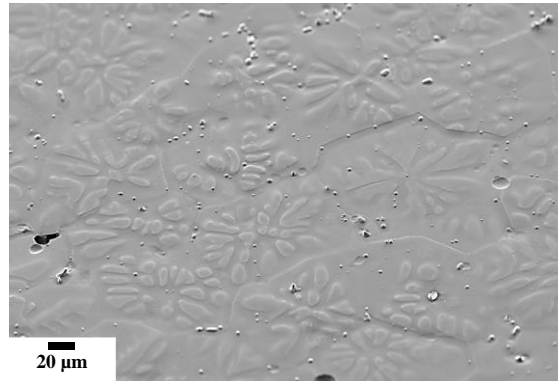


Figure 4.9: Secondary electron image of the pristine (as-etched) surface of alloy 6 at the T6 temper clearly showing the dendritic imprints and grain boundaries.

One sample was anodically polarized at $+50 \text{ mV}_{\text{SCE}}$ above the matrix E_b ($-884 \text{ mV}_{\text{SCE}}$) and a second sample was anodically polarized within the initial active state ($-1040 \text{ mV}_{\text{SCE}}$), for a 5 min duration each. Figure 4.10 shows a set of secondary electron images of the surface anodically polarized at $-884 \text{ mV}_{\text{SCE}}$ for 5 min. The potentiodynamic polarization curves is shown in Figure 4.10a and a typical current transient recorded during the 5 min potentiostatic polarization is shown in b of the same. There are two modes of corrosion observed on the surface of this Cu-free alloy. The first mode is denoted as interdendritic corrosion (IDC) and the second mode is a mix between corrosion rings and domes. As is shown by the modified EXCO results, later in this thesis, all alloys are susceptible to IDC. This is the phenomenon where corrosion is localized to the interdendritic regions leaving the dendritic imprint intact. Figure 4.10c and d clearly show that the corrosion is localized to the interdendritic region. As was shown in Figure 4.3, the dendritic imprints are rich in Ti. The retention of the Ti segregation between the equiaxed dendritic and the interdendritic regions results in a barrier to corrosion propagation into the

Chapter 4: Results and Discussion

equiaxed dendritic regions. However, the mechanisms involved in the role of Ti in affecting the propagation of corrosion needs to be further investigated. A plausible hypothesis involves Ti, being more noble than the other alloying elements, prevents propagation of corrosion into the dendritic regions.

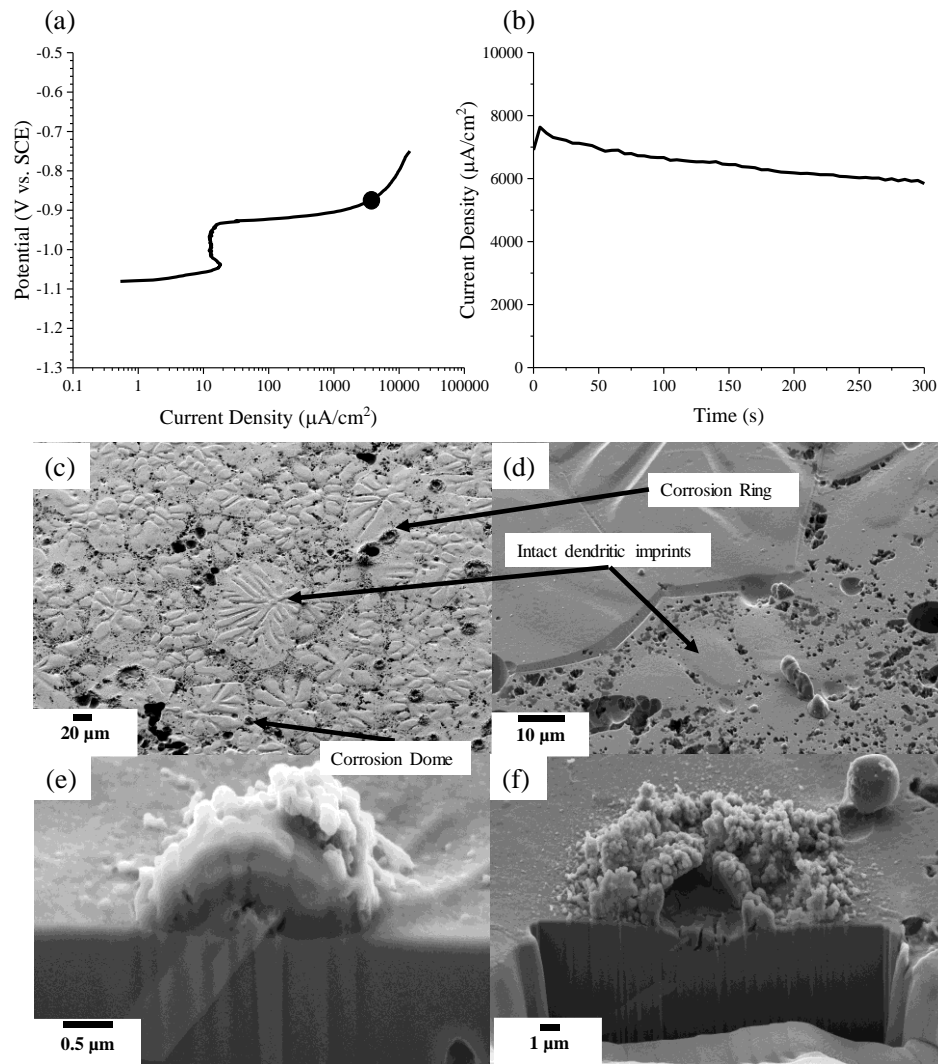


Figure 4.10: Results of the potentiostatic polarization experiment of alloy 6 at the T6 temper corresponding to matrix breakdown (-884 mV_{SCE} in deaerated 0.5 M NaCl_(aq)) (a) potentiodynamic (b) current density transient during 5 min potentiostatic (c-d) secondary electron image of the surface (e) secondary electron image of a FIB-prepared cross-section of a corrosion dome with intermetallic particle at base (f) secondary electron image of a FIB-prepared corrosion-section of a co-operative corrosion ring.

Chapter 4: Results and Discussion

The second corrosion mode observed when anodically polarized above the matrix breakdown potential is co-operative corrosion leading to corrosion rings and domes. Typical rings and domes are identified in Figure 4.10c-f. Corrosion rings are thought to be indicative of initiation sites for stable pitting and form over areas that have multiple intermetallic present (co-operative corrosion) [39]. After using the FIB to mill through the dome, an intermetallic particle was found at the base of the dome. An EDS spot analysis of this intermetallic particle revealed that it is rich in Fe (Figure 4.11). Based on the results of the Pandat solidification simulation (Table 1) and the morphology of the phase in the microstructure, the phase is most likely $\text{Al}_{13}\text{Fe}_4$. FIB milling of several corrosion domes revealed that the presumed $\text{Al}_{13}\text{Fe}_4$ phase is present at the base of all of them. As a stable phase, the presumed $\text{Al}_{13}\text{Fe}_4$ particles likely evolves during solidification of these alloys and remains in the microstructure through all subsequent heat treatment of the samples. Additionally, it is notable that the solidification simulation (Scheil-Gulliver non-equilibrium paradigm) suggests that these $\text{Al}_{13}\text{Fe}_4$ phases typically form at the later stages of solidification, particularly after the arrest of the growing equiaxed dendrites from solute field impingement. Hence, these Fe-rich phase particles exist in the inter-dendritic regions of the primary Al grains after solidification. Figure 4.10f shows the cross section of a typical corrosion ring, where, under the surface, there is a blocky particle (presumed $\text{Al}_{13}\text{Fe}_4$) and a few fine particles closer to the surface. The interior regions of the ring likely serve as local cathodes facilitating initiation of stable pitting.

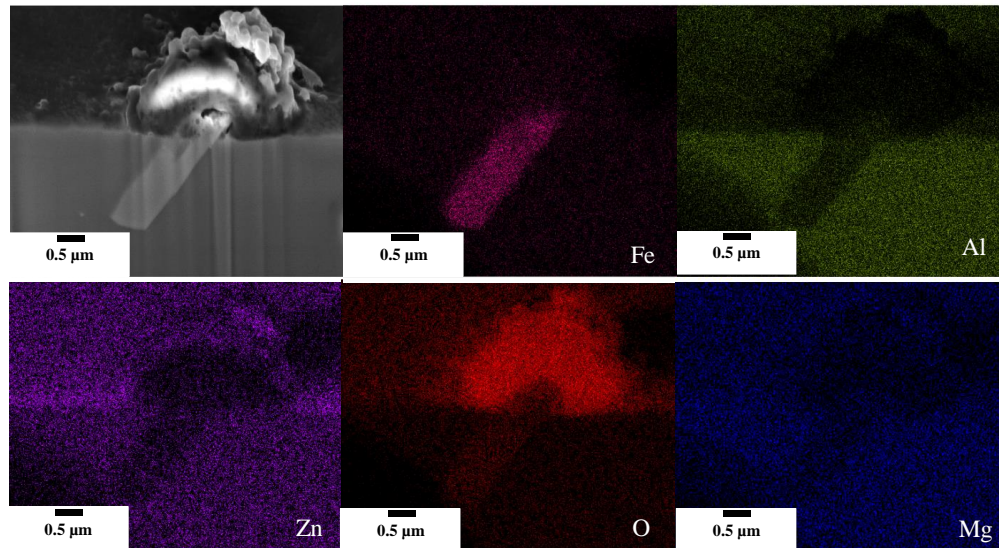


Figure 4.11: EDS elemental maps of the corrosion dome observed in FIB-prepared cross-section of alloy 6 at the T6 temper shown in Figure 10e.

Figure 4.12 shows the results of the potentiostatic polarization experiment involving the initial active state ($-1040 \text{ mV}_{\text{SCE}}$) of alloy 6 at the T6 temper polarized at $-884 \text{ mV}_{\text{SCE}}$ for 5 min. Figure 4.12c shows a secondary electron image of the surface after potentiostatic polarization for 5 min. Figure 4.12b shows the current transient stabilizing at a significantly lower value ($\cong 2 \mu\text{A}/\text{cm}^2$) than the current transient in Figure 4.10 ($\cong 6000 \mu\text{A}/\text{cm}^2$) indicating that less corrosion has occurred in the sample polarized at $-1040 \text{ mV}_{\text{SCE}}$. There is a distinct difference in appearance between the surface polarized within the 1st active state relative to the surface polarized above the breakdown of the matrix. The surface at the 1st active state is free of IDC: the only mode of corrosion observed is the corrosion domes. A presumably $\text{Al}_{13}\text{Fe}_4$ intermetallic particle was found at the base of the dome, as shown in Figure 12 (b) and the set of EDS spectra shown in Figure 12 (e). It is conjectured that the intermetallic particle is responsible for the initiation of the corrosion

Chapter 4: Results and Discussion

dome formation. The fact that no large corrosion rings are observed whilst polarized into the 1st active state indicates that the 1st active-passive transition is likely due to the repassivation of the presumed $\text{Al}_{13}\text{Fe}_4$ phase. The striking similarity between the corrosion domes and the nature of the initiation site found in this study and that reported by Seri et al. [45] for Al-Fe alloys leads to the conjecture that the etching procedure to remove the active surface layer applied in this work is similar to the cathodic pre-treatment applied by Seri et al [45]. Instead of a cathodic pre-treatment prior to polarizing, the alkaline etching process dealloys the Al in the Fe-based intermetallic phase allowing the repassivation of Fe to occur. The absence of corrosion rings (evidence of co-operative corrosion) in the sample polarized at $-1040 \text{ mV}_{\text{SCE}}$ shows that the stable pitting does not occur in this active region.

In the T6 and T79 tempers, the 1st active state is caused by $\text{Al}_{13}\text{Fe}_4$ intermetallic particle corrosion followed by repassivation of the dealloyed Fe. Subsequently, the surface becomes stable until the breakdown of the matrix initiates (possibly due to co-operative corrosion) and propagates via IDC. The T4 temper does not show this 1st active region because the OCP (corrosion potential) is pinned at same potential value as the 1st active region for the T6 and T79 tempers. The E_b of T4 matches closely with the E_b of the T6 and T79 tempers. The T76 and T73 tempers do not show a repassivation similar to the T6 and T79 tempers, but these tempers still exhibit two breakdown potentials. The presumed $\text{Al}_{13}\text{Fe}_4$ intermetallic particles do not disappear during artificial ageing, so it is unclear at this point why the potentiodynamic curve changes significantly during artificial ageing. It is possible that the effect of Cu desensitizes the alloy to this effect, but if this is the case,

Chapter 4: Results and Discussion

then all Cu-free alloys (1, 6, and 8) should still exhibit two active regions. More research is required at each temper in each Cu-free alloy to understand the mechanism.

In summary, the analyses of the results from the potentiodynamic polarization experiments reveal that the propensity for corrosion initiation is higher in Cu-free alloys due to the lower values of E_b in these alloys. Specifically, the decreasing weight ratio of Zn to Cu values in the alloy results in decreasing propensity for corrosion initiation. The propensity of corrosion propagation is further investigated using the modified EXCO experiment.

Chapter 4: Results and Discussion

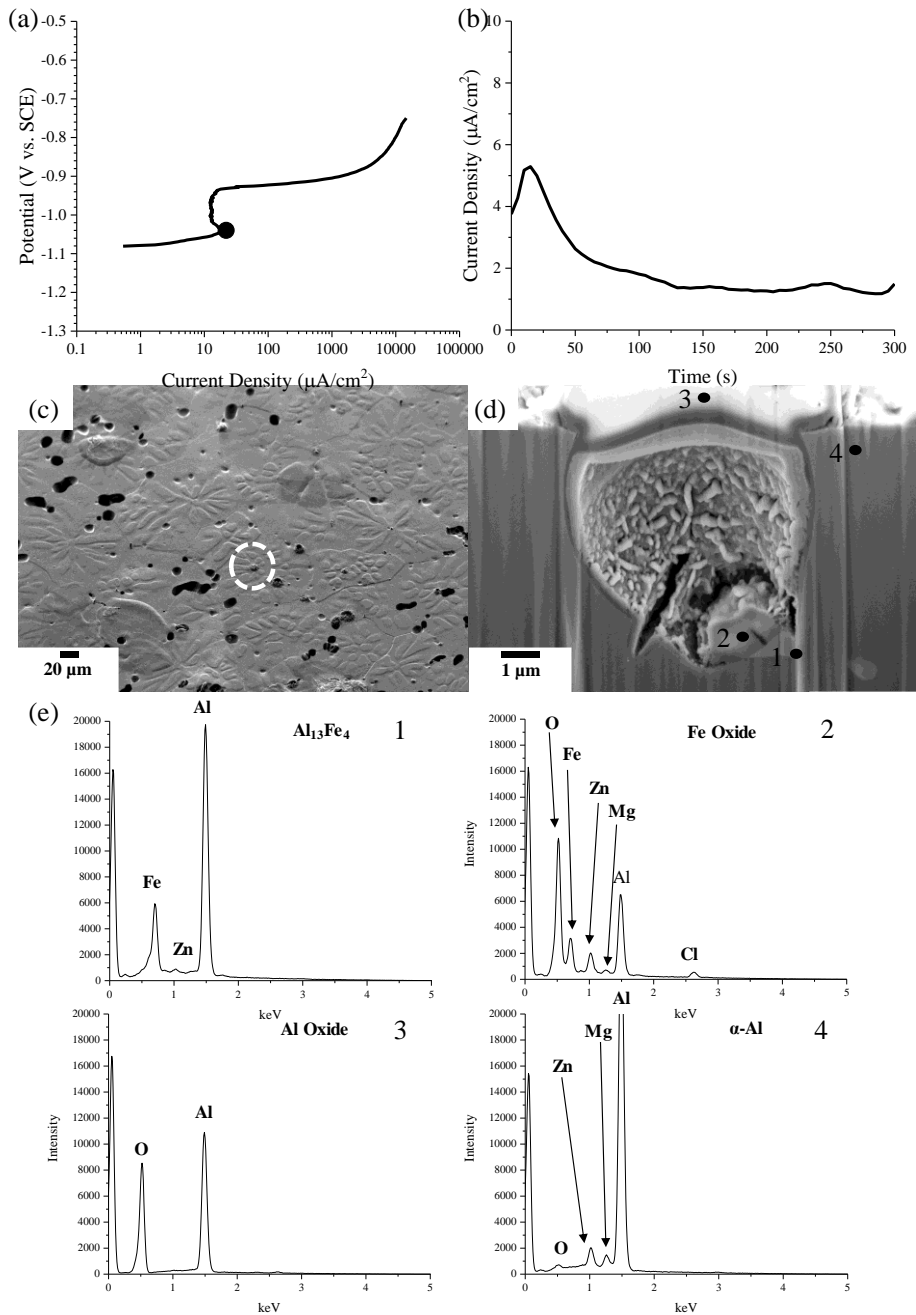


Figure 4.12: Results of the potentiostatic polarization experiment of alloy 6 at the T6 temper corresponding to the 1st active state region ($-1040 \text{ mV}_{\text{SCE}}$) in deaerated $0.5 \text{ M NaCl}_{(\text{aq})}$: (a) potentiodynamic curve (b) current density transient (c) secondary electron image of surface (d) secondary electron image of FIB-prepared cross-section through a corrosion dome (e) EDS spot analyses corrosion dome and underlying intermetallic particle corresponding to the spots identified in (d).

4.3.0 Modified EXCO Experiments

Photographs of the cast plate surfaces, taken before and after the modified EXCO experiments, along with light optical microscopy cross-sectional images of the corroded surfaces, are presented in the Appendix, within the respective section for each alloy. The maximum depth of attack was recorded for each plate immersed in the modified EXCO solution and the values are also tabulated for each alloy in the Appendix. The breakdown potential, E_b was used as a metric to help understand the mode of corrosion initiation. The modified EXCO experiments were used to study relative changes localized corrosion susceptibility in terms of the mode and extent of corrosion observed after 96 h of immersion. Table 4.5 summarizes the mode of corrosion and depth of attack observed after 96 h of immersion in the EXCO solution. There is also a strong correlation between the extent of attack and the Cu content in the alloy. The plate images in the Appendix show that the Cu-lean alloys (alloys 1, 6, and 8) have very little surface damage compared to all other Cu-containing alloys. The Cu-free alloys do not have the detrimental Cu-rich intermetallic particles that promote the formation of microgalvanic cells. In contrast, Cu-containing alloys contain a relatively high volume fraction of detrimental Cu-rich intermetallic particles that promote the formation of microgalvanic cells. Even an alloy containing a relatively small amount of Cu, such as in alloy 9 (Al-6.5Zn-2.4Mg-1.3Cu-0.04Ti), the surface damage and maximum depth of attack is similar to alloys that contain 3 wt.% Cu (alloys 5 and 7).

Corrosion on the surface of the plates and cross-section maximum depth of attack after 96 h immersion in the modified EXCO experiments show that in Cu-free alloys, such

Chapter 4: Results and Discussion

as alloys 1,6, and 8, the T4 temper samples exhibit more corrosion than those with the T6 and T7x ageing treatments. Cu-free alloys in the T4 temper condition have more Zn in the matrix solid solution than the samples in the T6 and T7x tempers due to the formation of strengthening precipitates upon artificial ageing. Decreasing the amount of Zn in the matrix solid solution reduces the galvanic potential difference between the Fe-containing phases and matrix, reducing the driving force for corrosion. Cu-containing alloys do not show a significant difference in corrosion susceptibility between the T4 temper condition and the aged conditions in the T6 and T7x tempers, because, the matrix solid solution contains Cu which reduces the galvanic interaction between strengthening precipitates and matrix. Another salient observation to support these corrosion tendencies as a function of alloy composition would be the trend in the changes of E_b , as discussed in the previous section. In Cu-lean alloys such as alloys 1, 6 and 8, the value of E_b is significantly less for the T4 temper when compared to the subsequent T6 and T7x tempers after ageing; while, in the Cu-containing alloys, the value of E_b does not show a significant difference between the T4 and the aged, T6 and T7x tempers. This observation corroborates the results obtained from the modified EXCO experiments, as explained above, in this section. Hence, it would lead to safely suggest that within a given alloy composition, the increasing values of E_b lead to decreasing corrosion tendencies.

Figure 4.13 presents a set of cross-sectional light optical microscopy images of the corroded surface in cross-section. The alloys are arranged such that there is increasing Cu content from left to right of the image and increasing Ti content from top to bottom. It is evident from Figure 4.13a-c that, for a nearly constant Ti content in the alloy (<0.05 wt%),

Chapter 4: Results and Discussion

an increase in the Cu content increases corrosion attack, as shown by the increasing maximum depth of attack. Notably, the typical mode of corrosion in the samples of alloys 9 and 5 in Figure 4.13a-c is IDC, which is evident from the equiaxed dendritic morphology that is intact after corrosion. It is shown that all alloys displaying IDC as the primary mechanism of attack have similar maximum depth of penetration, regardless of the damage to the exposed surface, as shown in Figure 4.13 and quantified in the Appendix and Table 4.5: IDC is a form of selective dissolution of the interdendritic regions. All the nine alloys shown in Figure 4.13, have a sufficient Ti content to result in a very similar mechanism of athermal nucleation and unconstrained growth leading to a similar size and morphology of equiaxed dendrites during the initial stages of solidification of the primary Al matrix. Hence, all the alloys show propensity to IDC. However, the addition of Cu to these alloys increases the extent of this corrosion in the modified EXCO experiments. Corrosion in Cu-free alloys (1, 6, and 8) propagates by IDC after initiation, as shown by alloy 6 in Figure 4.10, however the extent of the damage is minimal in the modified EXCO experiment.

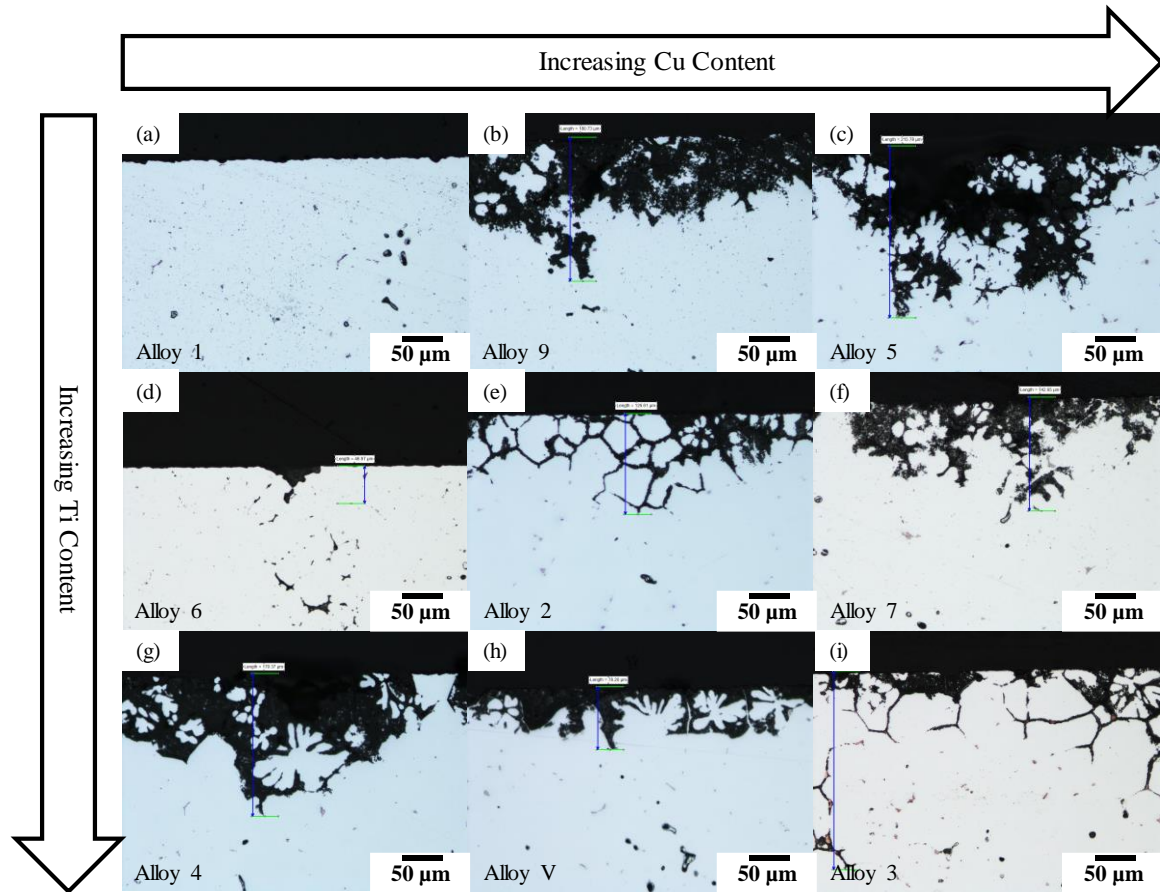


Figure 4.13: Light optical images of the corroded surface of alloys at the T6 temper in cross-section and after 96 h immersion in the modified EXCO solution (a) Al-3.4Zn-1.5Mg-0.04Ti (b) Al-6.5Zn-2.4Mg-1.3Cu-0.04Ti (c) Al-5.4Zn-2.2Mg-3Cu-0.05Ti (d) Al-5Zn-2.1Mg-0.12Ti (e) Al-3.6Zn-2Mg-1.5Cu-0.12Ti (f) Al-7Zn-1.7Mg-3Cu-0.15Ti (g) Al-5.1Zn-1.6Mg-1.4Cu-0.25Ti (h) Al-5.9Zn-1.6Mg-12.7Cu-0.2Ti (i) Al-3.6Zn-2.5Mg-2.9Cu-0.2Ti.

In Figure 4.13e and i show that alloys 2 and 3 exhibit intergranular corrosion in addition to IDC. Figure 4.14 shows that the grain size distribution in alloy 2 is bimodal due to the abnormal grain growth during the T4 temper, while that of alloy 3 is uniform and small due to the mitigation of abnormal growth from an increased Ti content in this alloy.

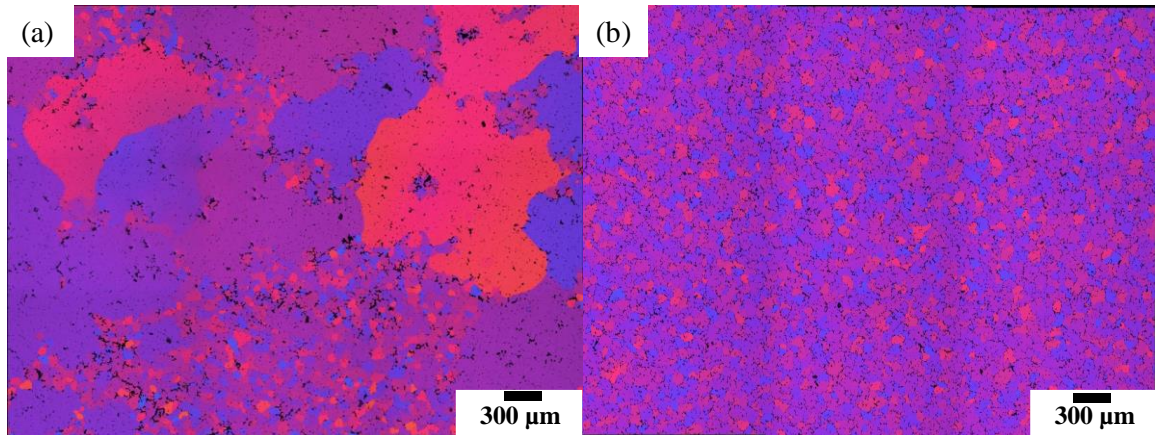


Figure 4.14: Light optical microscopy images of the typical microstructure found in (a) alloy 2 with a bimodal distribution of grain size due to abnormal grain growth and (b) alloy 3 with a uniform grain size.

Figure 4.15 shows images of the cross-sections of alloy 2 and 3 at various tempers after the modified EXCO experiments. Both alloys clearly display intergranular corrosion at the T6 temper, however, once overaging begins (T7x tempers) no intergranular corrosion is observed. Notably, IDC is visible in all tempers from T4 to T73. As mentioned previously, the abnormal grain growth does not change the size and morphology of the equiaxed dendrites of primary Al matrix, hence IDC remains unaffected by the various tempers. Alloys 2 and 3 are the only two alloys with a Zn to Mg weight ratio less than 2; hence, it is speculated that in these alloys, with Ti additions, that a weight ratio of Zn to Mg less than 2 is required for intergranular corrosion to occur.

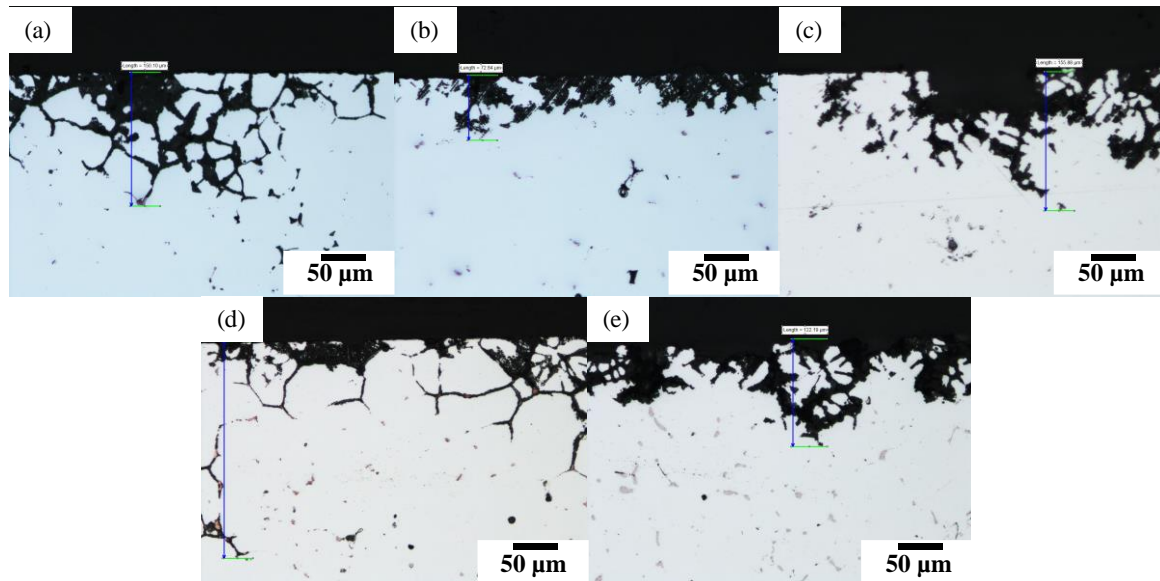


Figure 4.15: Light optical microscopy images of the corroded surface in cross-section after 96 h immersion in modified EXCO solution: (a) alloy 2 at the T6 temper (small grain area), (b) alloy 2 at the T6 temper (large grain area), (c) alloy 2 at the T79 temper (small grain area), (d) alloy 3 at the T6 temper and (e) alloy 3 at the T79 temper.

Alloy 2 contains the lowest total amount of alloying elements of all the Cu-containing alloys and has a weight ratio of 1.76 for Zn to Mg. Alloy 2 has a bimodal grain size, which has a significant effect on whether intergranular corrosion occurs or not. Figure 16a and b presents the photographs taken of the alloy 2 plate surface before and after the modified EXCO experiment, respectively. Figure 16c is a schematic of the photograph in Figure 16b with the areas of corrosion attack shaded in red and the large abnormal grain are demarcated with black lines. The area under the red shaded area is a region of small grains. Surface corrosion only occurs in area with the small grains (no abnormal growth). In alloy 2, there exists a mixed mode of corrosion propagation, intergranular corrosion and IDC. Intergranular corrosion occurs along the grain boundaries and is the dominant

Chapter 4: Results and Discussion

propagation mechanism in the small grain area because of the significantly larger grain boundary area in this region. However, IDC occurs throughout the sample, irrespective of the grain size. When corrosion is initiated, the IDC is the dominant propagation mode in large grain regions and the intergranular corrosion is dominant propagation mode in the small grain sections, as shown in Figure 4.15a and b.

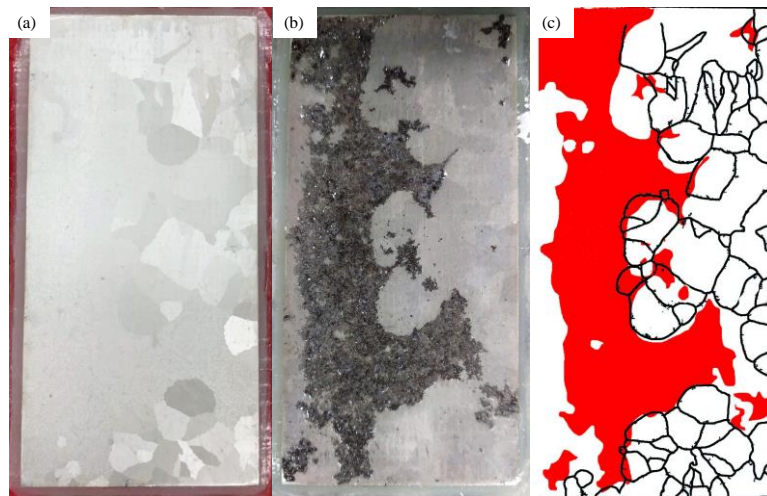


Figure 4.16: Photograph taken of the alloy 2 at the T6 temper plate sample (a) before immersion and (b) after 96 h of immersion in the modified EXCO solution. (c) Overlay of corroded areas (red) and large grain area (black outline).

Figure 4.16 shows that the corrosion extent in the small grain regions is significantly greater than that in the large grain regions. Since the dominant corrosion mode in the small grain region is the intergranular corrosion, it is safe to conclude that the corrosion mode has a strong influence on the corrosion extent: the extent due to intergranular corrosion being greater relative to that due to IDC. Evidently, the depth of attack in alloy 3 at the T6 temper is significantly greater than for the other tempers of this alloy. Alloy 3, with a weight ratio of 1.46 for Zn to Mg, does not have any abnormal large grain regions in the

microstructure. Since intergranular corrosion is only operative as a corrosion mode in the T6 temper (as shown in Figure 4.15), the small grain regions in this temper exhibit the largest depth of attack when compared to the other tempers of this alloy.

Figure 4.17 shows a secondary electron image of the alloy 3 at the T6 temper plate surface in the pristine (as-etched) condition. The surface of the sample includes many heterogeneities caused by the chemical etching process used to remove the active Zn-rich surface layer due to sample preparation. The surface exhibits no intergranular or interdendritic corrosion.

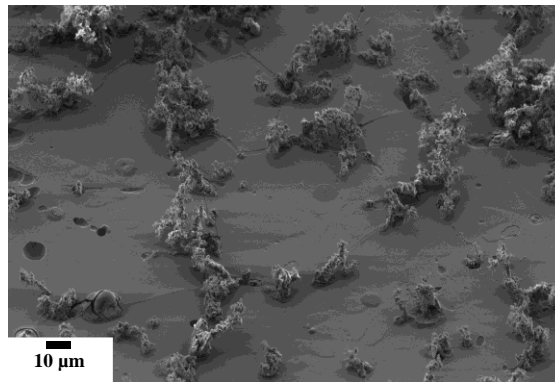


Figure 4.17: Secondary electron image of the alloy 3 at the T6 temper plate surface in the pristine (as-etched) condition.

Alloy 3 at the T6 temper was anodically polarized +50 mV_{SCE} above the breakdown potential at -683 mV_{SCE} in deaerated 0.5 M NaCl_(aq) for 5 min. to achieve the surface features shown in Figure 4.18. Figure 4.18b shows a typical plateaued current transient signifying that the sample shown is representative of a corroded sample. Intergranular corrosion is clearly apparent in this case. When compared to alloy 6 at the T6 temper (Figure 4.10), the difference of corrosion modes is evident. Corrosion does not deviate

Chapter 4: Results and Discussion

from the grain boundaries in alloy 3 at the T6 temper. The EDS maps of the alloy 3 at the T6 temper plate surface (Figure 4.19) show the absence of Al in the grain boundaries (lack of material) and Cu segregated at the grain boundaries (incorporated into the intermetallic particle precipitates). The Cu-containing particles were cross-sectioned using FIB milling and subsequently images using SEM.

Chapter 4: Results and Discussion

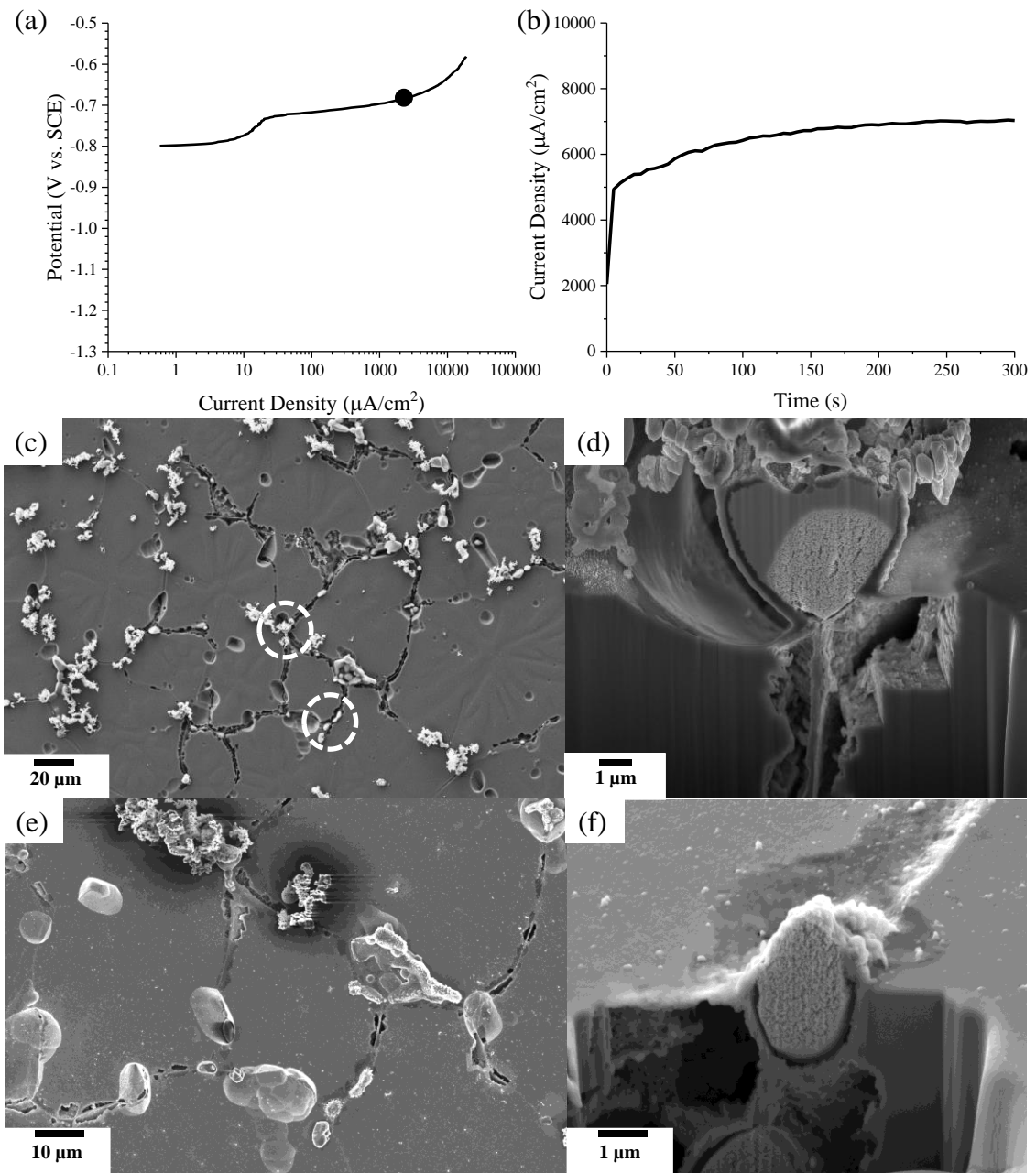


Figure 4.18: Results of the potentiostatic polarization experiment ($-683 \text{ mV}_{\text{SCE}}$ for 5 min. in deaerated $0.5 \text{ M NaCl}_{(\text{aq})}$) of alloy 3 at the T6 temper: (a) potentiodynamic curve (b) current density transient during potentiostatic polarization (c and e) secondary electron images of the polarized surface, (d and f) secondary electron images of FIB-prepared cross-section through partially dealloyed S-phase.

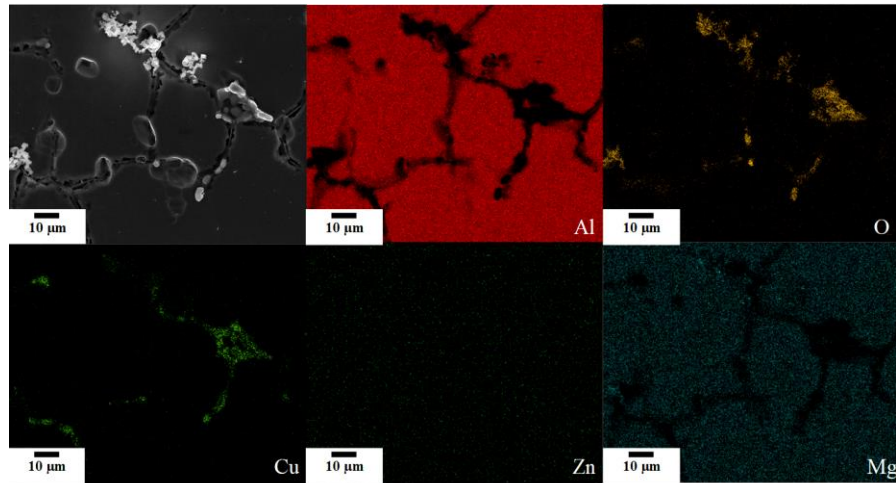


Figure 4.19: EDS elemental map of the polarized alloy 3 at the T6 temper plate surface showing enrichment of Cu phases along the grain boundaries.

Figure 4.18c and d show the cross-section of two intermetallic particles. The first particle analyzed is a partially dealloyed S-phase intermetallic particle (Figure 4.20). When the S-phase comes in contact with a $\text{NaCl}_{(\text{aq})}$, the particle initially serves as an anodic, setting up a microgalvanic cell with the surrounding PFZ, which serves as the cathode. The Al and Mg selectively dissolve from the S-phase, leaving behind a porous elemental Cu matrix. Following this, the residual Cu matrix becomes cathodic relative to the surrounding PFZ. Hence, PFZ begins to corrode. In the partially dealloyed S-phase particle, the portion in contact with the grain boundary has selectively dissolved leaving behind the porous Cu matrix, thus creating a microgalvanic cell with the PFZ allowing propagation via intergranular corrosion [3].

Chapter 4: Results and Discussion

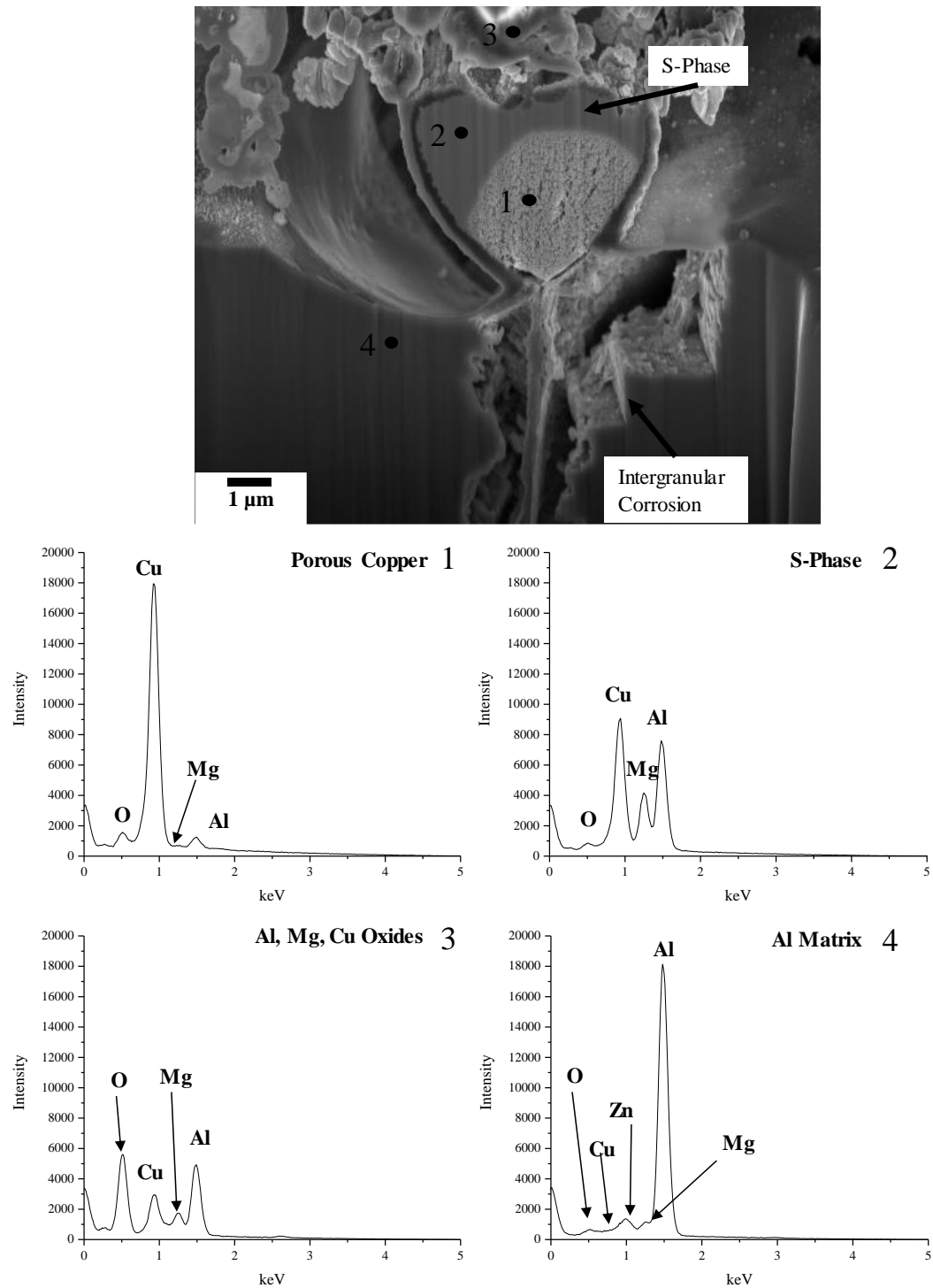


Figure 4.20: Secondary electron image of S-phase particle in cross-section and associated set of EDS spot analyses corresponding to the locations identified in the image for alloy 3 at the T6 temper.

Chapter 4: Results and Discussion

The TEM examination of alloy 3 at the T6 temper reveals Cu-containing precipitates form on the grain boundaries (Figure 4.21). These cathodic grain boundary precipitates cause the PFZ to be preferentially attacked [47]. In this alloy the grain boundary has remained intact, leaving a thin stem in the middle of the grain boundary. It has been reported that, in the AA6xxx alloys, a Cu-film exists along the grain boundary, which serves as a cathode for microgalvanic corrosion initiation [47]. However, after EDS line scans were acquired across grain boundaries, it is concluded that no Cu-film is present at the center of the grain boundary in alloy 3 at the T6 temper. The stem observed is likely indicative of a network of Cu-rich precipitates formed along the grain boundary. Notably, Mo and Ga peaks are identified on the EDS spectrum in Figure 4.21c. The Mo peak is a result of mounting the TEM sample on a Mo grid and the Ga peak is due to Ga impingement during the creation of an electron transparent sample in the FIB.

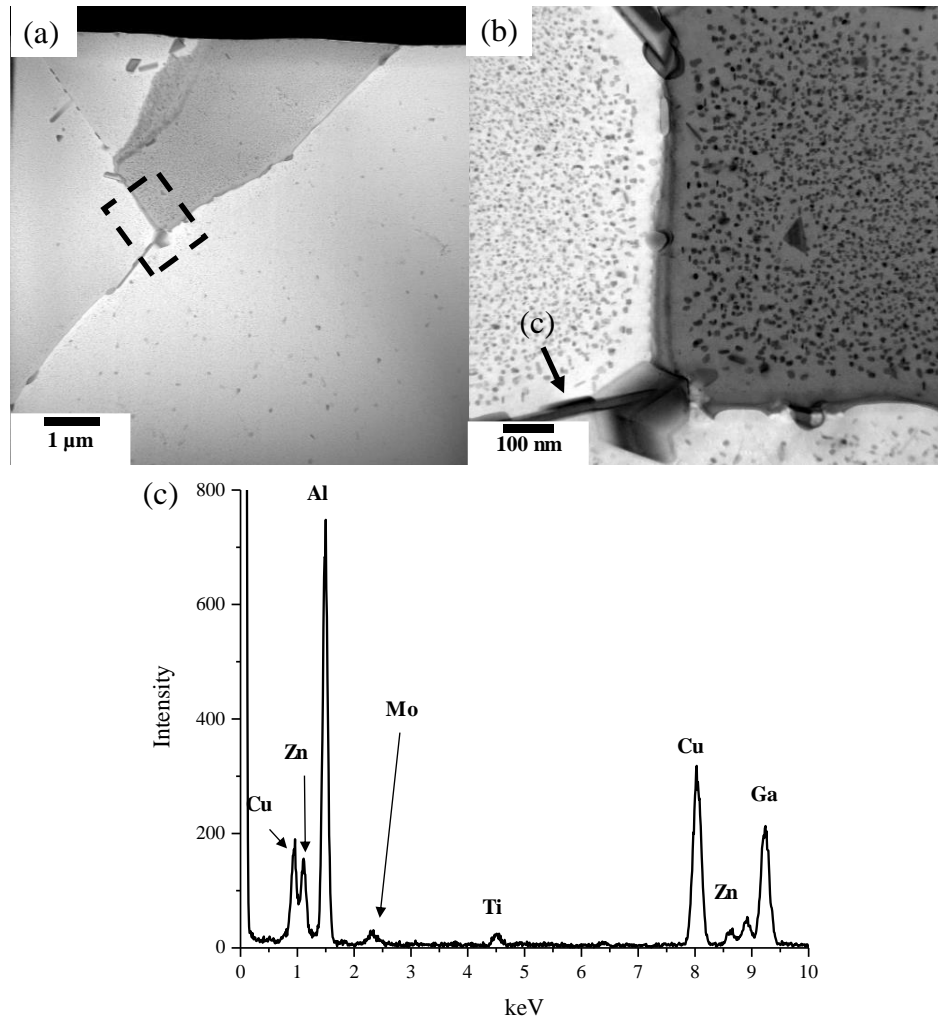


Figure 4.21: Bright field (BF) scanning TEM (STEM) images of alloy 3 at the T6 temper in the pristine condition (a) low magnification (b) grain boundary with Cu-rich precipitate formation (c) EDS spot analyses of the grain boundary precipitate identified in (b).

The S-phase particle in Figure 4.18f is fully dealloyed and is merely a Cu elemental network. These particles are the initiation site for the intergranular corrosion observed in alloy 3. Based on the compositional similarities between alloy 2 and 3, it is expected that alloy 2 initiates corrosion under a similar manner. Both alloy 2 and 3 have values of Zn to

Chapter 4: Results and Discussion

Mg weight ratios that are less than 2. Lower values of Zn to Mg ratio in the alloys leads to more Cu atoms substituting the Zn atoms in the lattice structure of the grain boundary precipitates; making them more cathodic and promoting the propagation of the intergranular corrosion, however, more work is required to substantiate this claim. All other alloys have a Zn to Mg ratio above 2, so there is less Cu in the precipitates and the primary mode of corrosion propagation is IDC rather than intergranular corrosion.

Once aged to the T79 (33% overage) temper, intergranular corrosion is not observed in the cross-sections of the corroded surfaces of both alloy 2 and 3 after 96 h immersion in the modified EXCO solution. Figure 4.22 and Figure 4.23 show the results from the dual platform FIB-SEM for alloy 3 at the T73 temper. The T73 rather than T79 temper was studied to ensure sufficient differences between peak and overaged tempers. In the pristine condition (Figure 4.22) the grains are intact and there are no signs of corrosion, whether it is intergranular, interdendritic or cooperative.

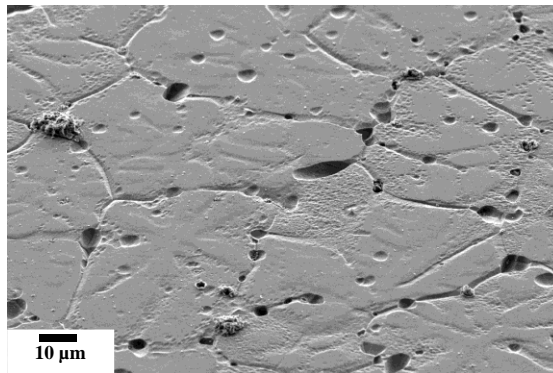


Figure 4.22: Secondary electron image of the alloy 3 at the T73 temper plate surface in the pristine (as-etched) condition.

Chapter 4: Results and Discussion

After holding the potential +50 mV_{SCE} above E_b (-696 mV_{SCE}), corrosion is no longer localized to the grain boundaries as is observed with the T6 temper: selective dissolution is also taking place in the interdendritic regions. Thus, there exists a mixed mode of corrosion. It is initiating at the S-phase, like with the T6 temper, but is propagating via intergranular corrosion and IDC. Figure 4.23 shows a cluster of fully dealloyed S-phase particles with both intergranular corrosion and IDC surrounding them. Clustering of both differing and similar intermetallic particles can lead to large stable pitting [39,74,75]. In Figure 4.23 there are instances where IDC is occurring with no link to intergranular corrosion.

Chapter 4: Results and Discussion

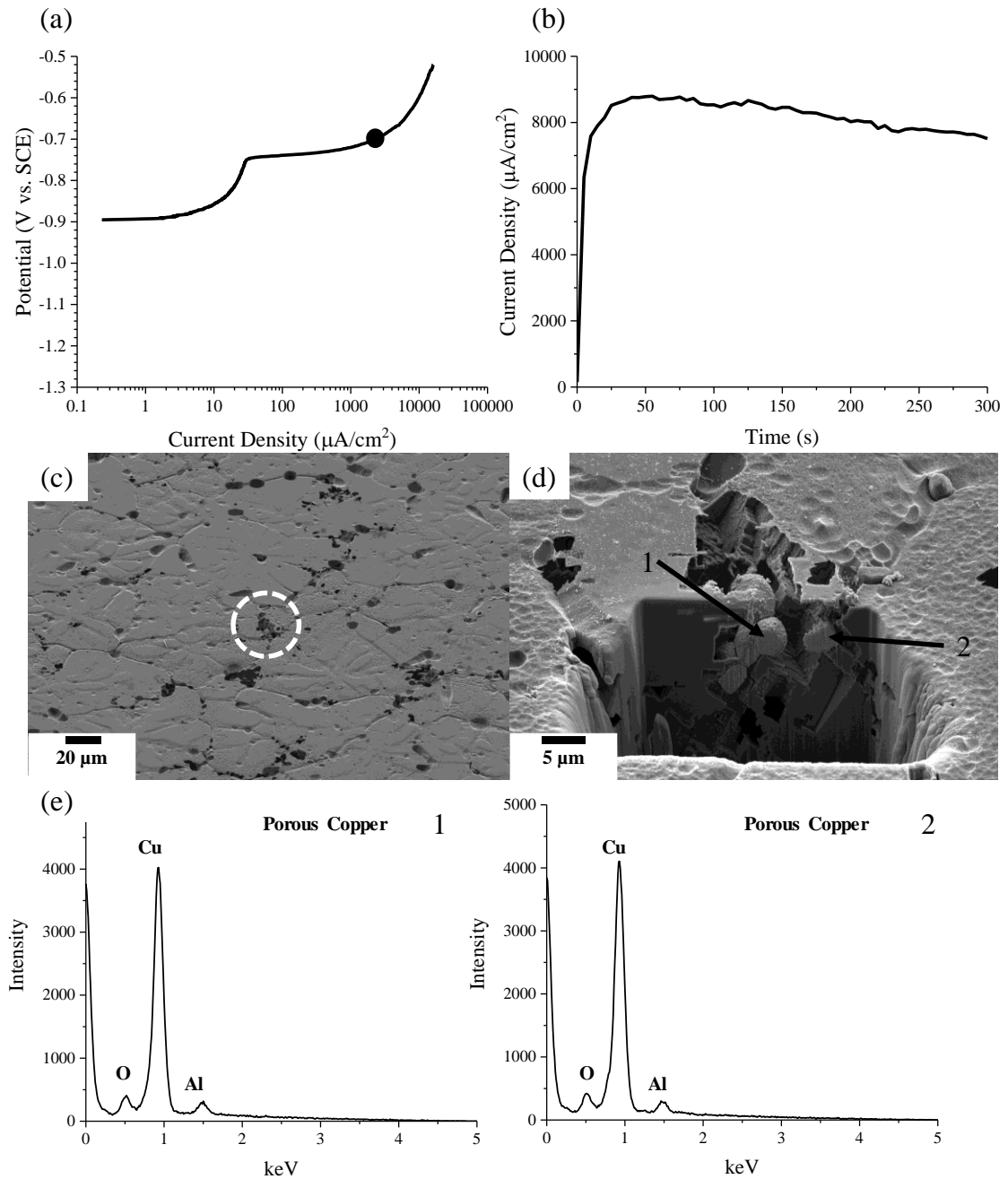


Figure 4.23: Results of the potentiostatic polarization experiment (-696 mV_{SCE} for 5 min. in deaerated 0.5 M NaCl_(aq)) of alloy 3 at the T73 temper: (a) potentiodynamic curve (b) current density transient during potentiostatic polarization (c) secondary electron image of polarized surface (d) secondary electron image of FIB-prepared cross-section through S-phase particle cluster, and (e) EDS spectra for selected locations identified in (d).

Artificial ageing effects the morphology of the grain boundary precipitates. Large grain boundary precipitates grow at the expense of smaller precipitates (coarsening). This creates larger precipitates, but also increases the distance between each precipitate. Intergranular corrosion needs a continuous galvanic path to propagate [3,47]. In the T6 condition the closely packed Cu-containing precipitates creates a continuous galvanic path for intergranular corrosion to propagate leaving behind a virtually unaffected stem, as observed in Figure 4.18c. Without the continuous galvanic path, as observed in the T7x temper, there is no driving force for the corrosion to localize along the grain boundaries allowing for IDC to dominate.

4.4.0 Summary of Corrosion Mechanisms in AA7xxx Alloys

Through electrochemical and immersion corrosion tests, 3 distinct corrosion mechanisms were active in these alloys; localized corrosion at precipitate/matrix interfaces, intergranular corrosion, and interdendritic corrosion. Once initiated all alloys were susceptible to interdendritic corrosion. Table 4.5 outlines a summary of the corrosion mechanisms observed in each of the alloys with the associated cross-sectional maximum depths of attack observed after immersion in the modified EXCO solution; wherein the corrosion susceptibility is presented as a function of Cu content, weight ratio of Zn to Mg and heat treatment temper of the alloy castings. In Table 4.5, the Cu-lean alloys show a higher corrosion tendency in the T4 temper condition when compared to the T6 and T7x tempers, except alloy 8 in the T73 temper. More work is required to identify the reason why this specific alloy and temper has a larger maximum depth of attack. The dominate

Chapter 4: Results and Discussion

corrosion propagation mode in these alloys is interdendritic corrosion (IDC). Notably, the Zn to Mg ratio does not appear to affect the corrosion in the Cu-lean alloys. In the Cu-containing alloys, the Zn to Mg ratio affects the corrosion mechanism and the critical ratio is 2. Alloys with Zn to Mg ratio of less than 2 exhibit corrosion propagation by intergranular corrosion in the T6 (peak aged) condition and hence, exhibits the highest corrosion tendency when compared to the T4 and T7x tempers, wherein the dominant corrosion propagation is interdendritic corrosion. In the Cu-containing alloys with Zn to Mg ratio greater than 2, the corrosion propagation mechanism is interdendritic corrosion and there is no appreciable difference in the corrosion tendencies amongst the heat treatment tempers of T4, T6 and T7x.

Alloy 2 and 3 are the only alloys to corrode by the intergranular corrosion mode. intergranular corrosion is an unfavourable mode of corrosion because:

- Alloy 3 in the T6 temper had the deepest penetration of attack during the modified EXCO experiment and was attributed to the increased susceptibility to intergranular corrosion.
- The propagation of interdendritic corrosion is not as affected by ageing, contrary to that in intergranular corrosion. Hence, both the T6 and any of T7x tempers would corrode in a similar and comparable manner.
- Stress corrosion cracking (SCC) is an extension of the intergranular corrosion, hence, if intergranular corrosion is mitigated then stress corrosion cracking could be mitigated, as well [51].

Chapter 4: Results and Discussion

- The stress intensity at the tip of the intergranular attack would lead to corrosion fatigue [51]. The stress intensities created through interdendritic corrosion would be less than intergranular corrosion because there are no microstructural features that would create locations of abnormally high concentrations of stress in the interdendritic regions.

Therefore, interdendritic mode of corrosion is preferable over intergranular corrosion mode, in the AA7xxx alloys.

Table 4.5: Summary of corrosion mechanisms in each alloy as a function of composition and temper.

Cu Content	Alloys	Zn/Mg weight ratio	Maximum Recorded Depth After Modified EXCO (μm)			Propagation
			T4	T6	T7x	
Cu-lean	1, 6, & 8	All	385	338	192,689*	IDC
Cu-containing	2 & 3	<2	315	543	379	IGC in T6 IDC in T4 & T7x
Cu-containing	4, 5, 7, 9, & V	>2	288	373	329	IDC

*Alloy 8 at the T73 temper experienced significantly more attack than any other alloy. All other Cu-lean alloys and tempers had a maximum depth of attack of 192 μm .

Increasing Ti concentration in the alloy mitigates the abnormal grain growth during T4 treatment and hence lead to uniform and small grains, as observed in alloys 3, 4, 6, and V. As stated earlier, abnormal grain growth is not beneficial for properties such as fracture toughness and fatigue crack resistance. The validation alloy (V) showed the best combination of uniaxial tensile strength and elongation from experimental optimization of the nine alloys.

Chapter 4: Results and Discussion

Considering corrosion susceptibility, uniaxial tensile properties and grain size an favourable alloy composition for structural automotive application would have the following characteristics:

- A high Cu alloy (approximately 3 wt.%) is beneficial for reduced hot tearing tendencies and high strength.
- A Zn/Mg ratio greater than 2 will prevent intergranular corrosion from occurring and interdendritic corrosion will be the only propagation mode.
- Ti concentrations in the alloy, greater than that required for optimal grain refinement would enable the mitigation of abnormal grain growth and lead to uniformly small grain size and benefit mechanical properties and performance of the cast component.

The composition and performance of the validation alloy in this study shows that it falls within the favourable regime for both uniaxial mechanical properties and corrosion resistance leading to conclude that it would be an apt candidate for structural automotive application.

Chapter 5: Conclusions

Casting high integrity near net shaped AA7xxx components by introducing Ti and B into the melt to promote a non-dendritic microstructure produced a unique microstructure due to the phenomena of athermal nucleation, unconstrained growth, and solute field impingement. A description of the microstructure evolution in these Ti-containing AA7xxx alloys is provided below:

- During the initial stages of solidification, copious nucleation of the primary Al phase takes place on preferential lattice planes of the grain refiner inoculant, possibly TiB_2 . As the melt temperature drops the solid-liquid (S/L) interface grows as equiaxed dendrites due to the constitutional supercooling enhanced by the negative thermal gradient ahead of the solidification front leading to significant breakdown of the S/L interface during growth. Additionally, the effect of significant curvatures in the equiaxed dendrites, results in the curvature undercooling, which is governed by the Gibb-Thompson effect and the contribution of the curvature returns the growth S/L interface back to planarity. However, the effect of curvature is significantly less than that of the constitutional undercooling during the initial stages of solidification.
- During the later stages of dendritic solidification, solute field impingement occurs and results in the equalization of the solute and thermal gradients between impinging dendrites. At this stage, the constitutional and thermal

Chapter 5: Conclusions

undercooling factors diminish, while the curvature effect on the growth begins to dominate. Hence, at the later stages of solidification the growth transforms back to a nearly planar S/L interface resulting in a non-dendritic primary Al grain in the microstructure.

- The eutectic phase forms at the end of solidification in the intergranular regions producing a rich environment of secondary phases along the grain boundaries.

The following summarizes the major findings associated with the corrosion tendencies of the unique above-mentioned microstructure of the castings produced with the AA7xxx alloys.

1. A multivariate regression model was developed to predict the mean value of breakdown potential, E_b as a function of alloy composition and heat treatment. However, the effect of Zn (3.4 to 7 wt%), Mg (1.5 to 2.5 wt%) and Ti (0.04 to 0.25 wt%), individually, have no discernable effect on variation of E_b in the alloy castings. However, the individual effect of Cu (0.02 to 3 wt%) and the weight ratio of Zn/Cu have a pronounced effect on the same. An empirical semi-logarithmic model was developed to predict E_b at various heat treatment tempers, as a function of the weight ratio of Zn/Cu.
2. The depletion of Zn and Cu from the solid solution of the Al matrix due to the formation of the strengthening intermetallic precipitates increases and decreases the value of E_b , respectively. In Cu-lean alloys ($Zn/Cu > 44$), there is a continually increasing trend for E_b when aged from the T4 to T73 tempers due to the absence

Chapter 5: Conclusions

of any Cu-depletion to counteract the effects of the Zn-depletion in the matrix. In alloys with some Cu addition, specifically for $Zn/Cu \cong 5$, E_b increased when aged from the T4 to T6 tempers due to the dominance of the Zn-depletion over that of Cu in the matrix; the value of E_b remained relative constant between the T6 and T73 tempers. In alloys with high Cu content such as $Zn/Cu < 5$, results in no significant change in E_b from ageing between the T4 and T73 tempers.

3. In alloys with Cu additions, the initiation of corrosion predominantly occurs at the Cu-containing secondary phases in the intergranular regions of the microstructure. While the initiation occurs on the Fe-containing intermetallic phases in alloys without Cu additions.
4. There were two modes of corrosion propagation in these alloys: interdendritic corrosion (IDC) and intergranular corrosion (IGC). IDC is present in all the alloy compositions and heat treatment tempers, while IGC is only present in alloys with $Zn/Mg < 2$ in the T6 temper condition, alone. The equiaxed dendrite imprints created during the first regime of solidification leads to the selective dissolution of the interdendritic region that solidified under the curvature undercooling. In all the Cu-containing alloys of this study, the level of corrosion propagation remains nearly the same and is independent of alloy composition or heat treatment temper between T4 and T73; because, the dendritic features do not change size or morphology with ageing, the propagation of IDC is not mitigated in Cu-containing alloys with heat treatment contrary to IGC. In the Cu-lean alloys, the T6 and T7x temper conditions show low levels of IDC in the modified EXCO experiments, due to the lack of

Chapter 5: Conclusions

detrimental galvanic couples between Cu-containing precipitates and surrounding matrix to act as initiation sites. However, in the T4 temper condition of the Cu-lean alloys, the susceptibility to IDC increases due to the large galvanic difference between an anodic Zn-rich solid solution and the cathodic Fe-containing intermetallic phases. Regardless, the extent of corrosion is greater with the IGC mode.

5. Alloys with $Zn/Mg < 2$ are susceptible to IGC in the T6 temper condition alone. Relatively cathodic grain boundary precipitates likely cause the dissolution of the anodic PFZ. In the T6 temper condition, corrosion is localized to the grain boundary, but with subsequent ageing to the T73 temper, a combination of IGC and IDC occur.
6. The Al-6Zn-1.6Mg-2.3Cu-0.25Ti (validation) alloy, developed as the optimized composition for maximum uniaxial tensile properties, corrodes by IDC and performs no worse than other Cu-containing alloys in the modified EXCO experiments.
7. There was no evidence of exfoliation corrosion in the modified EXCO experiments in any of the alloy compositions and heat treatment tempers evaluated in this study.
8. In the alloy 6 after the T6 and T79 tempers, chemically etching the surface to remove the active surface layer created during etching could selectively dissolve the Al from Fe-Al intermetallic phases leaving behind an elemental Fe matrix. When exposed to a saline environment, the matrix likely passivates to $Fe(OH)_2$ creating an active-passive region on the potentiodynamic curve. Hence, the

Chapter 5: Conclusions

chemical etching during these experiments could cause artifacts in the microstructure that may lead to abnormal potentiodynamic data.

Chapter 6: Future Work

1. The formation of second phases in this thesis was predicted using solidification simulations completed in Pandat. These simulations provided an approximation of the expected phases, but an in-depth study of actual precipitates and intermetallic particles that formed is required. SEM equipped with EDS is required to identify the detrimental intermetallic phases of all alloys prior to exposure in a corrosive environment in each temper for a more complete understanding of structure-property relationships. Providing an extensive second phase characterization of the materials would aid in the investigation of detrimental initiation sites in these alloys.

Using TEM, the grain boundaries of each alloy and temper needs to be investigated for grain boundary precipitate growth and composition of those precipitates. IGC is dependant on grain boundary chemistry. The conclusion that IGC in these alloys only occurs with a Zn/Mg less than 2 would be made more concrete by compositional characterizing of the precipitates and how it changes as a function of the alloy Zn/Mg weight ratio. The conclusion that Zn and Cu-depletion is the mechanism behind the changing E_b can be substantiated by chemical characterization of the bulk as a function of ageing and temper.

The structure and composition of the dendritic imprints needs characterization to better understand the IDC mechanism. Atom probe tomography (APT) is an attractive tool to elucidate concentration gradients and particle

Chapter 6: Future Work

formation from the center of the dendrite, across a dendritic arm, and at the dendrite α -Al interface

2. In this study corrosion was observed to initiate at both Cu-containing and Fe-containing intermetallic phases, however it is likely that Fe-containing intermetallic phases exist in Cu-containing alloys. Therefore, it is reasonable to assume there exists a transition where the initiation mode transitions from Fe-containing to Cu-containing intermetallic phases, this transition point needs to be investigated further to better understand localized corrosion initiation.
3. The grain size was characterized as being bimodal or uniform due to abnormal grain growth in alloys that contained an insufficient Ti-content to promote a uniform grain size. Investigating the minimum amount of Ti required to create a uniform grain size as a function of other alloying elements (Zn, Mg, and Cu) is required to understand the grain growth phenomenon.
4. Characterization of IMPs before and after removal of the altered surface layer requires clarity. The removal of the altered surface layer is required for accurate potentiodynamic results, but not if it causes unexpected side-effects. It was proposed that the chemical etch selectively dissolved the Al from the $Al_{13}Fe_4$ intermetallic particle creating an active passive region in the potentiodynamic polarization curve in alloy 6. As well, it was noted that after the chemical etch oxide remnants were found on the surface in Alloy 3 T6 during the dual platform FIB-SEM investigation.

Chapter 6: Future Work

5. Alloy 6 requires special consideration. The potentiodynamic polarization produced multiple breakdowns that were affected by ageing. Although, the T6 and T79 active-passive region was attributed to selective dissolution of Al in the $Al_{13}Fe_4$ intermetallic particle, it doesn't explain how the potentiodynamic curve changes with temper. Further potentiostatic and dual beam FIB-SEM investigations would provide mechanistic insight for the cause of these abnormalities.

Chapter 7: Appendix

7.1.0 Alloy 1

Table 7.1: Alloy 1 compositions as determined by GDOES.

	Zn (wt%)	Mg (wt%)	Cu (wt%)	Ti (wt%)	Si (wt%)	Fe (wt%)	Mn (wt%)	Sn (wt%)	Al (wt%)	(Zn+Mg+Cu) (wt%)	Zn/Cu (wt%)	Zn/Mg (wt%)
TPGC	3.2	1.4	0.02	0.06	0.02	0.05	0.02	0.01	Bal.	4.6	160	2.3
Permanent Mould	3.4	1.5	0.05	0.04	0	0.06	0.02	0.02	Bal.	4.9	68	2.3

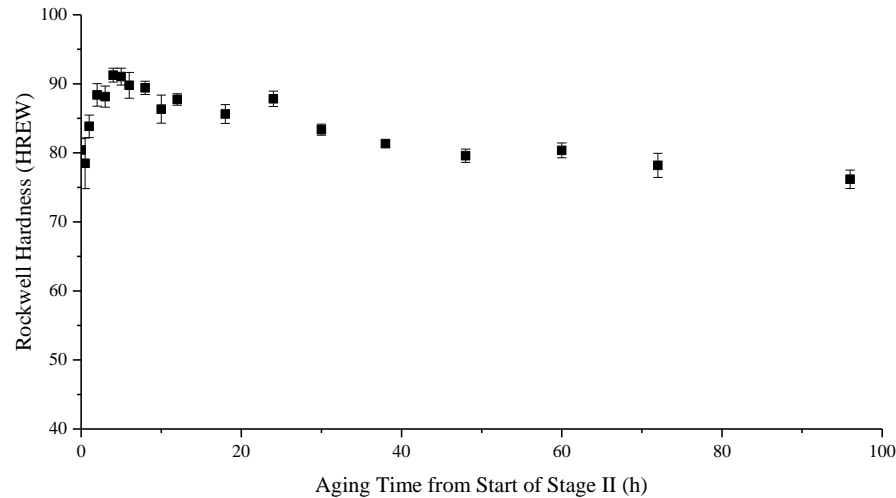


Figure 7.1: Ageing curve for alloy 1 at 185°C (HREW).

Table 7.2: Rockwell hardness and associated ageing time for Alloy 1.

Temper	Rockwell Hardness (HREW)	Stage II Ageing Time (h)
T6	56	5
T79	86	10
T76	82	37
T73	78	65

Chapter 7: Appendix

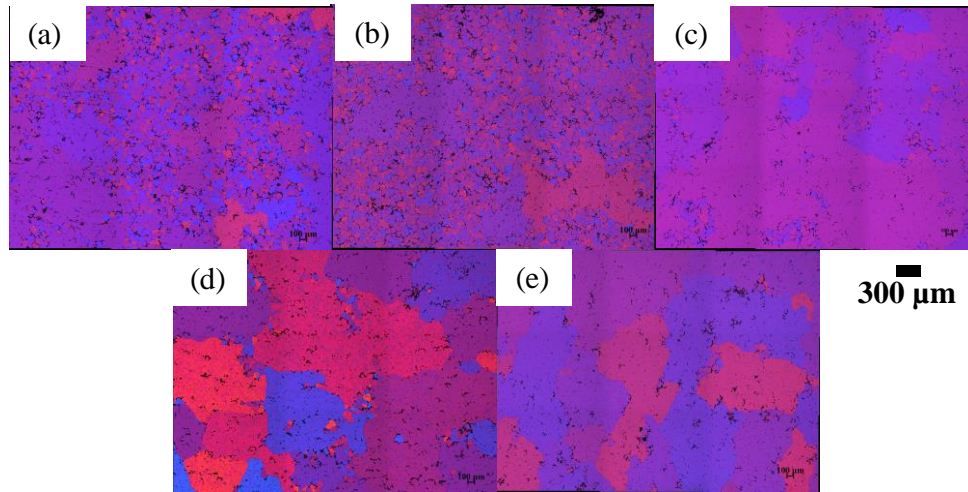


Table 7.3: Alloy 1 grain size summary.

Temper	T4	T6	T79	T76	T73
Area Fraction of Small Grains	0.82	0.93	0.32	0.1	0.02
Average Small ECD (μm)	33	29	61	29	62
95% Error (μm)	1	0.5	1.4	1.2	4.8
Area Fraction of Large Grains	0.18	0.07	0.68	0.9	0.98
Average Large ECD (μm)	141	146	667	560	701
95% Error (μm)	20	24	86	25	190

Figure 7.3: Alloy 1 micrographs at 100x of (a) T4 (b) T6 (c) T79 (d) T76 (e) T73.

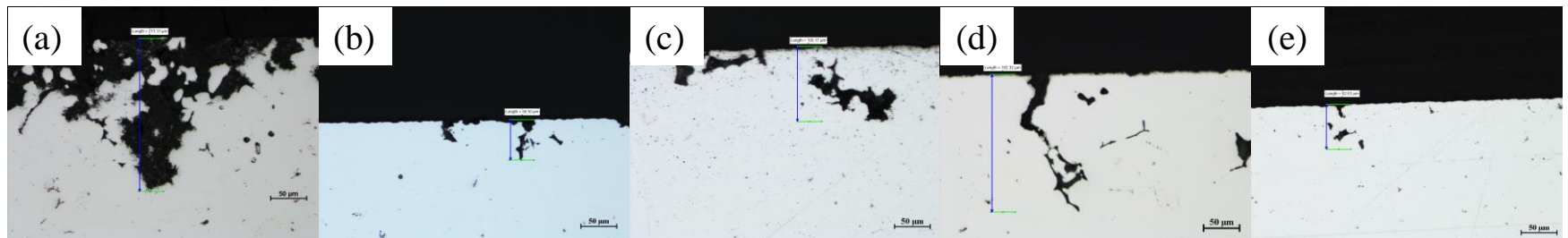


Figure 7.2: Alloy 1 cross-sections after 96 h immersion in EXCO solution at 200x (a) T4 (b) T6 (c) T79 (d) T76 (e) T73. Scale is 50 μm.

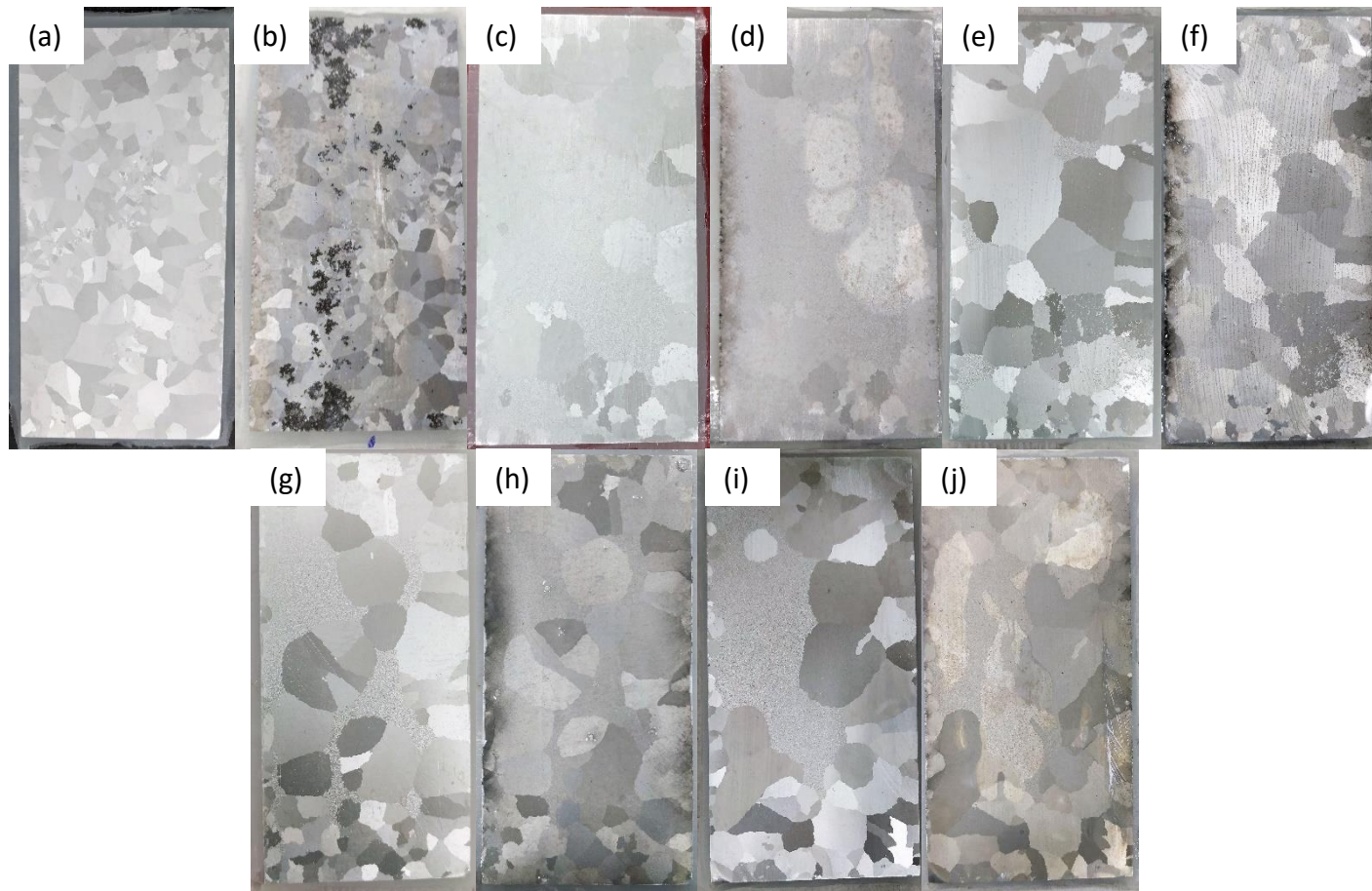


Figure 7.4: Alloy 1 images before and after immersion in modified EXCO solution (a-b) T4 (c-d) T6 (e-f) T79 (g-h) T76 (i-j) T73.

Chapter 7: Appendix

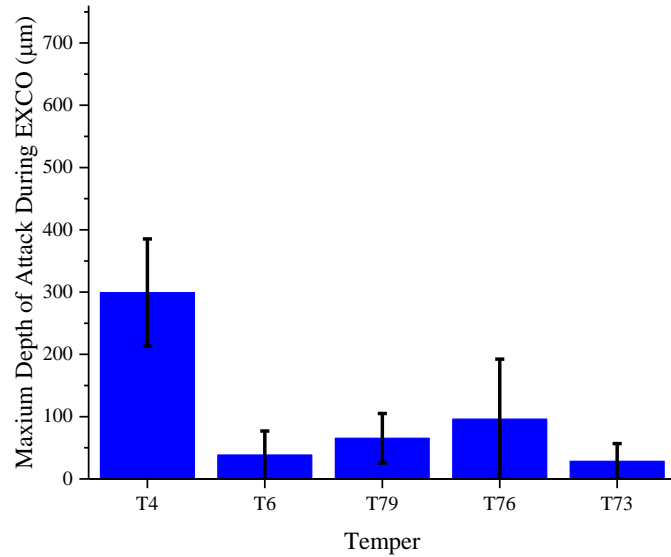


Figure 7.6: Alloy 1 maximum depth of penetration observed in cross-section after 96 h of immersion in modified EXCO solution.

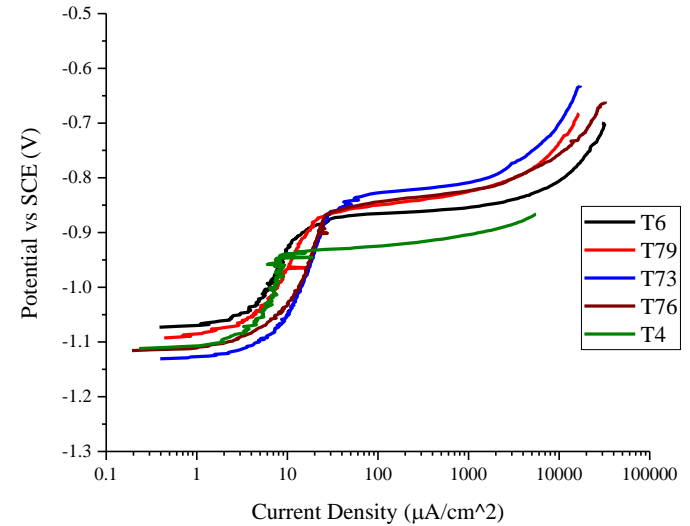


Figure 7.5: Alloy 1 potentiodynamic polarizations in deaerated 0.5M NaCl_(aq) solution.

Alloy 1 was a Cu-free alloy with the lowest total overall alloying elements. The microstructure contains a bimodal grain size distribution due to abnormal grain growth. Due to the low alloying content, alloy 1 was the softest of the ten tested in this study. The T4 condition had the most surface damage and largest depth of attack recorded during the modified EXCO test. The breakdown potential increased from T4 to T73 due to the depletion of Zn from the matrix (high Zn/Cu ratio).

Chapter 7: Appendix

7.2.0 Alloy 2

Table 7.4: Alloy 2 compositions as determined by GDOES.

	Zn (wt%)	Mg (wt%)	Cu (wt%)	Ti (wt%)	Si (wt%)	Fe (wt%)	Mn (wt%)	Sn (wt%)	Al (wt%)	(Zn+Mg+Cu) (wt%)	Zn/Cu (wt%)	Zn/Mg (wt%)
TPGC	3.2	1.8	1.2	0.17	0.02	0.05	0.02	0.01	Bal.	6.2	2.67	1.8
Permanent Mould	3.6	2.0	1.5	0.12	0	0.07	0.02	0.02	Bal.	7.1	2.4	1.8

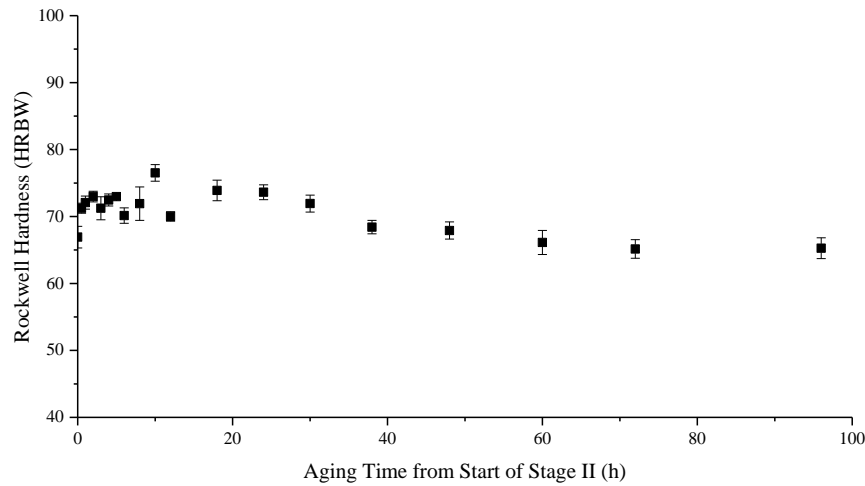


Figure 7.7: Ageing curve for alloy 2 at 185°C (HRBW).

Table 7.5: Rockwell hardness and associated ageing time for alloy 2.

Temper	Rockwell Hardness (HRBW)	Stage II Ageing Time (h)
T6	75	10
T79	72	20
T76	69	37
T73	67	58

Chapter 7: Appendix

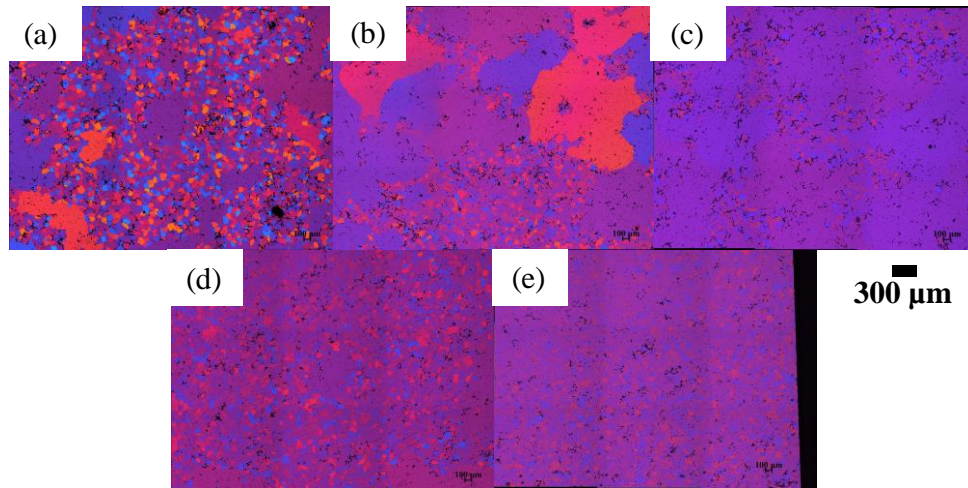


Table 7.6: Alloy 2 grain size summary.

Temper	T4	T6	T79	T76	T73
Area Fraction of Small Grains	0.82	0.1	0.48	0.67	0.55
Average Small ECD (μm)	36	49	46	50	52
95% Error (μm)	0.7	1.5	0.8	0.7	1.2
Area Fraction of Large Grains	0.18	0.9	0.52	0.33	0.45
Average Large ECD (μm)	170	353	252	168	168
95% Error (μm)	30	94	87	15	13

Figure 7.9: Alloy 2 micrographs at 100x of (a) T4 (b) T6 (c) T79 (d) T76 (e) T73.

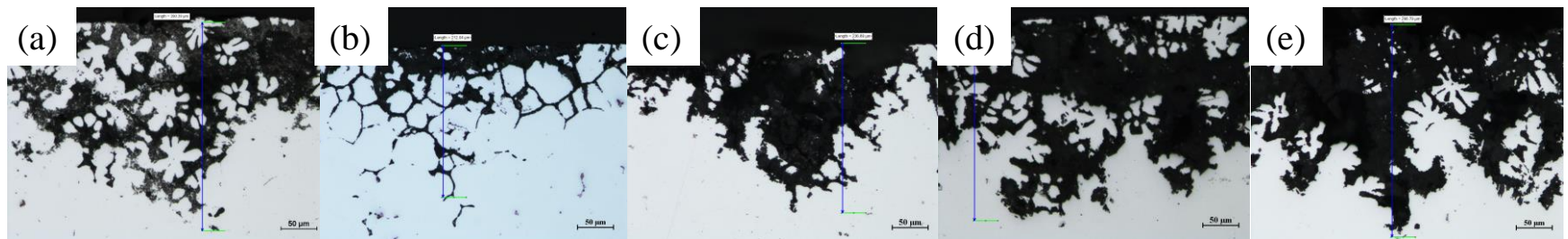


Figure 7.8: Alloy 2 cross-sections after 96 h immersion in EXCO solution at 200x (a) T4 (b) T6 (c) T79 (d) T76 (e) T73. Scale is 50 μm.

Chapter 7: Appendix

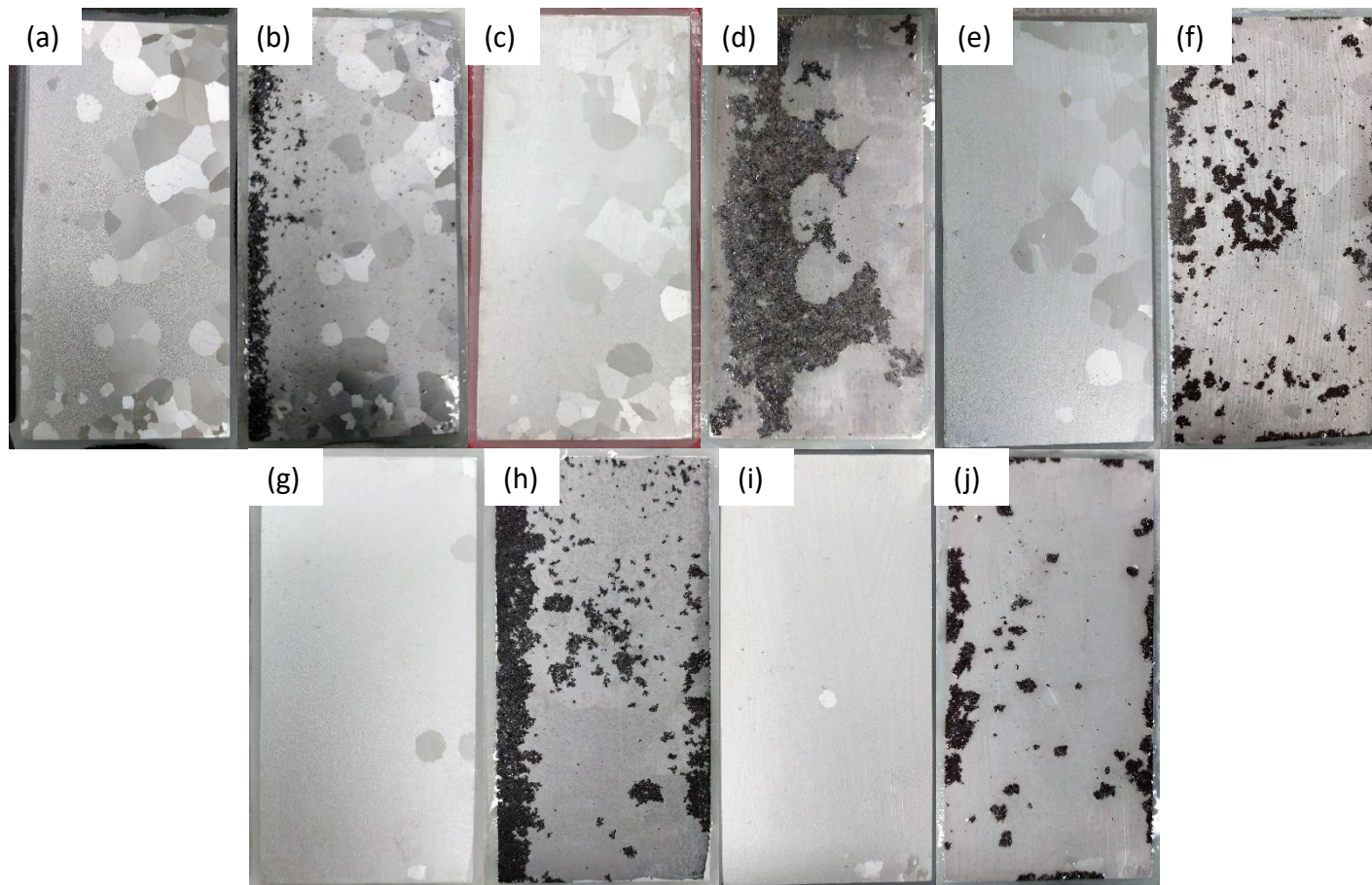


Figure 7.10: Alloy 2 images before and after immersion in modified EXCO solution (a-b) T4 (c-d) T6 (e-f) T79 (g-h) T76 (i-j) T73.

Chapter 7: Appendix

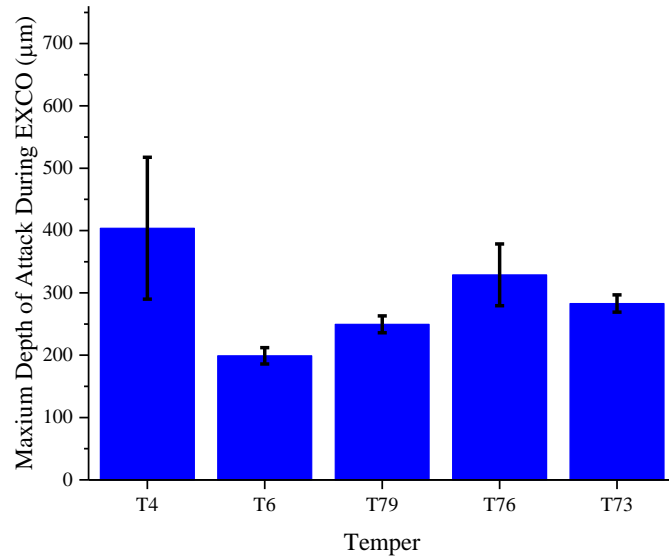


Figure 7.12: Alloy 2 maximum depth of penetration observed in cross-section after 96 h of immersion in modified EXCO solution.

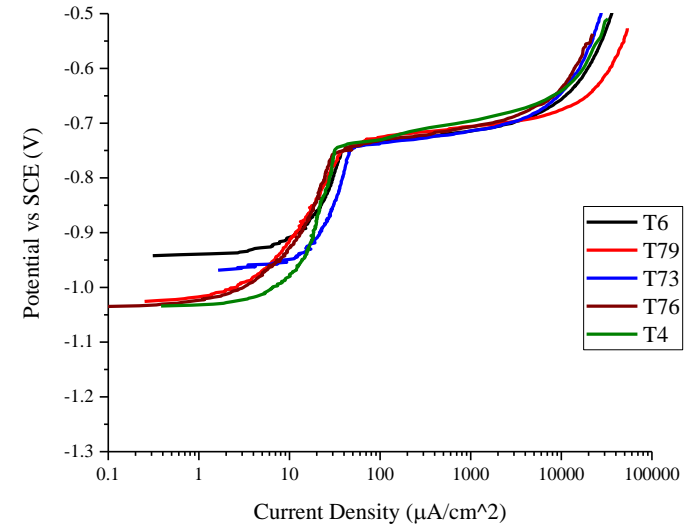


Figure 7.11: Alloy 2 potentiodynamic polarizations in deaerated 0.5M NaCl_(aq) solution.

Alloy 2 had the lowest total alloying content of all Cu-containing alloys. A Zn/Mg ratio below 2 limits the ageing response of the alloy. The low Zn/Mg ratio also leads to intergranular corrosion in the T6 temper during the modified EXCO test, but the bimodal distribution of small and large grains leads to a mixed mode of corrosion with interdendritic corrosion. Along the grain boundaries intergranular corrosion dominates, but within the grains IDC takes control. No significant change in maximum depth of attack is observed with temper. Due to a competition between Zn and Cu-depletion in the matrix there is no significant change in breakdown potential as ageing proceeds from T4 to T73.

7.3.0 Alloy 3

Table 7.7: Alloy 3 compositions as determined by GDOES.

	Zn (wt%)	Mg (wt%)	Cu (wt%)	Ti (wt%)	Si (wt%)	Fe (wt%)	Mn (wt%)	Sn (wt%)	Al (wt%)	(Zn+Mg+Cu) (wt%)	Zn/Cu (wt%)	Zn/Mg (wt%)
TPGC	3.4	2.4	2.7	0.2	0.02	0.07	0.02	0.01	Bal.	8.5	1.26	1.4
Permanent Mould	3.6	2.5	2.9	0.2	0	0.08	0.01	0.02	Bal.	9	1.24	1.4

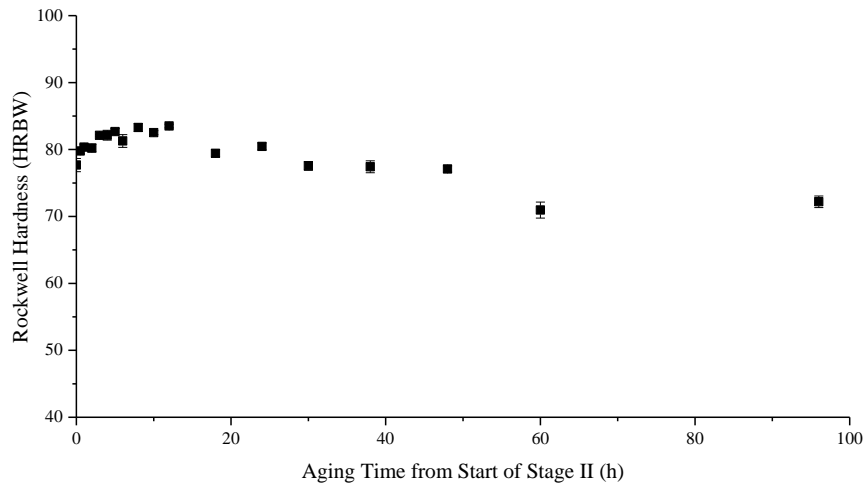


Figure 7.13: Ageing curve for alloy 3 at 185°C (HRBW).

Table 7.8: Rockwell hardness and associated ageing time for alloy 3.

Temper	Rockwell Hardness (HRBW)	Stage II Ageing Time (h)
T6	83	8
T79	80	20
T76	76	40
T73	72	54

Chapter 7: Appendix

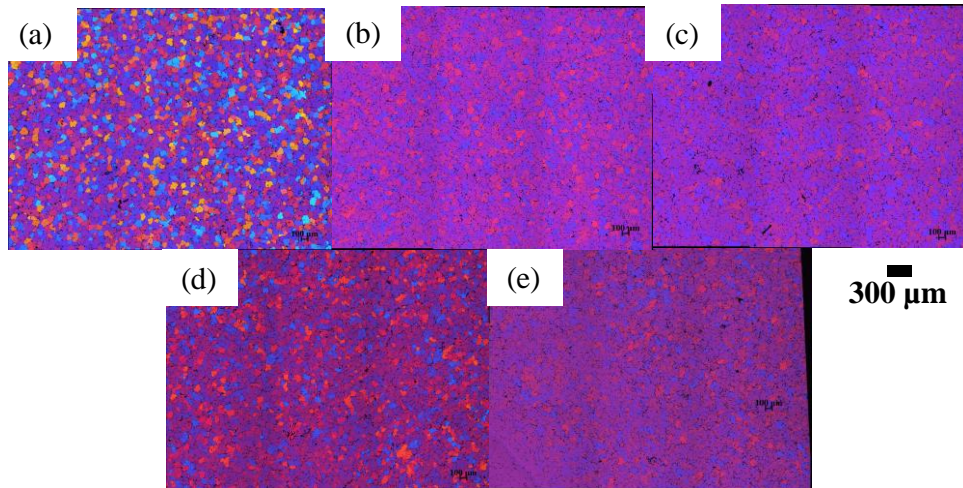


Table 7.9: Alloy 3 grain size summary.

Temper	T4	T6	T79	T76	T73
Area Fraction of Small Grains	1	1	1	1	1
Average Small ECD (μm)	61	64	64	64	57
95% Error (μm)	1	1.7	2.2	1.5	2.1
Area Fraction of Large Grains					
Average Large ECD (μm)					
95% Error (μm)					

Figure 7.15: Alloy 3 micrographs at 100x of (a) T4 (b) T6 (c) T79 (d) T76 (e) T73.

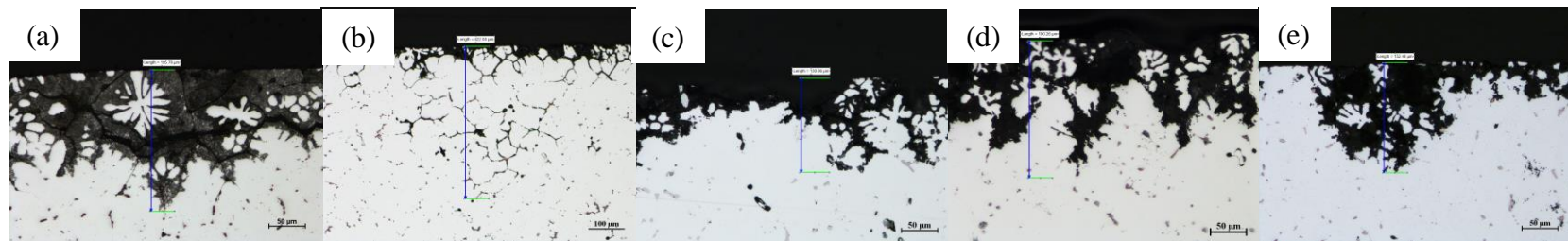


Figure 7.14: Alloy 3 cross-sections after 96 h immersion in EXCO solution at 200x (a) T4 (b) T6 (c) T79 (d) T76 (e) T73. Scale is 50 μm.*

* Note (b) was taken at 100x rather than the standard 200x. The scale in (b) is 100 μm

Chapter 7: Appendix

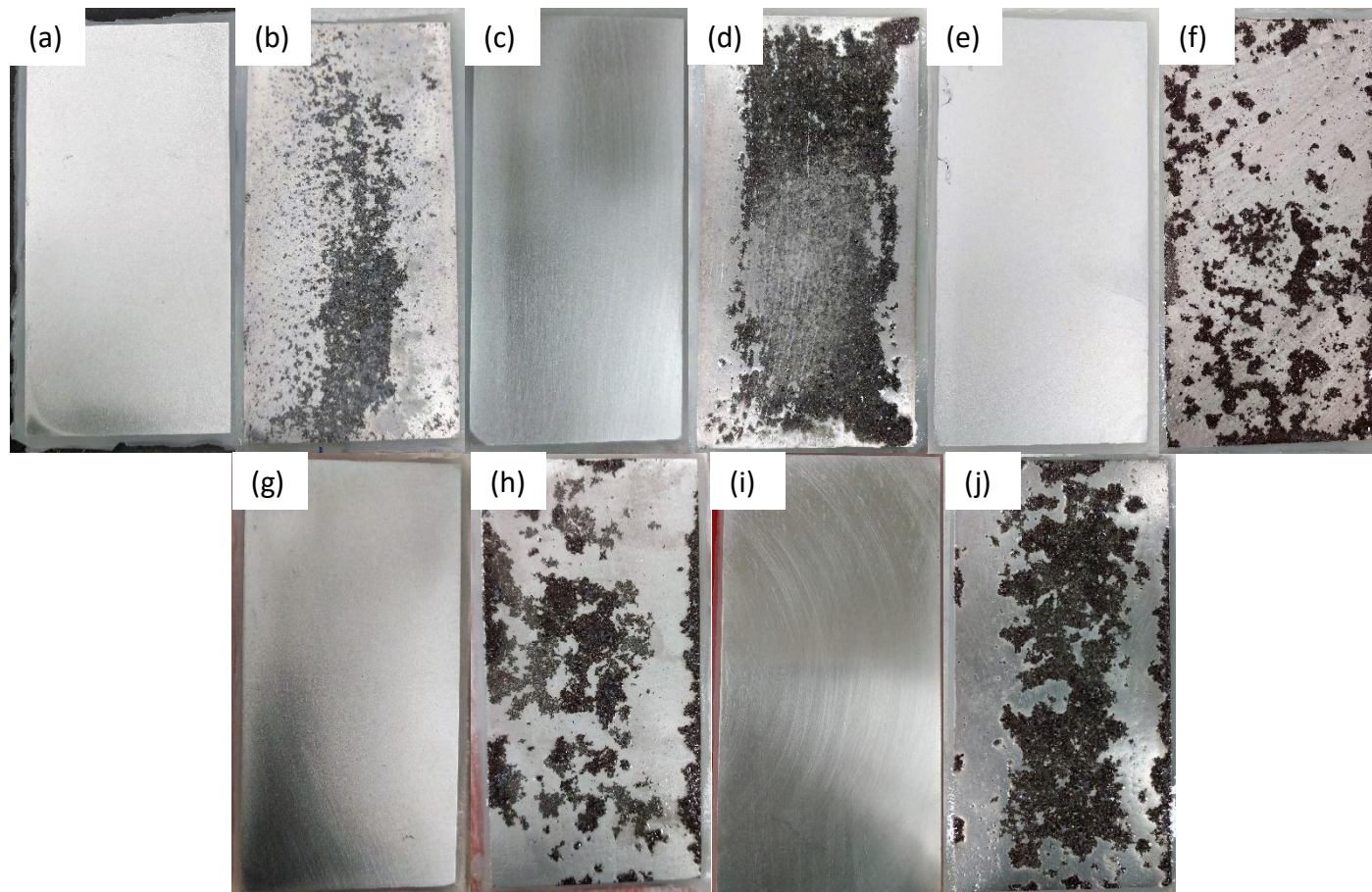


Figure 7.16: Alloy 3 images before and after immersion in modified EXCO solution (a-b) T4 (c-d) T6 (e-f) T79 (g-h) T76 (i-j) T73.

Chapter 7: Appendix

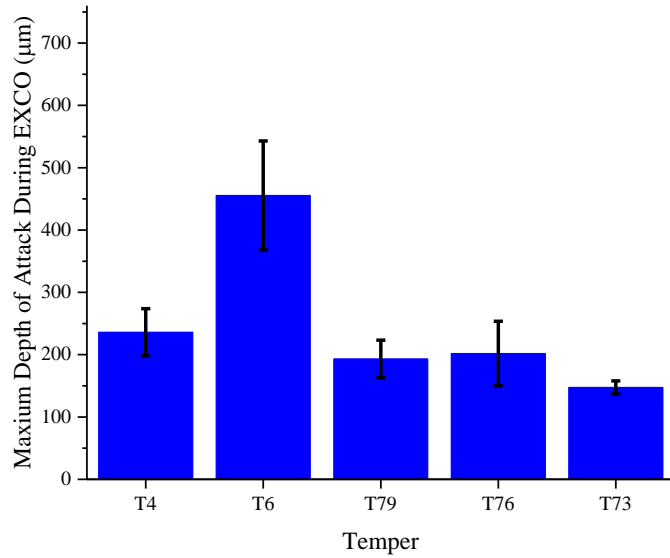


Figure 7.18: Alloy 3 maximum depth of penetration observed in cross-section after 96 h of immersion in modified EXCO solution.

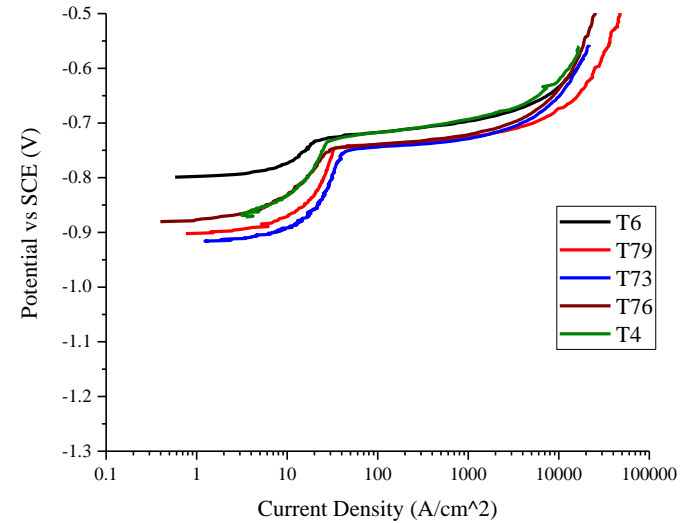


Figure 7.17: Alloy 3 potentiodynamic polarizations in deaerated 0.5M NaCl_(aq) solution.

Alloy 3 had the second lowest total alloying content of all Cu-containing alloys. A Zn/Mg ratio below 2 limits the ageing response of the alloy. The low Zn/Mg ratio also leads to intergranular corrosion in the T6 temper during the modified EXCO test. Unlike Alloy 2, alloy 3 had a uniform grain size therefore, intergranular corrosion is the dominate mechanism with the secondary mechanism of IDC. Aside from T6 IDC is the dominate mechanism. Due to intergranular corrosion, the maximum depth of attack in the T6 condition is significantly higher. The competition between Zn and Cu-depletion in the matrix leads to no significant change in breakdown potential as ageing proceeds from T4 to T73.

7.4.0 Alloy 4

Table 7.10: Alloy 4 compositions as determined by GDOES.

	Zn (wt%)	Mg (wt%)	Cu (wt%)	Ti (wt%)	Si (wt%)	Fe (wt%)	Mn (wt%)	Sn (wt%)	Al (wt%)	(Zn+Mg+Cu) (wt%)	Zn/Cu (wt%)	Zn/Mg (wt%)
TPGC	4.8	1.5	1.3	0.18	0.02	0.06	0.02	0.01	Bal.	7.6	3.7	3.2
Permanent Mould	5.1	1.6	1.4	0.25	0	0.07	0.02	0.02	Bal.	8.1	3.64	3.2

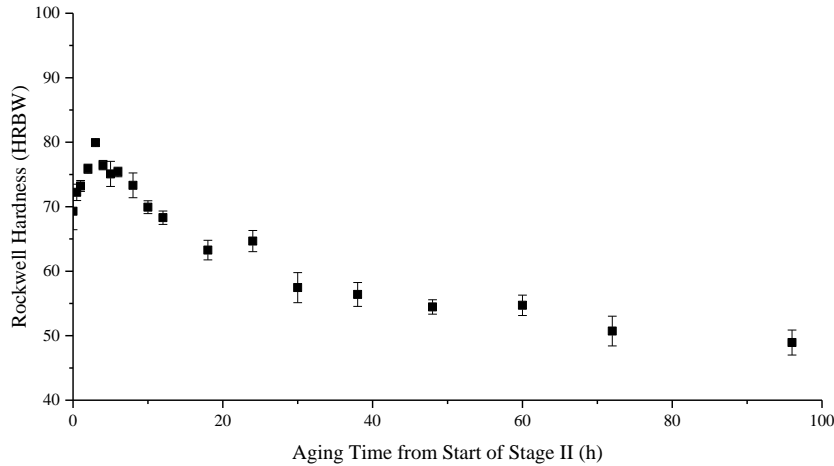


Figure 7.19: Ageing curve for alloy 4 at 185°C (HRBW).

Table 7.11: Rockwell hardness and associated ageing time for alloy 4.

Temper	Rockwell Hardness (HRBW)	Stage II Ageing Time (h)
T6	80	3
T79	70	10
T76	59	28
T73	48	64

Chapter 7: Appendix

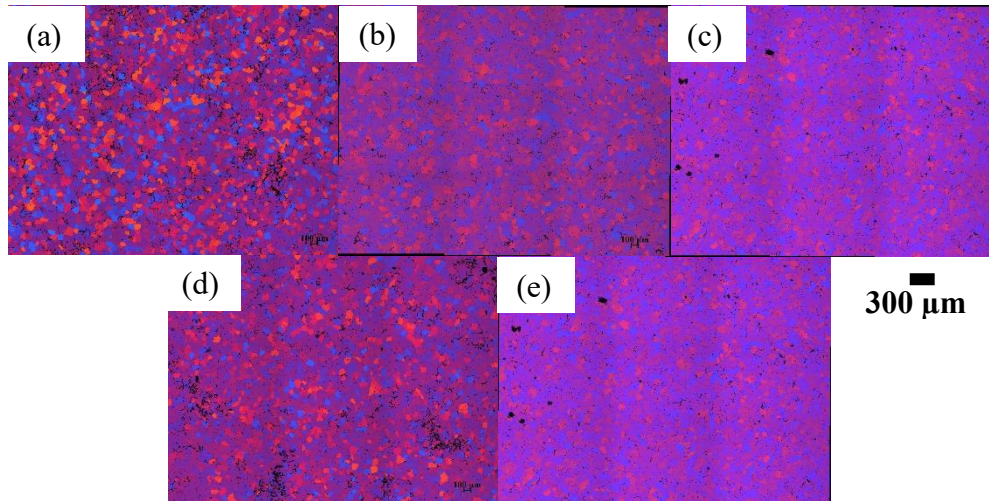


Table 7.12: Alloy 4 grain size summary.

Temper	T4	T6	T79	T76	T73
Area Fraction of Small Grains	1	1	1	1	1
Average Small ECD (μm)	51	67	61	63	51
95% Error (μm)	2.2	1.6	1.4	1.6	1.4
Area Fraction of Large Grains					
Average Large ECD (μm)					
95% Error (μm)					

Figure 7.21: Alloy 4 micrographs at 100x of (a) T4 (b) T6 (c) T79 (d) T76 (e) T73.

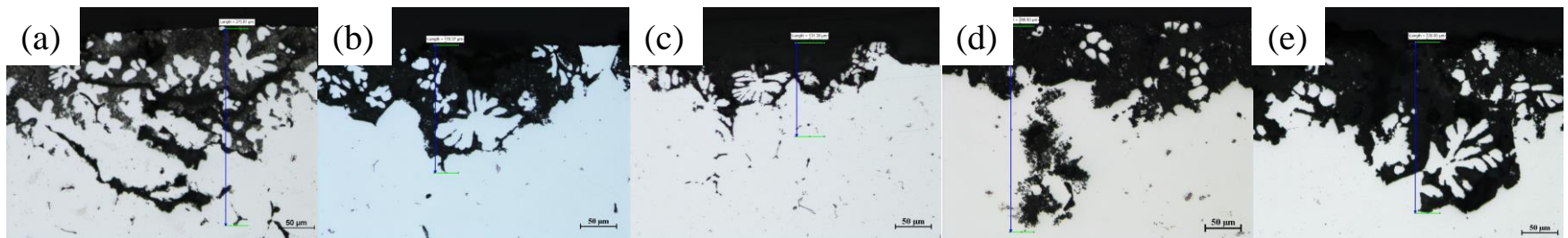


Figure 7.20: Alloy 4 cross-sections after 96 h immersion in EXCO solution at 200x (a) T4 (b) T6 (c) T79 (d) T76 (e) T73. Scale is 50 μm.

Chapter 7: Appendix

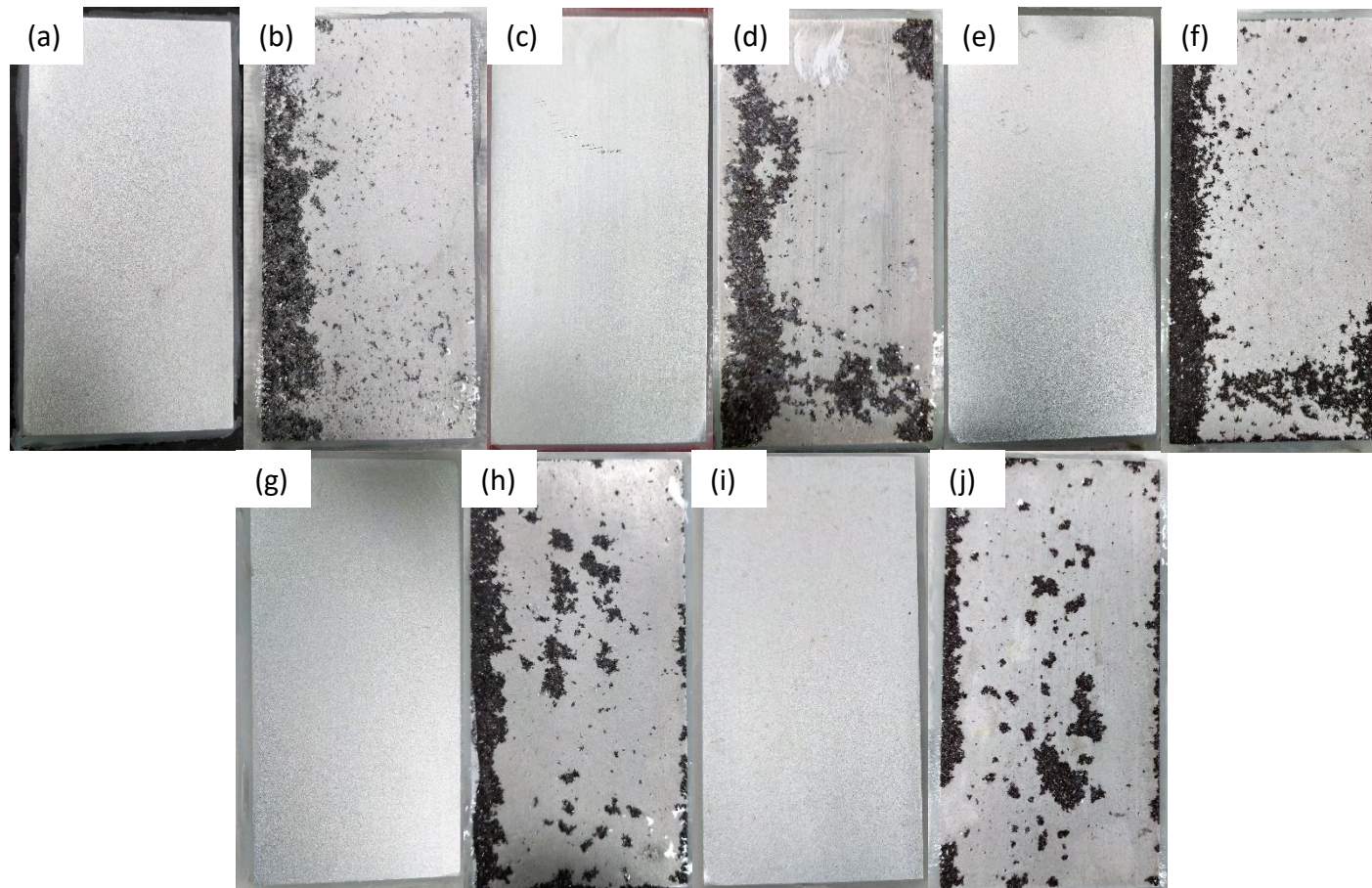


Figure 7.22: Alloy 4 images before and after immersion in modified EXCO solution (a-b) T4 (c-d) T6 (e-f) T79 (g-h) T76 (i-j) T73.

Chapter 7: Appendix

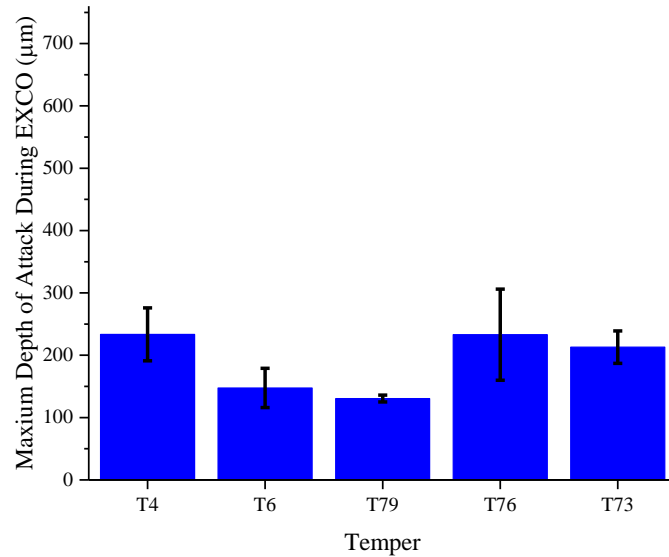


Figure 7.24: Alloy 4 maximum depth of penetration observed in cross-section after 96 h of immersion in modified EXCO solution.

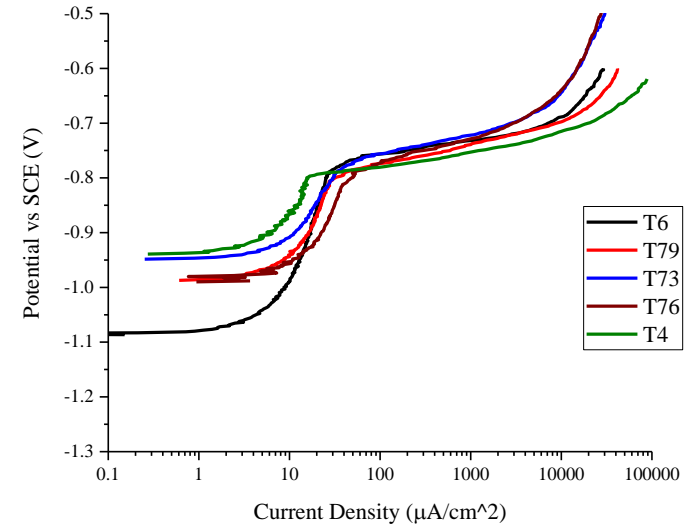


Figure 7.23: Alloy 4 potentiodynamic polarizations in deaerated 0.5M NaCl_(aq) solution.

Alloy 4 is a Cu-containing alloy with Zn/Mg ratio well above 2. In the T6 temper the hardness is relatively high, but it is highly responsive to ageing. Due to relatively high Ti content the grain size is uniform with a diameter of approximately 55 µm. The primary mode of corrosion is IDC and according to the maximum depth of attack during modified EXCO, it is uniform across all tempers. There exists no significant difference in the breakdown potential with ageing.

7.5.0 Alloy 5

Table 7.13: Alloy 5 compositions as determined by GDOES.

	Zn (wt%)	Mg (wt%)	Cu (wt%)	Ti (wt%)	Si (wt%)	Fe (wt%)	Mn (wt%)	Sn (wt%)	Al (wt%)	(Zn+Mg+Cu) (wt%)	Zn/Cu (wt%)	Zn/Mg (wt%)
TPGC	4.8	2	2.7	0.09	0.02	0.06	0.02	0.01	Bal.	9.5	1.78	2.4
Permanent Mould	5.4	2.2	3	0.05	0	0.08	0.02	0.02	Bal.	10.6	1.8	2.5

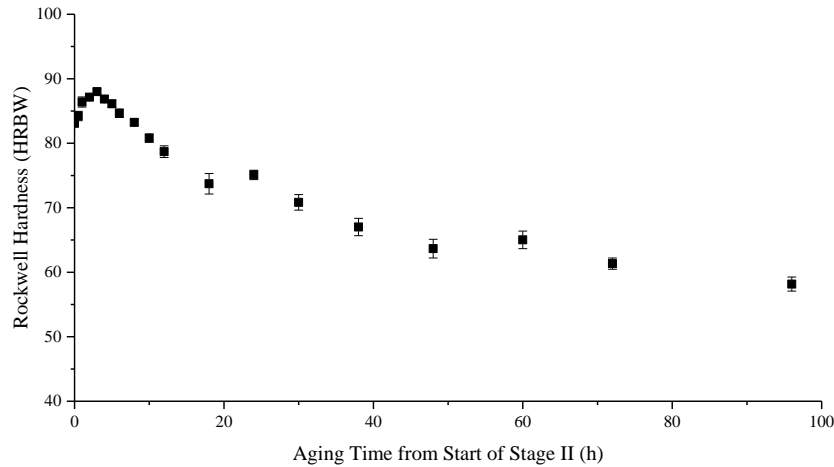


Figure 7.25: Ageing curve for alloy 5 at 185°C (HRBW).

Table 7.14: Rockwell hardness and associated ageing time for alloy 5.

Temper	Rockwell Hardness (HRBW)	Stage II Ageing Time (h)
T6	88	3
T79	79	12
T76	69	35
T73	60	73

Chapter 7: Appendix

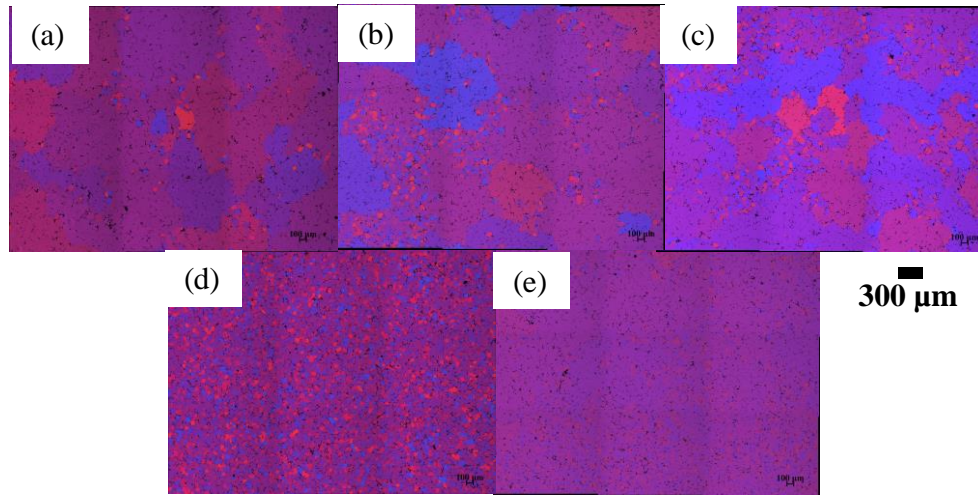


Table 7.15: Alloy 5 grain size summary.

Temper	T4	T6	T79	T76	T73
Area Fraction of Small Grains	0.04	0.2	0.33	0.03	0.62
Average Small ECD (μm)	51	48	44	43	48
95% Error (μm)	3	1.5	0.9	1.5	0.8
Area Fraction of Large Grains	0.96	0.8	0.67	0.97	0.38
Average Large ECD (μm)	611	320	243	772	195
95% Error (μm)	144	117	39	368	50

Figure 7.27: Alloy 5 micrographs at 100x of (a) T4 (b) T6 (c) T79 (d) T76 (e) T73.

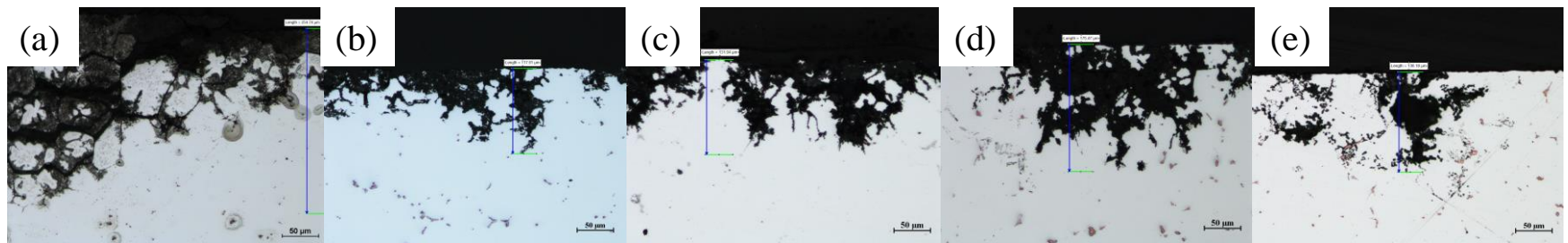


Figure 7.26: Alloy 5 cross-sections after 96 h immersion in EXCO solution at 200x (a) T4 (b) T6 (c) T79 (d) T76 (e) T73. Scale is 50μm.

Chapter 7: Appendix

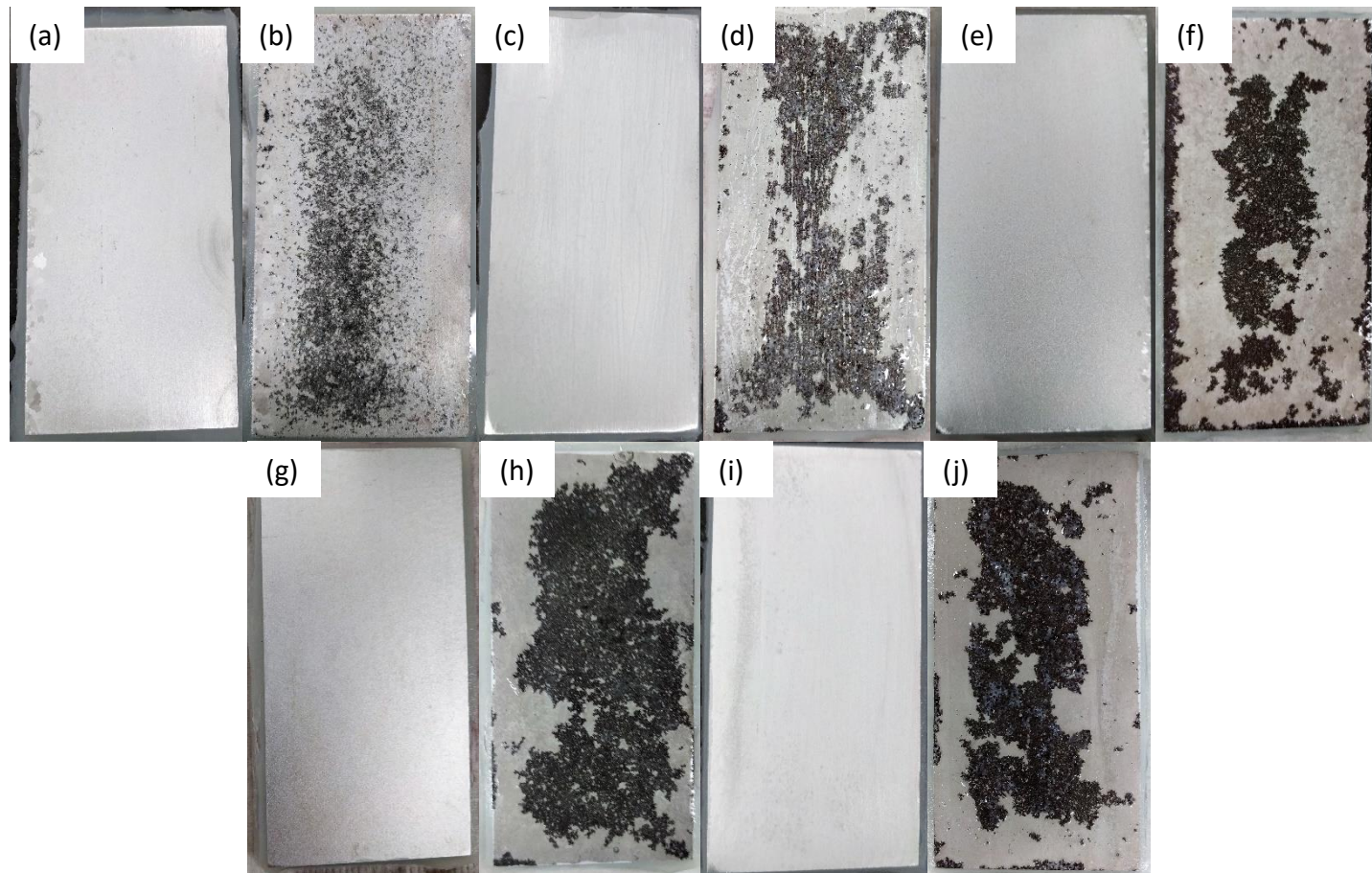


Figure 7.28: Alloy 5 images before and after immersion in modified EXCO solution (a-b) T4 (c-d) T6 (e-f) T79 (g-h) T76 (i-j) T73.

Chapter 7: Appendix

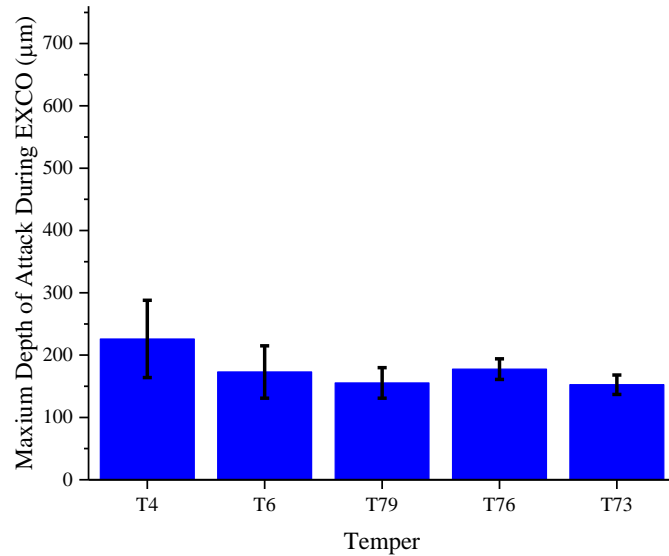


Figure 7.30: Alloy 5 maximum depth of penetration observed in cross-section after 96 h of immersion in modified EXCO solution.

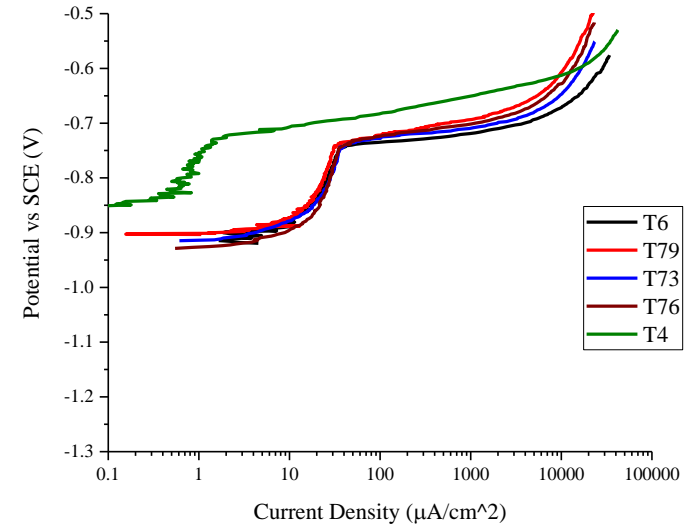


Figure 7.29: Alloy 5 potentiodynamic polarizations in deaerated 0.5M NaCl_(aq) solution.

Alloy 5 was a Cu-containing alloy with Zn/Mg ratio slightly above 2. In the T6 temper the hardness is relatively high and was highly responsive to ageing. Grain diameter had a bimodal distribution with the existence of small and large grains due to abnormal grain growth. The primary mode of corrosion was IDC and according to the maximum depth of attack during modified EXCO it is uniform across all tempers. There exists no significant difference in the breakdown potential with ageing, however the critical current density in the T4 condition is an order of magnitude less.

7.6.0 Alloy 6

Table 7.16: Alloy 6 compositions as determined by GDOES.

	Zn (wt%)	Mg (wt%)	Cu (wt%)	Ti (wt%)	Si (wt%)	Fe (wt%)	Mn (wt%)	Sn (wt%)	Al (wt%)	(Zn+Mg+Cu) (wt%)	Zn/Cu (wt%)	Zn/Mg (wt%)
TPGC	4.7	2.1	0.02	0.12	0.02	0.04	0.02	0.01	Bal.	6.82	235	2.2
Permanent Mould	5.0	2.1	0.02	0.12	0	0.06	0.02	0.04	Bal.	7.12	250	2.4

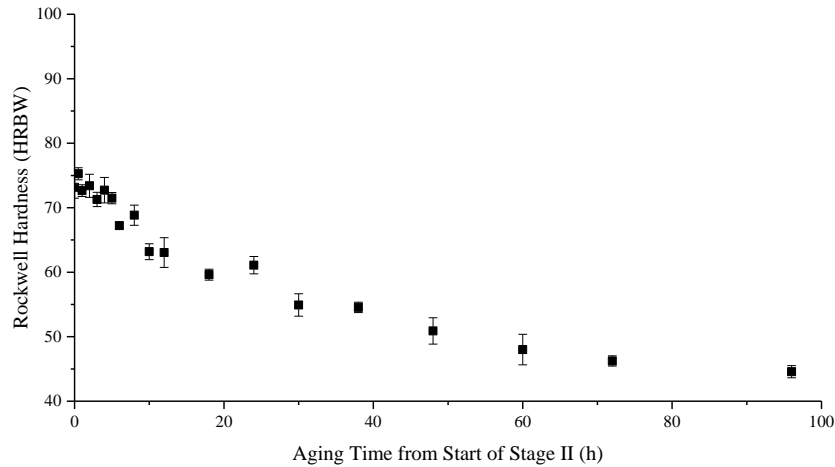


Figure 7.31: Ageing curve for alloy 6 at 185°C (HRBW).

Table 7.17: Rockwell hardness and associated ageing time for alloy 6.

Temper	Rockwell Hardness (HRBW)	Stage II Ageing Time (h)
T6	75	0.5
T79	65	7
T76	55	30
T73	46	61

Chapter 7: Appendix

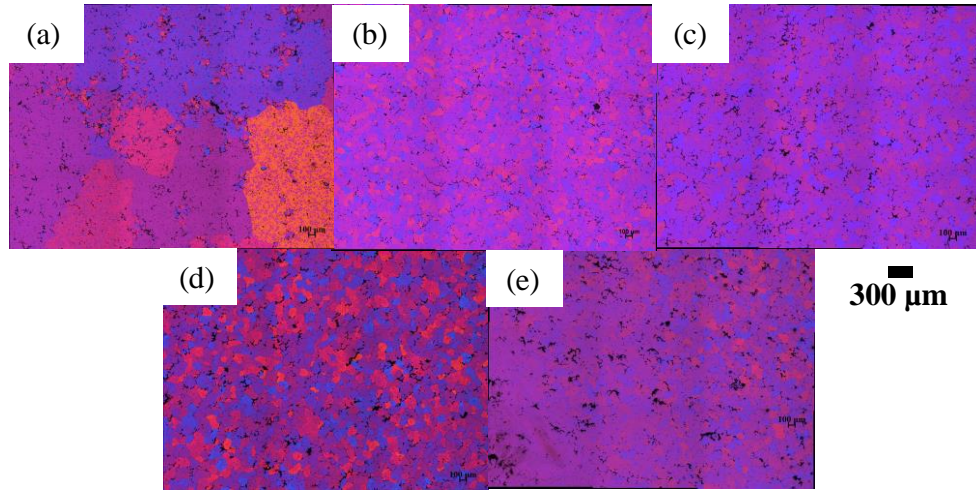


Table 7.18: Alloy 6 grain size summary.

Temper	T4	T6	T79	T76	T73
Area Fraction of Small Grains	1	1	1	1	1
Average Small ECD (μm)	51	79	95	104	67
95% Error (μm)	0.8	3.9	3.3	5.3	3.7
Area Fraction of Large Grains					
Average Large ECD (μm)					
95% Error (μm)					

Figure 7.33: Alloy 6 micrographs at 100x of (a) T4 (b) T6 (c) T79 (d) T76 (e) T73.

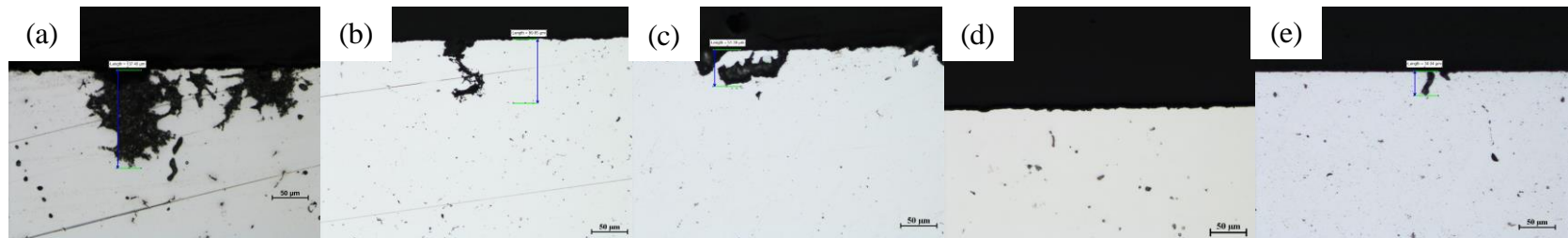


Figure 7.32: Alloy 6 cross-sections after 96 h immersion in EXCO solution at 200x (a) T4 (b) T6 (c) T79 (d) T76 (e) T73. Scale is 50 μm.

Chapter 7: Appendix

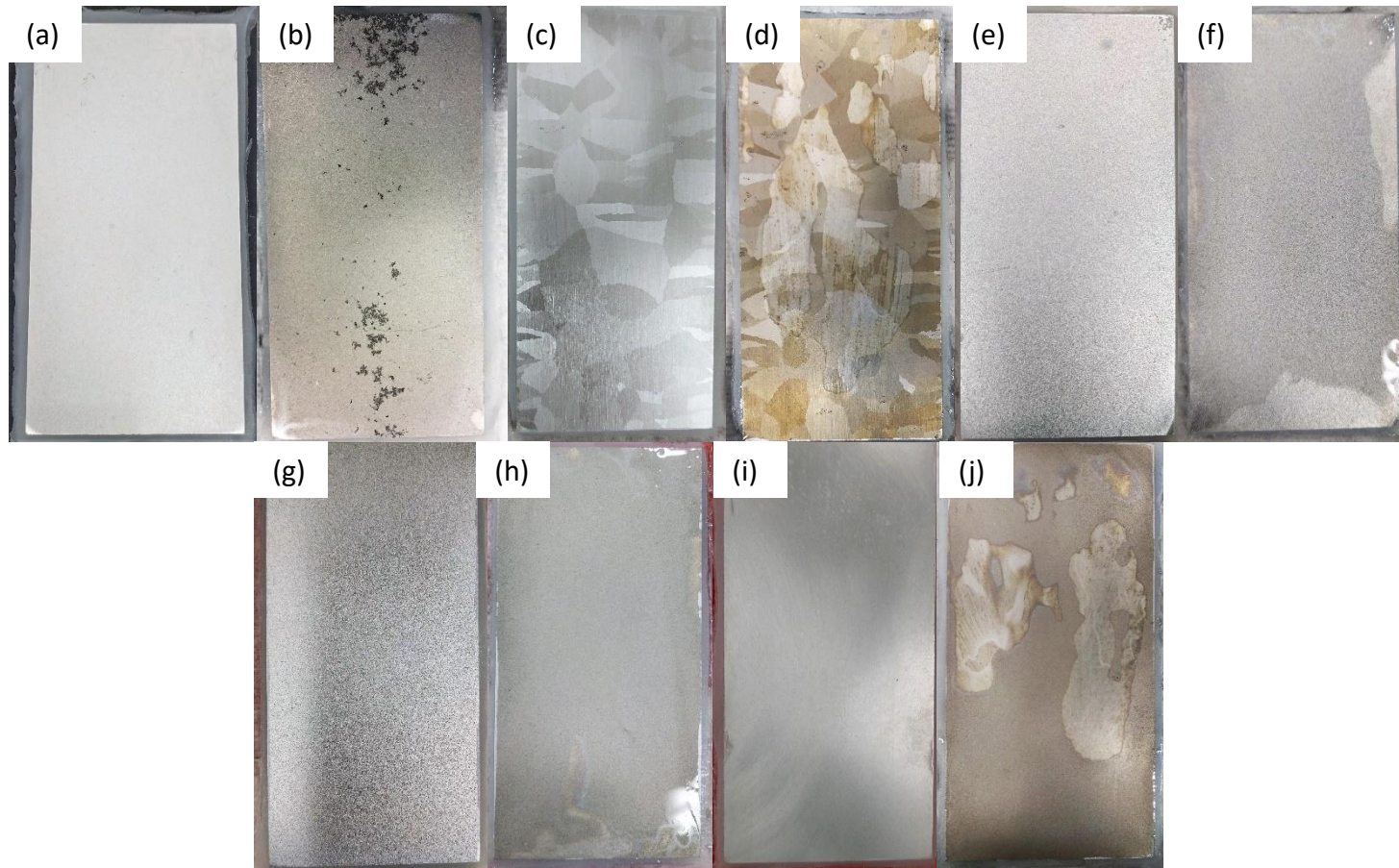


Figure 7.34: Alloy 6 images before and after immersion in modified EXCO solution (a-b) T4 (c-d) T6 (e-f) T79 (g-h) T76 (i-j) T73.

Chapter 7: Appendix

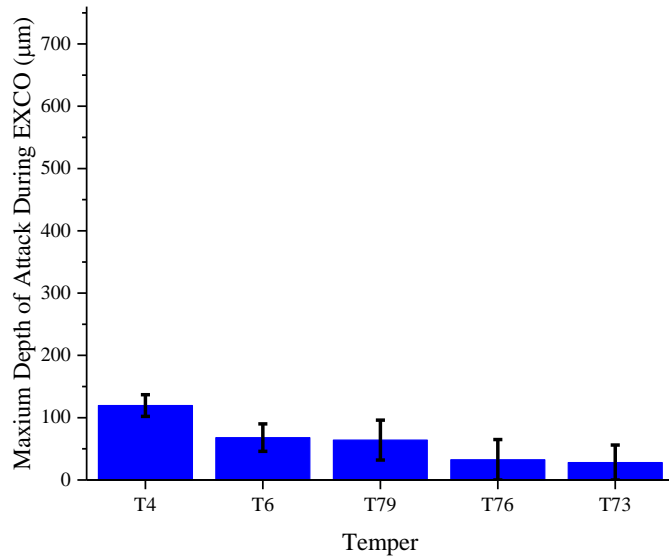


Figure 7.36: Alloy 6 maximum depth of penetration observed in cross-section after 96 h of immersion in modified EXCO solution.

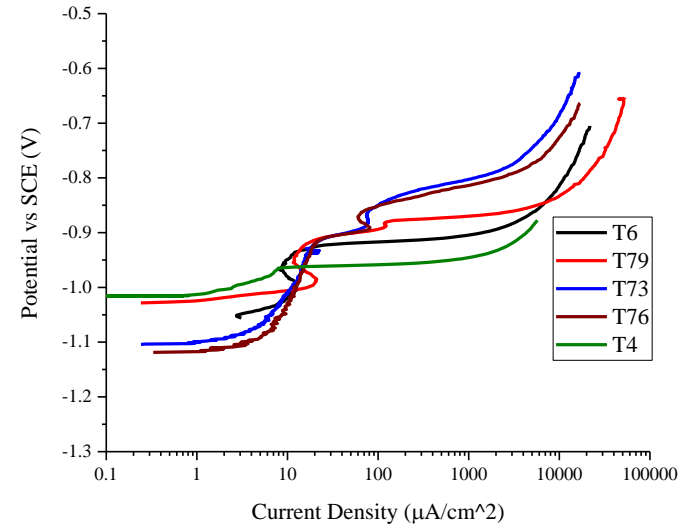


Figure 7.35: Alloy 6 potentiodynamic polarizations in deaerated 0.5M NaCl_(aq) solution.

Alloy 6 is a Cu-lean alloy with a Zn/Mg ratio slightly above 2. At the T6 temper the hardness is relatively high for a low copper alloy, but with a strong ageing response the hardness quickly drops with continued ageing. The microstructure shows a uniform distribution. The maximum depth during modified EXCO is lower than Cu-containing alloys and is uniform across the tempers. Any corrosion that does form further than pitting shows characteristics of IDC. The breakdown potentials show many interesting features that are explained in the discussion section. T4 shows a typical single breakdown, T6 and T79 show an active passive region followed by a breakdown, and T76 and T73 show a double breakdown.

7.7.0 Alloy 7

Table 7.19: Alloy 7 compositions as determined by GDOES.

	Zn (wt%)	Mg (wt%)	Cu (wt%)	Ti (wt%)	Si (wt%)	Fe (wt%)	Mn (wt%)	Sn (wt%)	Al (wt%)	(Zn+Mg+Cu) (wt%)	Zn/Cu (wt%)	Zn/Mg (wt%)
TPGC	6	1.4	2.1	0.57	0.01	0.05	0.02	0.01	Bal.	9.5	2.86	4.3
Permanent Mould	7	1.7	3	0.15	0	0.08	0.02	0.02	Bal.	11.7	2.33	4.1

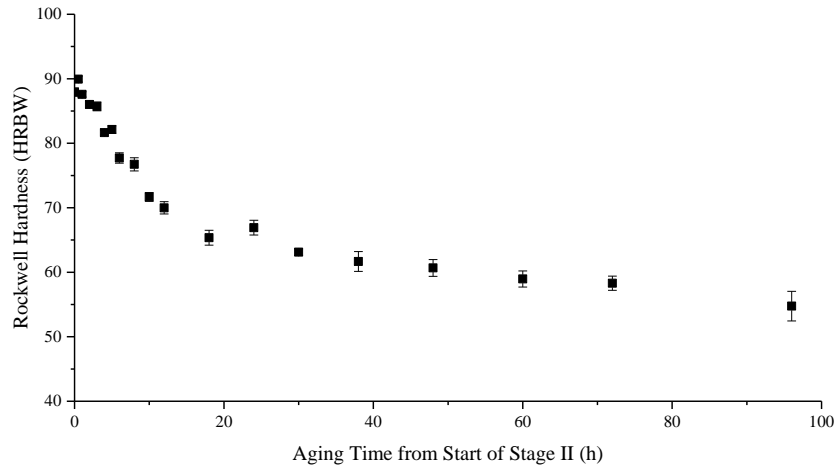


Figure 7.37: Ageing curve for alloy 7 at 185°C (HRBW).

Table 7.20: Rockwell hardness and associated ageing time for alloy 7.

Temper	Rockwell Hardness (HRBW)	Stage II Ageing Time (h)
T6	91	0.5
T79	80	5
T76	68	22
T73	59	48

Chapter 7: Appendix

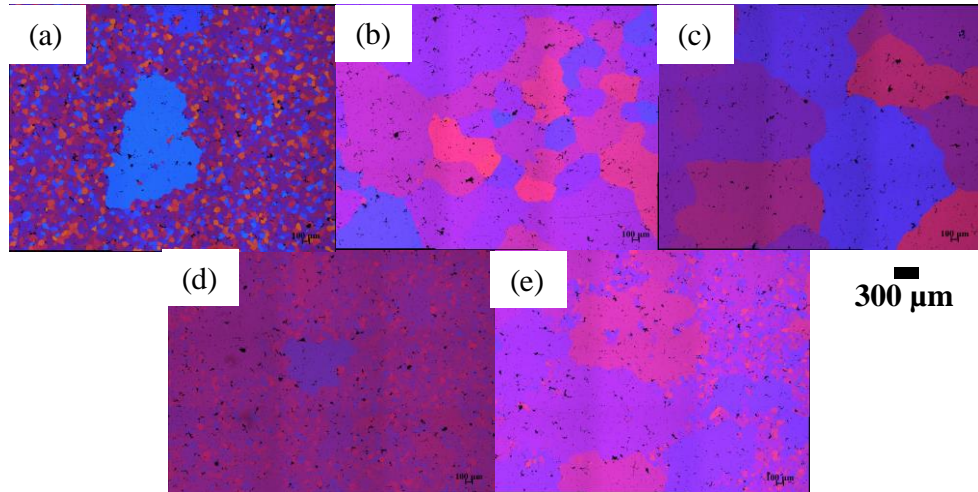


Table 7.21: Alloy 7 grain size summary.

Temper	T4	T6	T79	T76	T73
Area Fraction of Small Grains	0.48			0.31	0.56
Average Small ECD (μm)	57			53	37
95% Error (μm)	1			1	2.2
Area Fraction of Large Grains	0.52	1	1	0.69	0.44
Average Large ECD (μm)	169	434	512	208	194
95% Error (μm)	15	140	250	30	73

Figure 7.39: Alloy 7 micrographs at 100x of (a) T4 (b) T6 (c) T79 (d) T76 (e) T73.

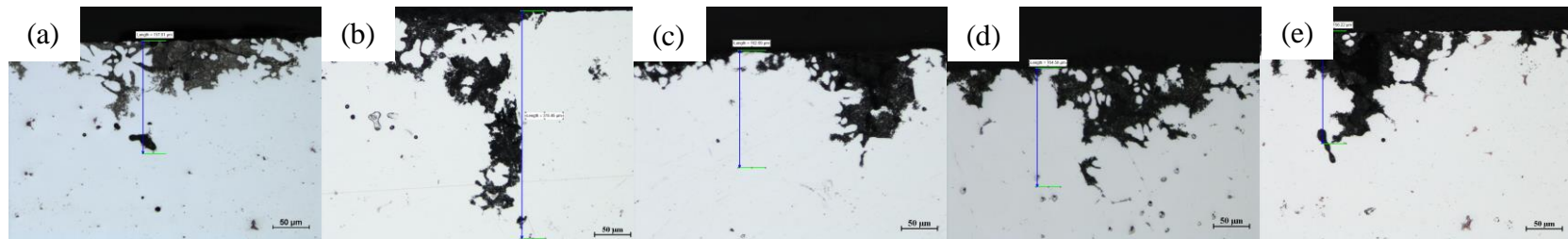


Figure 7.38: Alloy 7 cross-sections after 96 h immersion in EXCO solution at 200x (a) T4 (b) T6 (c) T79 (d) T76 (e) T73. Scale is 50 μm.

Chapter 7: Appendix

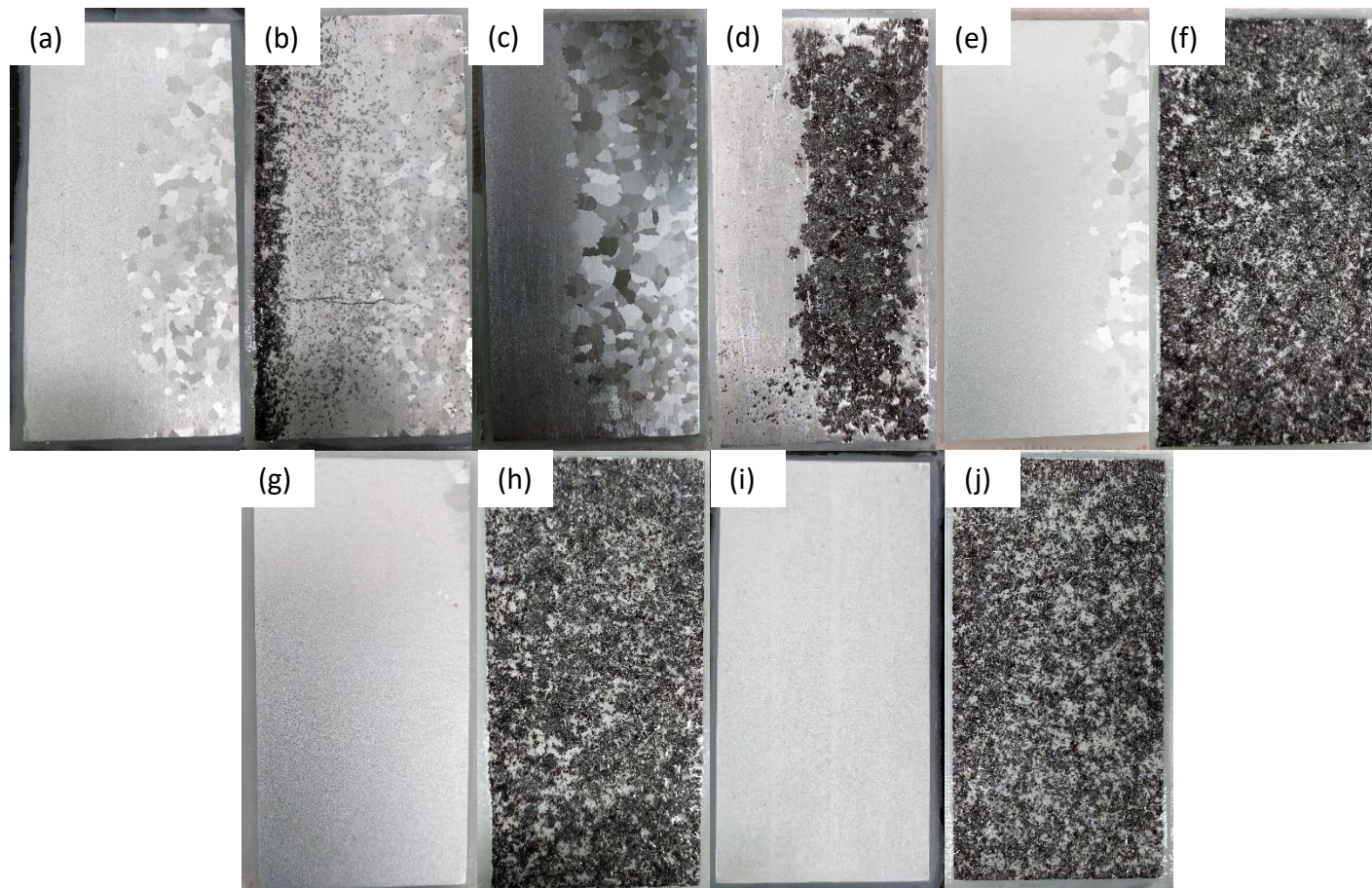


Figure 7.40: Alloy 7 images before and after immersion in modified EXCO solution (a-b) T4 (c-d) T6 (e-f) T79 (g-h) T76 (i-j) T73.

Chapter 7: Appendix

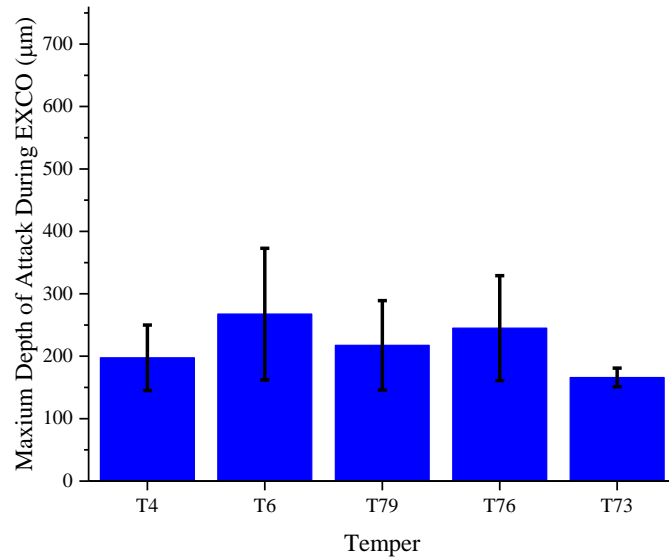


Figure 7.42: Alloy 7 maximum depth of penetration observed in cross-section after 96 h of immersion in modified EXCO solution.

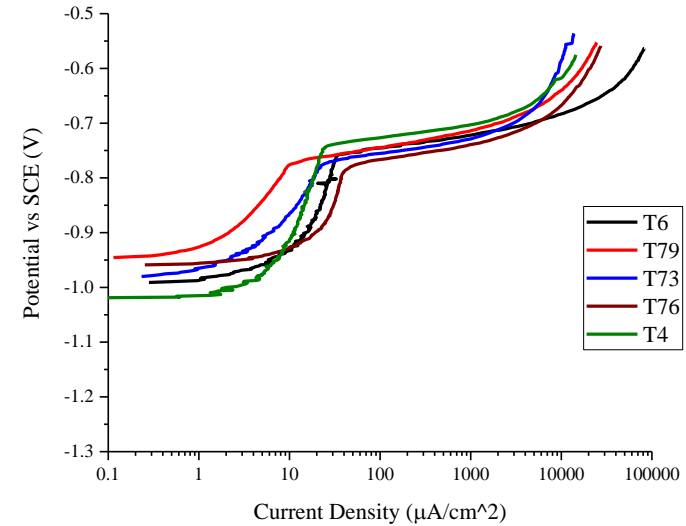


Figure 7.41: Alloy 7 potentiodynamic polarizations in deaerated 0.5M NaCl_(aq) solution.

Alloy 7 has a relatively high Zn/Mg ratio with a medium amount of Cu. The ageing response of alloy 7 is very high showing a large decrease in strength after T6. Due to a mid level Ti content the grain diameter is bimodal showing signs of abnormal grain growth. The main mechanism of attack is IDC as shown in the modified EXCO cross-sections, but there exists no significant difference in maximum depth of attack across the tempers. As well no significant difference exists in the breakdown potential of alloy 7 as ageing progresses from T4 to T73.

7.8.0 Alloy 8

Table 7.22: Alloy 8 compositions as determined by GDOES.

	Zn (wt%)	Mg (wt%)	Cu (wt%)	Ti (wt%)	Si (wt%)	Fe (wt%)	Mn (wt%)	Sn (wt%)	Al (wt%)	(Zn+Mg+Cu) (wt%)	Zn/Cu (wt%)	Zn/Mg (wt%)
TPGC	6	1.8	0.02	0.26	0.02	0.05	0.02	0.01	Bal.	7.82	300	3.3
Permanent Mould	6.9	1.9	0.16	0.08	0	0.06	0.04	0.07	Bal.	9	43	3.8

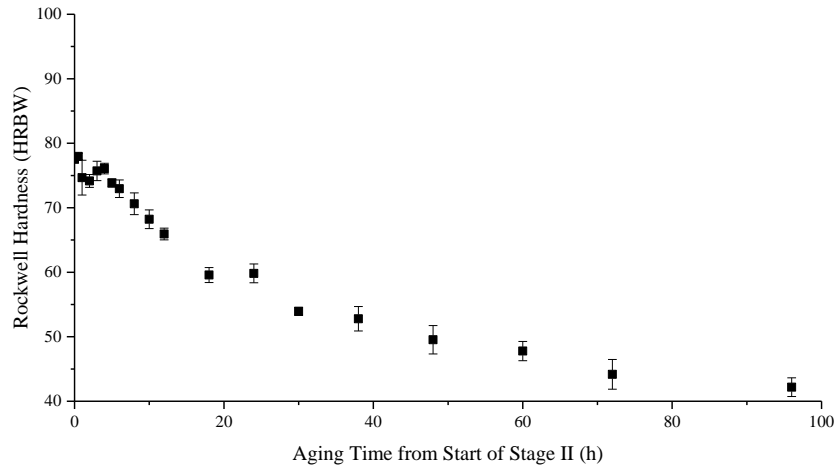


Figure 7.43: Ageing curve for alloy 8 at 185°C (HRBW).

Table 7.23: Rockwell hardness and associated ageing time for alloy 8.

Temper	Rockwell Hardness (HRBW)	Stage II Ageing Time (h)
T6	78	0.5
T79	69	7
T76	56	29
T73	46	66

Chapter 7: Appendix

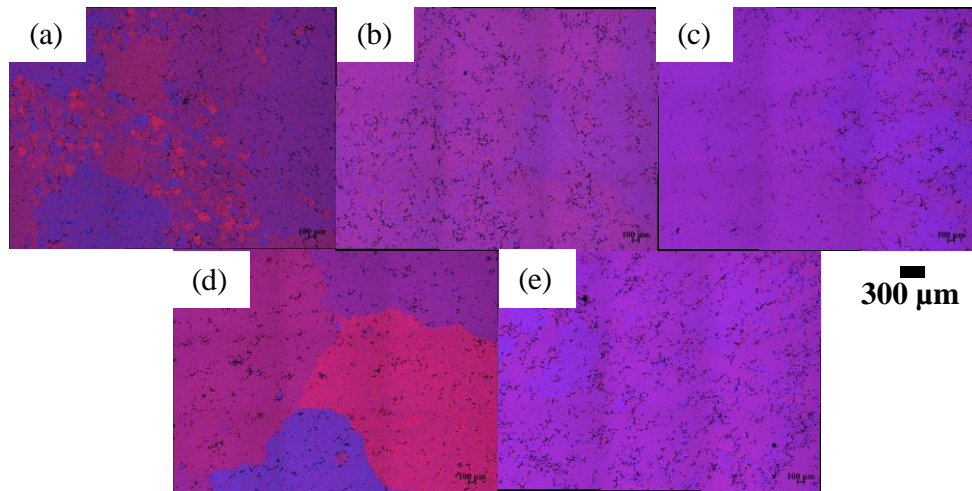


Table 7.24: Alloy 8 grain size summary.

Temper	T4	T6	T79	T76	T73
Area Fraction of Small Grains	0.22	0.13	0.56	0.1	0.2
Average Small ECD (μm)	65	52	54	95	47
95% Error (μm)	1.6	1.5	1.3	24	1
Area Fraction of Large Grains	0.78	0.87	0.44	0.99	0.8
Average Large ECD (μm)	193	255	294	2119	301
95% Error (μm)	52	84	97	100	77

Figure 7.45: Alloy 8 micrographs at 100x of (a) T4 (b) T6 (c) T79 (d) T76 (e) T73.

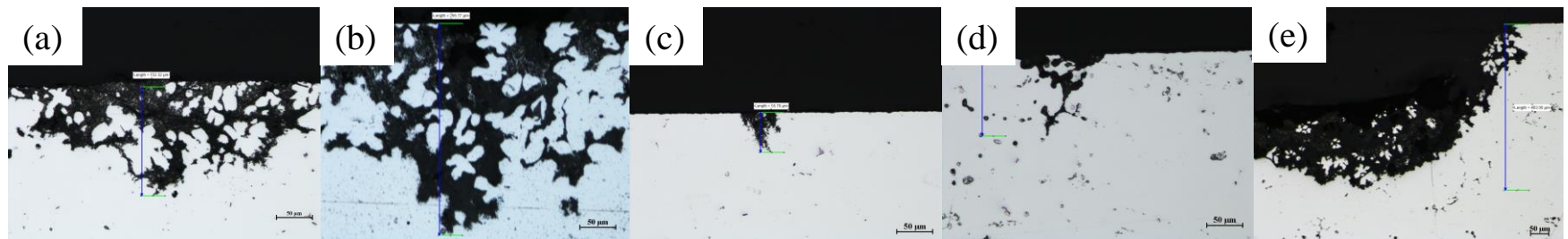


Figure 7.44: Alloy 8 cross-sections after 96 h immersion in EXCO solution at 200x (a) T4 (b) T6 (c) T79 (d) T76 (e) T73. Scale is 50 μm.*

*Note (e) was taken at 100x rather than the standard 200x

Chapter 7: Appendix

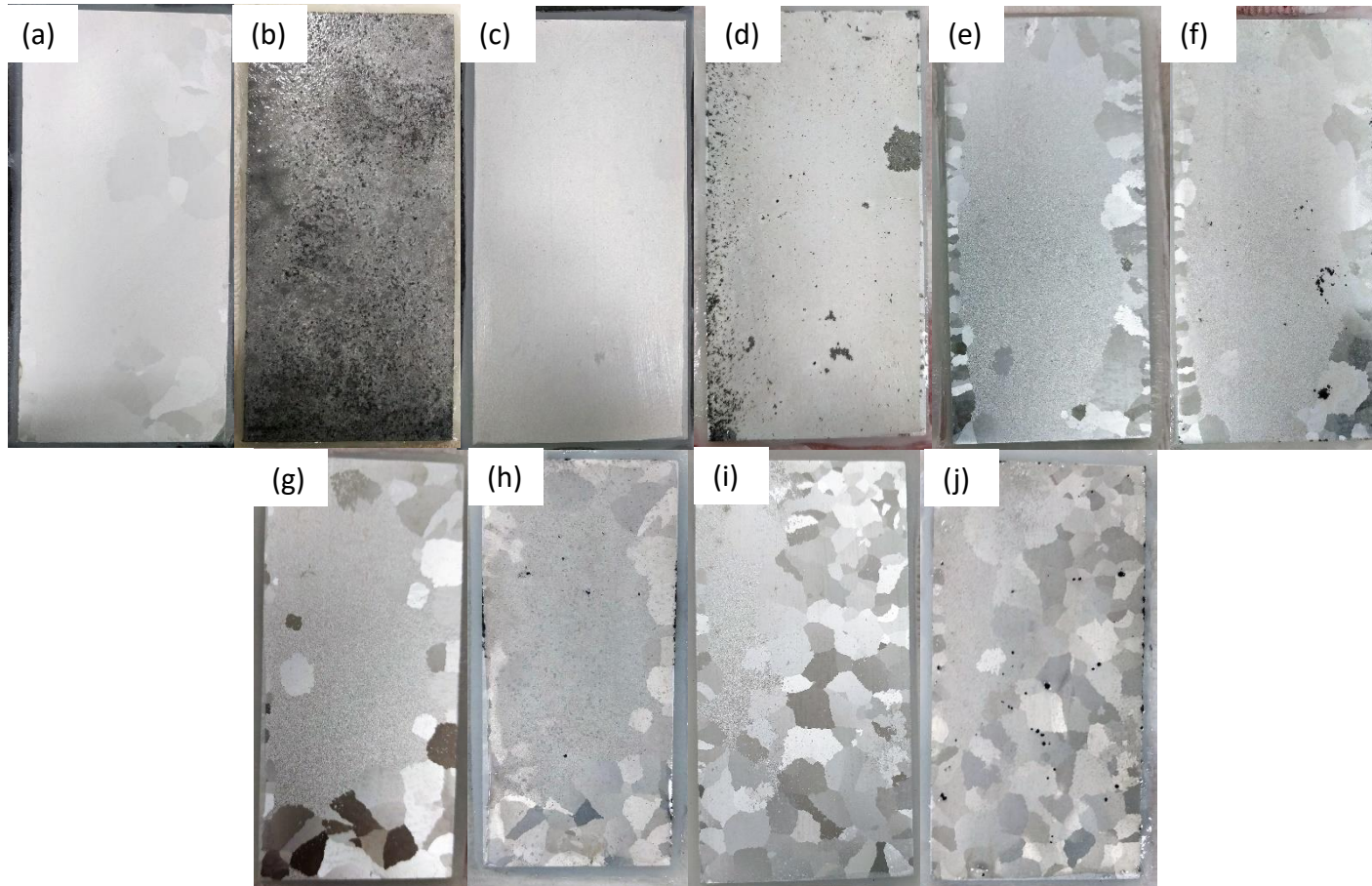


Figure 7.46: Alloy 8 images before and after immersion in modified EXCO solution (a-b) T4 (c-d) T6 (e-f) T79 (g-h) T76 (i-j) T73.

Chapter 7: Appendix

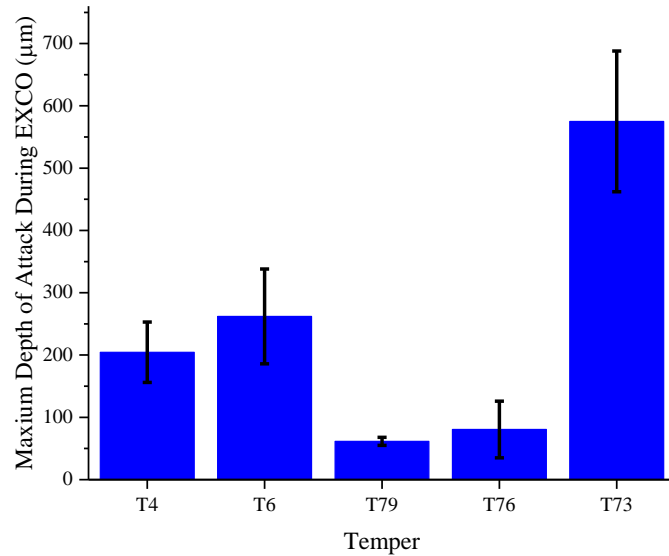


Figure 7.48: Alloy 8 maximum depth of penetration observed in cross-section after 96 h of immersion in modified EXCO solution.

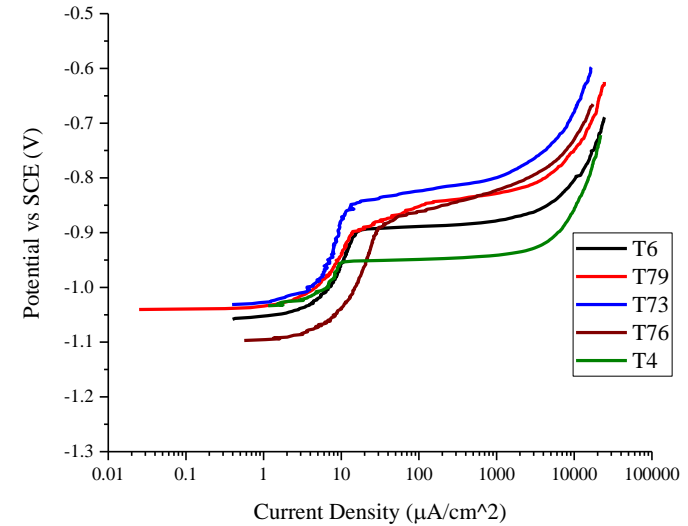


Figure 7.47: Alloy 8 potentiodynamic polarizations in deaerated 0.5M NaCl_(aq) solution.

Alloy 8 is the last of the Cu-free alloys and maintains a relatively high Zn/Mg ratio leading to a strong response to ageing as seen in the ageing curves. A low Ti content in the permanent mould leads to a bimodal distribution of grain diameters. Of the Cu-free alloys tested alloy 8 has the highest depth of penetration during the modified EXCO test with T73 having the most severe attack. The attack is primarily IDC, but large pits in the T73 condition are the cause of the significant damage. The breakdown potential increases with ageing from T4 to T73 due to Zn-depletion in the matrix.

7.9.0 Alloy 9

Table 7.25: Alloy 9 compositions as determined by GDOES.

	Zn (wt%)	Mg (wt%)	Cu (wt%)	Ti (wt%)	Si (wt%)	Fe (wt%)	Mn (wt%)	Sn (wt%)	Al (wt%)	(Zn+Mg+Cu) (wt%)	Zn/Cu (wt%)	Zn/Mg (wt%)
TPGC	6.4	2.3	1.3	0.06	0.02	0.05	0.02	0.01	Bal.	10	4.92	2.8
Permanent Mould	6.5	2.4	1.3	0.04	0	0.06	0.02	0.02	Bal.	10.2	5	2.7

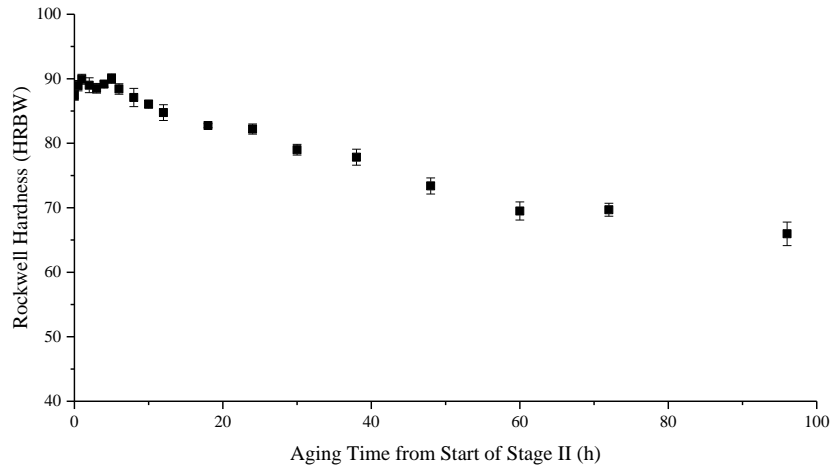


Figure 7.49: Ageing curve for alloy 9 at 185°C (HRBW).

Table 7.26: Rockwell hardness and associated ageing time for alloy 9.

Temper	Rockwell Hardness (HRBW)	Stage II Ageing Time (h)
T6	90	5
T79	83	17
T76	76	45
T73	69	60

Chapter 7: Appendix

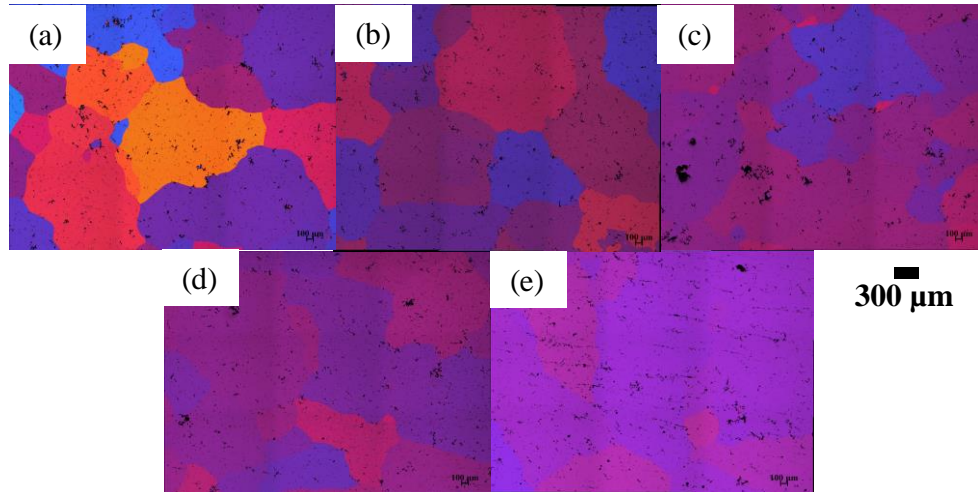


Table 7.27: Alloy 9 grain size summary.

Temper	T4	T6	T79	T76	T73
Area Fraction of Small Grains					
Average Small ECD (μm)					
95% Error (μm)					
Area Fraction of Large Grains	1	1	1	1	1
Average Large ECD (μm)	692	726	555	780	719
95% Error (μm)	260	319	201	170	360

Figure 7.51: Alloy 9 micrographs at 100x of (a) T4 (b) T6 (c) T79 (d) T76 (e) T73.

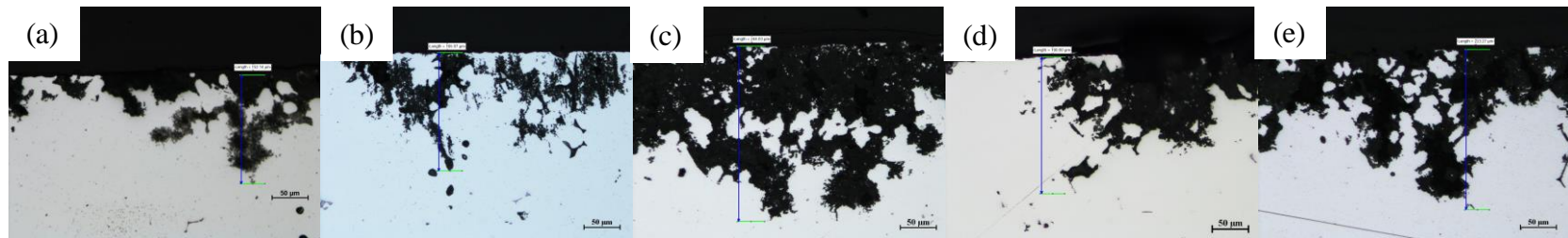


Figure 7.50: Alloy 9 cross-sections after 96 h immersion in EXCO solution at 200x (a) T4 (b) T6 (c) T79 (d) T76 (e) T73. Scale is 50 μm.

Chapter 7: Appendix

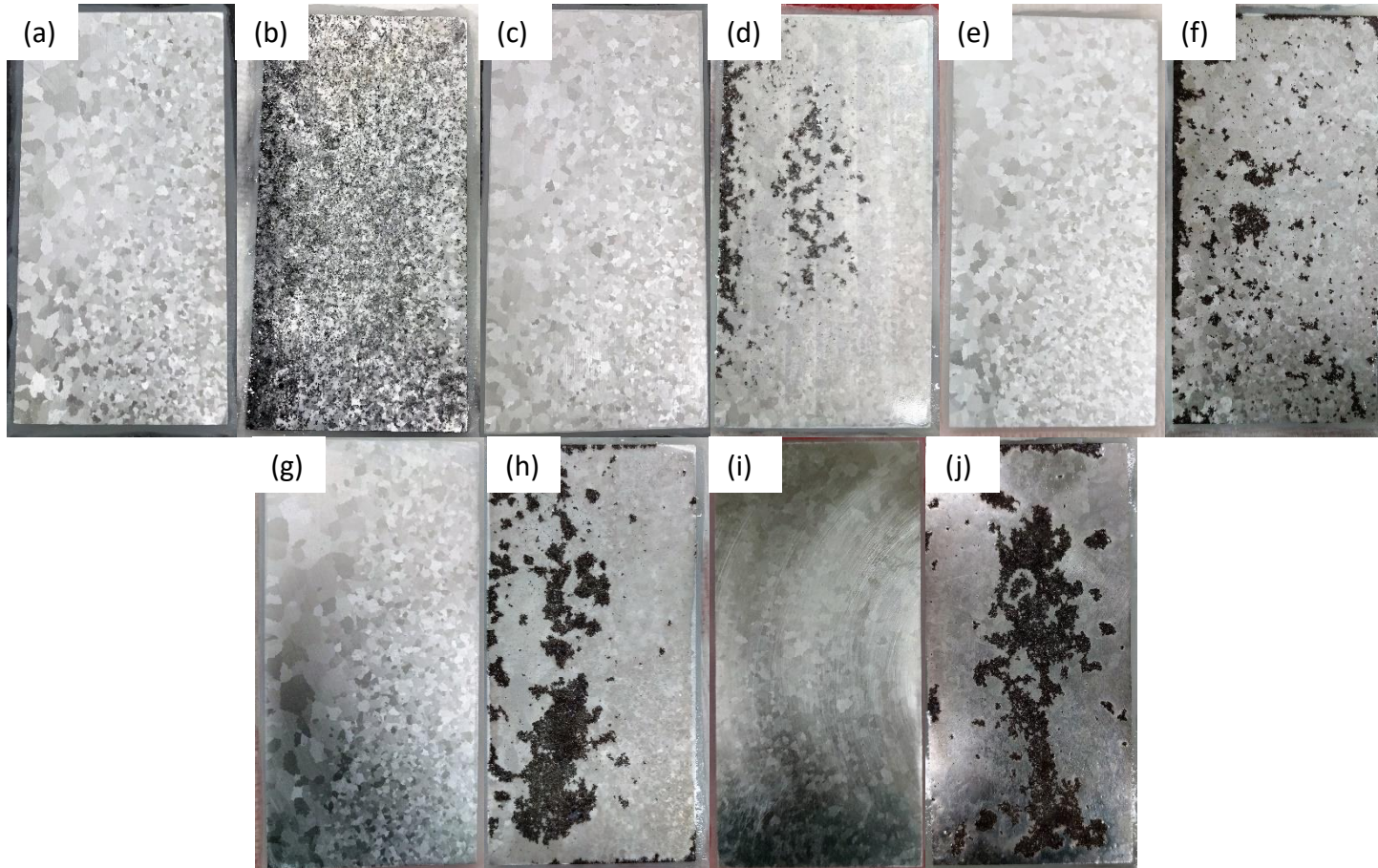


Figure 7.52: Alloy 9 images before and after immersion in modified EXCO solution (a-b) T4 (c-d) T6 (e-f) T79 (g-h) T76 (i-j) T73.

Chapter 7: Appendix

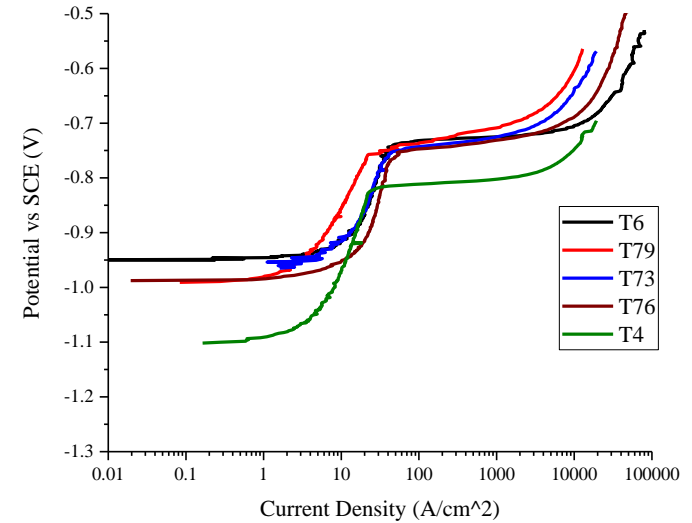
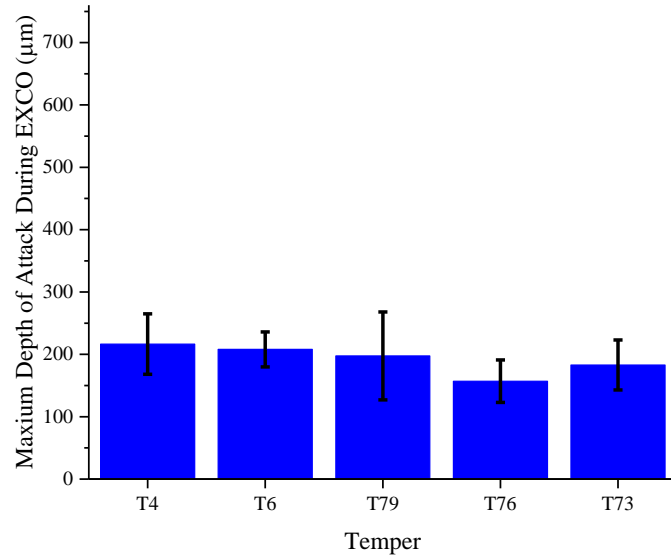


Figure 7.54: Alloy 9 maximum depth of penetration observed in cross-section after 96 h of immersion in modified EXCO solution.

Figure 7.53: Alloy 9 potentiodynamic polarizations in deaerated 0.5M NaCl_(aq) solution.

Alloy 9 is a Cu-containing alloy with a Zn/Mg ratio just above 2 and a Zn/Cu ratio of approximately 5. It has high hardness and a limited ageing response for alloys with Zn/Mg ratios above 2. The grain diameter is uniform, but with just large grains approximately 600 µm in diameter. The primary mechanism of corrosion is IDC, but the maximum depth of attack recorded in cross-section during the modified EXC test is uniform across all tempers. The breakdown potential increases from T4 to T6, but it stays relatively constant from T6 to T73. It is the only Cu-containing alloy with a significant increase from T4 to T6 which is attributed to the high Zn/Cu ratio.

7.10.0 Validation Alloy

Table 7.28: Validation alloy compositions as determined by GDOES.

	Zn (wt%)	Mg (wt%)	Cu (wt%)	Ti (wt%)	Si (wt%)	Fe (wt%)	Mn (wt%)	Sn (wt%)	Al (wt%)	(Zn+Mg+Cu) (wt%)	Zn/Cu (wt%)	Zn/Mg (wt%)
TPGC	6	1.6	2.5	0.32	0.03	0.09	0.02	0.02	Bal.	10.1	2.4	3.8
Permanent Mould	5.9	1.6	2.7	0.2	0	0.1	0.02	0.02	Bal.	10.2	2.19	3.7

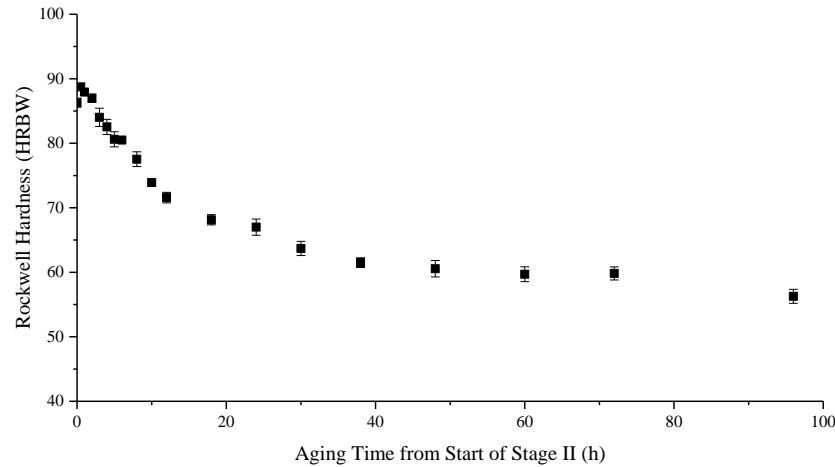


Figure 7.55: Ageing curve for the validation alloy at 185°C (HRBW).

Table 7.29: Rockwell hardness and associated ageing time for the validation alloy.

Temper	Rockwell Hardness (HRBW)	Stage II Ageing Time (h)
T6	89	0.5
T79	79	6
T76	70	14
T73	61	38

Chapter 7: Appendix

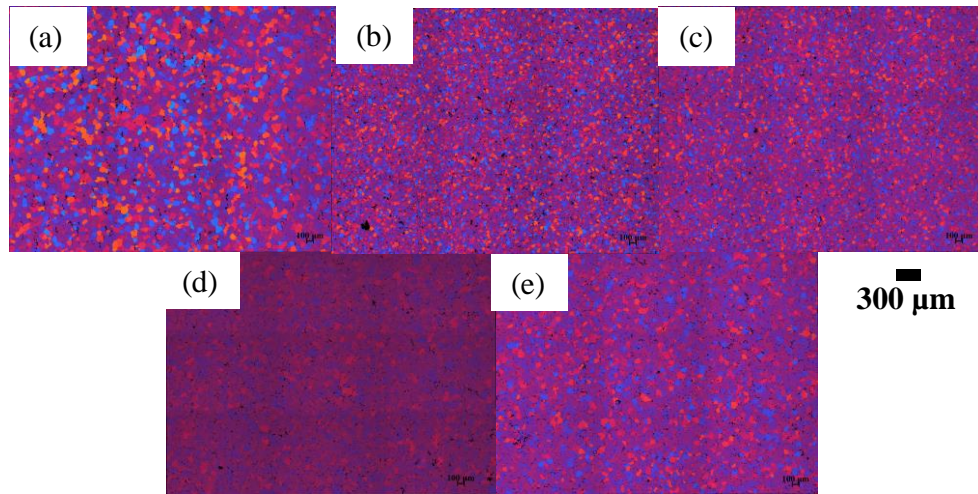


Figure 7.57: Validation alloy micrographs at 100x of (a) T4 (b) T6 (c) T79 (d) T76 (e) T73.

Table 7.30: Validation alloy grain size summary.

Temper	T4	T6	T79	T76	T73
Area Fraction of Small Grains	1	1	1	1	1
Average Small ECD (μm)	71	37	43.7	59	63.9
95% Error (μm)	1.7	0.4	0.59	5	1.7
Area Fraction of Large Grains					
Average Large ECD (μm)					
95% Error (μm)					

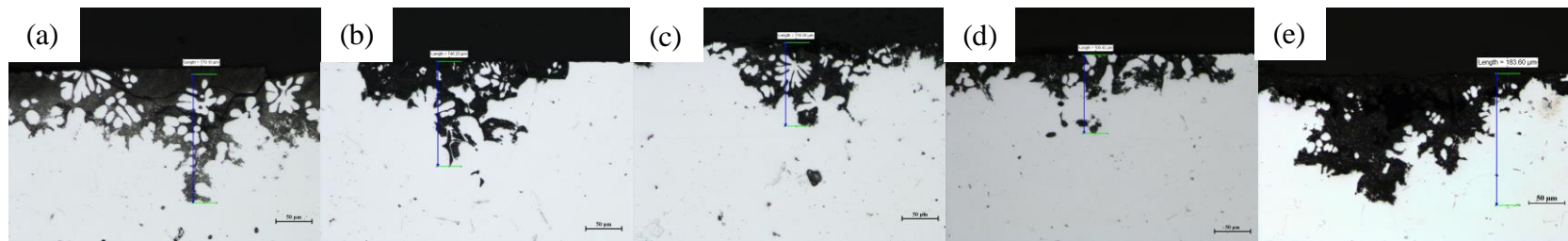


Figure 7.56: Validation alloy cross-sections after 96 h immersion in EXCO solution at 200x (a) T4 (b) T6 (c) T79 (d) T76 (e) T73. Scale is 50 μm.

Chapter 7: Appendix

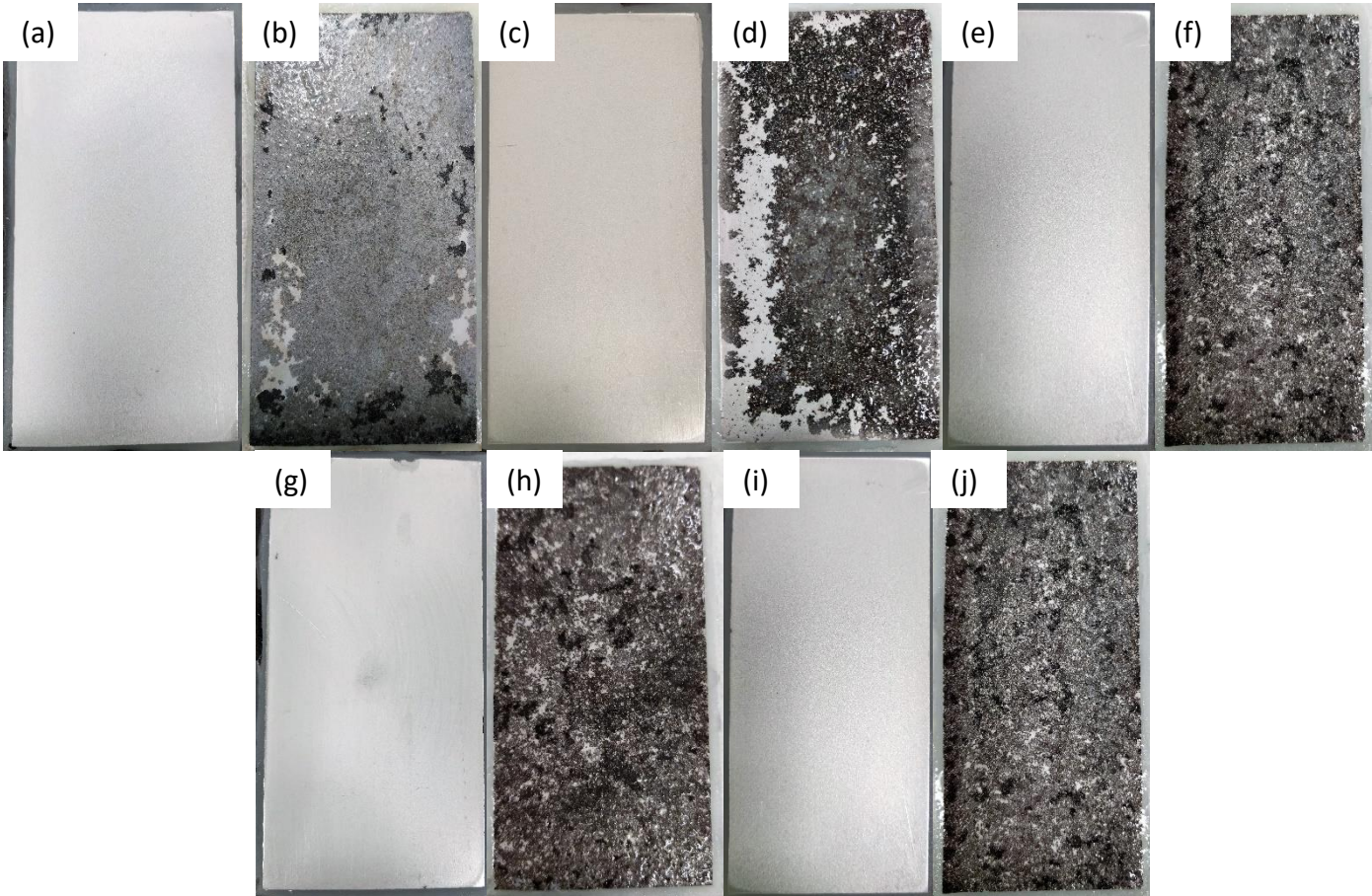


Figure 7.58: Validation alloy images before and after immersion in modified EXCO solution (a-b) T4 (c-d) T6 (e-f) T79 (g-h) T76 (i-j) T73.

Chapter 7: Appendix

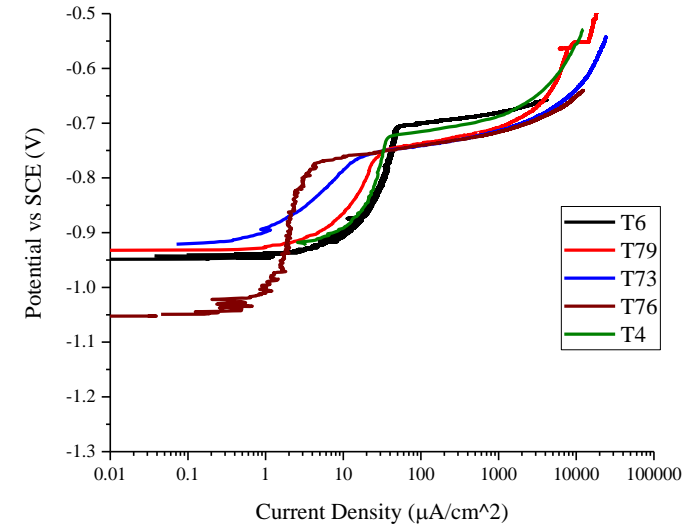
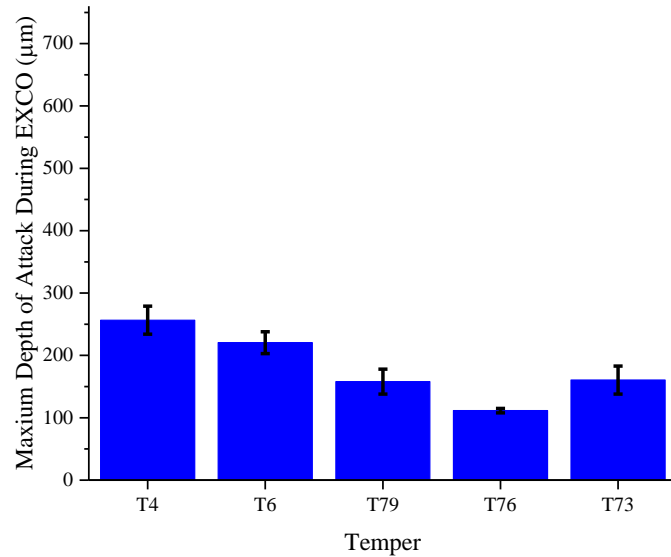


Figure 7.60: Validation alloy maximum depth of penetration observed in cross-section after 96 h of immersion in modified EXCO solution.

Figure 7.59: Validation alloy potentiodynamic polarizations in deaerated 0.5M NaCl_(aq) solution.

The validation alloy is a high copper and high Zn/Mg ratio alloy with high hardness and a strong ageing response. The grain size is uniform with a grain size of approximately 50µm for all tempers. The primary mode of corrosion is IDC with very little change in maximum depth of attack during the modified EXCO test. The breakdown potentials are relatively uniform across all tempers. T76 has a critical current density that is an order of magnitude less than the other tempers.

References

References

- [1] Ducker Worldwide, “Aluminum Content in Cars - Summary Report,” 2016.
- [2] S. Reza Ghiaasiaan, “Controlled Diffusion Solidification (CDS) of Al₃Zn₃Mg₃Cu (7050): Microstructure, heat treatment and mechanical properties,” McMaster University, 2014.
- [3] A. E. Hughes, N. Birbilis, J. M. C. Mol, S. J. Garcia, X. Zhou, and G. E. Thompson, “High Strength Al-Alloys: Microstructure Corrosion and Principles of Protection,” in *Recent Trends in Processing and Degredation of Aluminum Alloys*, Z. Ahmad, Ed. InTech, 2011, pp. 223–262.
- [4] D. A. Porter, K. E. Easterling, and M. Y. Sherif, *Phase Transformations in Metals and Alloys*, Third Edit. CRC Press, 1981.
- [5] W. X. Shu *et al.*, “Tailored Mg and Cu contents affecting the microstructures and mechanical properties of high-strength Al-Zn-Mg-Cu alloys,” *Mater. Sci. Eng. A*, vol. 657, pp. 269–283, 2016.
- [6] J. G. Kaufman, “Understanding Wrought and Cast Aluminum Alloys Designations,” in *Introduction to Aluminum Alloys and Tempers*, ASM International, 2000, pp. 23–37.
- [7] N. Birbilis and R. G. Buchheit, “Electrochemical Characteristics of Intermetallic Phases in Aluminum Alloys An Experimental Survey and Discussion,” *J. Electrochem. Soc.*, vol. 152, no. 4, pp. B140–B151, 2005.
- [8] N. Iqbal, N. H. van Dijk, T. Hansen, L. Katgerman, and G. J. Kearley, “The role of

References

- solute titanium and TiB₂ particles in the liquid - Solid phase transformation of aluminum alloys,” *Mater. Sci. Eng. A*, vol. 386, no. 1–2, pp. 20–26, 2004.
- [9] Aluminum Association, *ANSI H35.1: American National Standard Alloy and Temper Designation Systems for Aluminum*. 1990.
- [10] J. Weritz, L. Bulookbashi, and F. Licar, “The Aluminum Association Alloy and Temper System.” The Aluminum Association, 2016.
- [11] X. Zeng, C. Ferguson, K. Sadayappan, and S. Shankar, “Effect of Titanium levels on the Hot Tearing Sensitivity and Abnormal Grain Growth After T4 Heat Treatment of Al-Zn-Mg-Cu Alloys,” in *Material Science and Technology*, 2017.
- [12] A. L. Greer, “Grain refinement of alloys by inoculation of melts,” *Phil. Trans. R. Soc. Lond. A*, vol. 361, pp. 479–495, 2003.
- [13] T. E. Quested and A. L. Greer, “Athermal heterogeneous nucleation of solidification,” *Acta Mater.*, vol. 53, no. 9, pp. 2683–2692, 2005.
- [14] W. Kurz and D. Fisher, *Fundamentals of Solidification*, 4th ed. Trans Tech Publications, 1989.
- [15] M. E. Glicksman, *Principles of Solidification*. New York: Springer, 2011.
- [16] D. M. Stefanescu, *Science and Engineering of Casting Solidification*, 2nd ed. New York, 2009.
- [17] L. Backerud, “How a Good Grain Refiner Works,” *Light Met. Age*, vol. 41, no. 9,10, pp. 6–12, 1983.
- [18] M. Hillert, “On the theory of normal and abnormal grain growth,” *Acta Metall.*, vol. 13, no. 3, pp. 227–238, 1965.

References

- [19] J. S. Choi and D. Y. Yoon, “The temperature dependence of abnormal grain growth and grain boundary faceting in 316L stainless steel,” *ISIJ Int.*, vol. 41, no. 5, pp. 478–483, 2001.
- [20] J. Cormier, O. Yousfi, P. Villechaise, Y. Dahan, and B. Flageolet, “Characterization of Microstructures Containing Abnormal Grain Growth Zones in Alloy 718,” in *7th International Symposium on Superalloy 718 and Derivatives*, 2010, pp. 595–606.
- [21] D. A. Porter, K. E. Easterling, and M. Y. Sherif, “Diffusional Transformation in Solids,” in *Phase Transformations in Metals and Alloys*, C. Press, Ed. New York, 2009, pp. 261–374.
- [22] D. K. Xu, N. Birbilis, D. Lashansky, P. A. Rometsch, and B. C. Muddle, “Effect of solution treatment on the corrosion behaviour of aluminium alloy AA7150: Optimisation for corrosion resistance,” *Corros. Sci.*, vol. 53, pp. 217–225, 2011.
- [23] J. D. Embury and R. B. Nicholson, “The nucleation of precipitates: The system Al-Zn-Mg,” *Acta Metall.*, vol. 13, no. 4, pp. 403–417, 1965.
- [24] T. Marlaud, A. Deschamps, F. Bley, W. Lefebvre, and B. Baroux, “Influence of alloy composition and heat treatment on precipitate composition in Al-Zn-Mg-Cu alloys,” *Acta Mater.*, vol. 58, no. 1, pp. 248–260, 2010.
- [25] A. Deschamps, Y. Bréchet, and F. Livet, “Influence of Copper Addition on Precipitation Kinetics and Hardening in Al-Zn-Mg Alloy,” *Mater. Sci. Technol.*, vol. 15, no. 9, pp. 993–1000, 1999.
- [26] A. Guinier, “Structure of Age-Hardened Aluminium-Copper Alloys,” *Nature*, vol. 142, no. 3595, pp. 569–570, 1938.

References

- [27] G. D. Preston, “The Diffraction of X-Rays by Age-Hardened Aluminum Alloys,” *Proc. Roy. Soc.*, vol. A167, pp. 526–543, 1938.
- [28] G. A. Chadwick, *Metallography of Phase Transformations*. London: Butterworths, 1972.
- [29] J. W. Martin, *Precipitation Hardening*. Pergamon Press, 1968.
- [30] L. K. Berg, D. Schryvers, and L. R. Wallenberg, “GP-Zones In Al – Zn – Mg Alloys and Their Role in Artificial Ageing,” *Acta Mater.*, vol. 4, pp. 3443–3451, 2001.
- [31] Z. Katz and N. Ryum, “Precipitation kinetics in Al-alloys,” *Scr. Metall.*, vol. 15, no. 3, pp. 265–268, 1981.
- [32] K. Stiller, P. J. Warren, V. Hansen, J. Angenete, and J. Gjønnes, “Investigation of precipitation in an Al–Zn–Mg alloy after two-step ageing treatment at 100° and 150°C,” *Mater. Sci. Eng. A270*, vol. 270, pp. 55–63, 1999.
- [33] M. Nishi *et al.*, “Effect of the Zn/Mg Ratio on Microstructure and Mechanical Properties in Al-Zn-Mg Alloys,” *Mater. Sci. Forum*, vol. 794–796, pp. 479–482, 2014.
- [34] R. G. Buchheit, R. K. Boger, M. C. Carroll, R. M. Leard, C. Paglia, and J. L. Searles, “The electrochemistry of intermetallic particles and localized corrosion in Al alloys,” *J. Miner. Met. Mater. Soc.*, vol. 53, no. 7, pp. 29–33, 2001.
- [35] N. Birbilis *et al.*, “A closer look at constituent induced localised corrosion in Al-Cu-Mg alloys,” *Corros. Sci.*, vol. 113, pp. 160–171, 2016.
- [36] S. Wang, I. Huang, L. Yang, J. Jiang, and J. Chen, “Effect of Cu Content and Ageing Conditions on Pitting Corrosion Damage of 7xxx Series Aluminum Alloys,” *J.*

References

- Electrochem. Soc.*, vol. 162, no. 4, pp. 150–160, 2015.
- [37] P. A. Rometsch, Y. Zhang, and S. Knight, “Heat treatment of 7xxx series aluminium alloys - Some recent developments,” *Trans. Nonferrous Met. Soc. China (English Ed.)*, vol. 24, no. 7, pp. 2003–2017, 2014.
- [38] A. Boag, A. E. Hughes, A. M. Glenn, T. H. Muster, and D. McCulloch, “Corrosion of AA2024-T3 Part I: Localised corrosion of isolated IM particles,” *Corros. Sci.*, vol. 53, no. 1, pp. 17–26, 2011.
- [39] A. E. Hughes *et al.*, “Corrosion of AA2024-T3 Part II: Co-operative corrosion,” *Corros. Sci.*, vol. 53, no. 1, pp. 27–39, 2011.
- [40] A. M. Glenn *et al.*, “Corrosion of AA2024-T3 Part III: Propagation,” *Corros. Sci.*, vol. 53, no. 1, pp. 40–50, 2011.
- [41] R. G. Buchheit, “Local Dissolution Phenomena Associated with S Phase (Al₂CuMg) Particles in Aluminum Alloy 2024-T3,” *J. Electrochem. Soc.*, vol. 144, no. 8, p. 2621, 1997.
- [42] M. B. Vukmirovic, N. Dimitrov, and K. Sieradzki, “Dealloying and Corrosion of Al Alloy 2024-T3,” *J. Electrochem. Soc.*, vol. 149, no. 9, p. B428, 2002.
- [43] T. Hashimoto, X. Zhang, X. Zhou, P. Skeldon, S. J. Haigh, and G. E. Thompson, “Investigation of dealloying of S phase (Al₂ CuMg) in AA 2024-T3 aluminium alloy using high resolution 2D and 3D electron imaging,” vol. 103, pp. 157–164, 2016.
- [44] R. G. Buchheit, M. A. Martinez, and L. P. Montes, “Evidence for Cu Ion Formation by Dissolution and Dealloying the Al₂CuMg Intermetallic Compound in Rotating

References

- Ring-Disk Collection Experiments,” *J. Electrochem. Soc.*, vol. 147, no. 1, pp. 119–124, 2000.
- [45] O. Seri and M. Imaizumi, “The dissolution of FeAl₃ intermetallic compound and deposition on aluminum in AlCl₃ solution,” *Corros. Sci.*, vol. 30, no. 11, pp. 1121–1133, 1990.
- [46] O. Seri and K. Tagashira, “The Interpretation of the Interpretation of Polarization Curves for Al-Fe Alloys in De-Aerated NaCl Solution,” *Corros. Sci.*, vol. 30, no. 1, pp. 87–94, 1990.
- [47] S. K. Kairy, P. A. Rometsch, C. H. J. Davies, and N. Birbilis, “On the Intergranular Corrosion and Hardness Evolution of 6xxx Series Al Alloys as a Function of Si:Mg Ratio, Cu Content, and Ageing Condition,” *Corrosion*, vol. 73, no. 10, pp. 1280–1295, 2017.
- [48] L. L. Wei, Q. L. Pan, L. Feng, Y. L. Wang, and H. F. Huang, “Effect of ageing on corrosion property, electrochemical behavior and microstructure of Al-Zn-Mg-Cu alloy,” *Mater. Corros.*, vol. 66, no. 1, pp. 54–60, 2015.
- [49] X. Zhou *et al.*, “Grain-stored energy and the propagation of intergranular corrosion in AA2xxx aluminium alloys,” *Surf. Interface Anal.*, vol. 45, no. 10, pp. 1543–1547, 2013.
- [50] D. A. Jones, *Principle and Prevention of Corrosion*, Second Edi. Upper Saddle River: Prentice-Hall, 1996.
- [51] E. Ghali, *Corrosion Resistance of Aluminum and Magnesium Alloys*. Hoboken: John Wiley & Sons, 2010.

References

- [52] N. J. H. Holroyd and G. M. Scamans, “Stress corrosion cracking in Al-Zn-Mg-Cu aluminum alloys in saline environments,” *Metall. Mater. Trans. A Phys. Metall. Mater. Sci.*, vol. 44, no. 3, pp. 1230–1253, 2013.
- [53] T. Marlaud, B. Malki, C. Henon, A. Deschamps, and B. Baroux, “Relationship between alloy composition, microstructure and exfoliation corrosion in Al-Zn-Mg-Cu alloys,” *Corrosion. Sci.*, vol. 53, no. 10, pp. 3139–3149, 2011.
- [54] E. Charitidou, G. Papapolymerou, G. N. Haidemenopoulos, N. Hasiotis, and V. Bontozoglou, “Characterization of trapped hydrogen in exfoliation corroded aluminum alloy 2024,” *Scr. Mater.*, vol. 41, no. 12, pp. 1327–1332, 1999.
- [55] P. V. Petroyiannis, E. Kamoutsi, A. T. Kermanidis, S. G. Pantelakis, V. Bontozoglou, and G. N. Haidemenopoulos, “Evidence on the corrosion-induced hydrogen embrittlement of the 2024 aluminium alloy,” *Fatigue Fract. Eng. Mater. Struct.*, vol. 28, no. 6, pp. 565–574, 2005.
- [56] H. Kamoutsi, G. N. Haidemenopoulos, V. Bontozoglou, and S. Pantelakis, “Corrosion-induced hydrogen embrittlement in aluminum alloy 2024,” *Corros. Sci.*, vol. 48, no. 5, pp. 1209–1224, 2006.
- [57] J. F. Li, Z. Q. Zheng, S. C. Li, W. J. Chen, W. D. Ren, and X. S. Zhao, “Simulation study on function mechanism of some precipitates in localized corrosion of Al alloys,” *Corros. Sci.*, vol. 49, no. 6, pp. 2436–2449, 2007.
- [58] S. D. Liu, W. B. Liao, J. G. Tang, X. M. Zhang, and X. Y. Liu, “Influence of exfoliation corrosion on tensile properties of a high strength Al-Zn-Mg-Cu alloy,” *J. Cent. South Univ.*, vol. 20, no. 1, pp. 1–6, 2013.

References

- [59] D. McNaughtan, M. Worsfold, and M. J. Robinson, “Corrosion product force measurements in the study of exfoliation and stress corrosion cracking in high strength aluminium alloys,” *Corros. Sci.*, vol. 45, no. 10, pp. 2377–2389, 2003.
- [60] Z. Zhao and G. S. Frankel, “On the first breakdown in AA7075-T6,” *Corros. Sci.*, vol. 49, no. 7, pp. 3064–3088, 2007.
- [61] S. Wang, G. S. Frankel, J. Jiang, J. Chen, S.-L. Dai, and L. Zhen, “Mechanism of Localized Breakdown of 7000 Series Aluminum Alloys,” *J. Electrochem. Soc.*, vol. 160, no. 10, pp. C493–C502, 2013.
- [62] L. Mullert and J. R. Galvele, “Pitting Potential of High Purity Binary Aluminum Alloys - I. Al-Cu Alloys. Pitting and Intergranular Corrosion,” vol. 17, no. March 1976, 1977.
- [63] P. K. Rout, M. M. Ghosh, and K. S. Ghosh, “Microstructural, mechanical and electrochemical behaviour of a 7017 Al-Zn-Mg alloy of different tempers,” *Mater. Charact.*, vol. 104, pp. 49–60, 2015.
- [64] R. . Roy, *Design of Experiments Using The Taguchi Approach: 16 Steps to Product and Process Improvement*, 1st ed. Wiley-Interscience, 2001.
- [65] S. Shankar, “Professor, McMaster University, Personal Communication.” .
- [66] American Society for Testing and Materials, “ASTM E18-17e1 Standard Test Methods for Rockwell Hardness of Metallic Materials,” pp. 1–38, 2017.
- [67] American Society for Testing and Materials, “Standard Test Method for Exfoliation Corrosion Susceptibility in 2xxx and 7xxx Aluminium Alloys,” *Astm*, vol. 3, no. Reapproved 2013, p. 99, 1974.

References

- [68] S. Lee, B. W. Lifka, and A. C. G. on C. of Metals, “Modification of the EXCO test method for exfoliation corrosion susceptibility in 7XXX, 2XXX, and aluminum-lithium alloys,” *New Methods Corros. Test. Alum. Alloy.*, pp. 1–19, 1991.
- [69] D. Gildemeister, “Effects of Microstructure on Hot Cracking Behavior in Al–Zn–Mg–Cu Alloys,” in *Light Metals 2018*, 2018, pp. 1097–1104.
- [70] M. E. Glicksman, “Grain Refinement,” in *Principles of Solidification: An Introduction to Modern Casting and Crystal Growth Concepts*, Gainesville: Springer, 2010, pp. 290–301.
- [71] Z. Zhao and G. S. Frankel, “The effect of temper on the first breakdown in AA7075,” *Corros. Sci.*, vol. 49, no. 7, pp. 3089–3111, 2007.
- [72] S. Chen, K. Chen, G. Peng, L. Jia, and P. Dong, “Effect of heat treatment on strength, exfoliation corrosion and electrochemical behavior of 7085 aluminum alloy,” *Mater. Des.*, vol. 35, pp. 93–98, 2012.
- [73] Q. Meng and G. S. Frankel, “Effect of Cu Content on Corrosion Behavior of 7xxx Series Aluminum Alloys,” *J. Electrochem. Soc.*, vol. 151, no. 5, pp. B271–B283, 2004.
- [74] C. M. Liao and J. M. Olive, “In-situ monitoring of pitting corrosion in aluminum alloy 2024,” *Corrosion*, vol. 54, no. 6, pp. 451–458, 1998.
- [75] G. S. Chen and M. Gao, “Microconstituent-induced pitting corrosion in aluminum alloy 2024-T3,” *Corrosion*, vol. 52, no. 1, pp. 8–15, 1996.